UNIVERSITY OF CALIFORNIA
SANTA CRUZ

MELTING GLACIAL ICE FROM BELOW: FROM VOLCANOES TO ICE SHELVES

A dissertation submitted in partial satisfaction
of the requirements for the degree of

DOCTOR OF PHILOSOPHY

in

EARTH SCIENCES

by

Carolyn Branecky Begeman

June 2018

The Dissertation of Carolyn Branecky Begeman is approved:

_____
Professor Slawek Tulaczyk, chair

_____
Professor Andrew T. Fisher

_____
Professor Tim Stanton

_____
Professor Michael Manga

_____
Tyrus Miller
Vice Provost and Dean of Graduate Studies

Table of Contents

List of Figures

List of Tables

Chapter 3

Chapter 4

Abstract

Melting glacial ice from below: from volcanoes to ice shelves

Carolyn Branecky Begeman

Antarctica is a major source of potential sea level rise, holding 58 meters of sea level equivalent in the Antarctic Ice Sheet. The Antarctic Ice Sheet's mass balance is governed indirectly by melting from below, which determines the rate at which ice flows from the interior of the continent to the ocean. My thesis addresses three sources of heat which contribute to basal melting: oceanic heat flux, geothermal heat flux, and heat from subglacial volcanism. I measured oceanic heat flux and geothermal heat flux at a location in West Antarctica where the ice sheet transitions from grounded on the continent to floating over the ocean. Oceanic heat flux and thus ice-shelf basal melt rates were low at this site (0.7 W m^{-2} or 7 cm yr^{-1}) as a result of slow currents and stable stratification of colder and fresher water near the ice base. On the other hand, geothermal heat flux was moderately high at this site (0.09 W m^{-2}), though lower than the oceanic heat flux. Another measurement of geothermal heat flux only 100 km away revealed a much higher value (0.3 W m^{-2}); this spatial variability in geothermal heat flux could be explained by magmatic intrusions and/or advection of heat by flowing crustal fluids. In a separate investigation, I assess whether the magmatic history in Antarctica and elsewhere might have been influenced by the glacial history of these regions. Using a thermomechanical magma reservoir model, I show that ice thinning can increase the frequency of eruptions from ice-covered volcanoes and thus increase basal melting. The results from these three

projects can improve the representation of basal melting sources in ice-sheet models and thus improve the accuracy of sea level projections.

Dedication

To all women involved in the production and dissemination of knowledge, from indigenous healers to Florence Bascom to my peers in the University of California, Santa Cruz, Earth and Planetary Sciences department.

Acknowledgements

First and copious thanks go to my advisor on this dissertation, Slawek Tulaczyk, for making this work possible and for supporting me on every professional front. Slawek always showed confidence in my abilities and that helped bolster my own confidence. John B. Anderson deserves credit for introducing me to the field of glaciology, providing me research experience in glacial sedimentology, and encouraging me to work with Slawek Tulaczyk. Alexandra Witus, my undergraduate thesis supervisor, showed me how to be an effective graduate student researcher before I knew whether that was what I wanted to be. Leigh Stearns's mentorship and the NSF Research Experiences for Undergraduates program solidified my desire to undertake a graduate degree in Earth Sciences.

I have been fortunate to receive generous financial support from the National Science Foundation Graduate Research Fellowship, the University of California Chancellor's Fellowship, the University of California President's Graduate Fellowship, and the Philanthropic Educational Organization Scholar Award.

The work in Chapters 2 and 4 was supported by the US National Science Foundation, Section for Antarctic Sciences, Antarctic Integrated System Science program as part of the interdisciplinary WISSARD (Whillans Ice Stream Subglacial Access Research Drilling) project. The drilling team from University of Nebraska–Lincoln, the WISSARD traverse personnel, the U.S. Antarctic Program, and Air National Guard and Kenn Borek Air provided technical and logistical support.

The geothermal heat flux measurement presented in Chapter 2 would not have been possible without the efforts of Slawek Tulaczyk and Andrew Fisher to design a geothermal probe for ice borehole deployment. D. Thayer, D. Smith, and S. Ornellas were the primary builders of the geothermal probe. T. Sproule collaborated on geothermal probe thermistor calibration. D. van den Dries assisted in the analysis of sediment core WGZ-GC-1. This work was supported by awards from the U.S. National Science Foundation as part of the WISSARD project, NSF grants ANT-1346251, ANT-0838947, ANT-0839142, OCE-0939564, and OCE-1260408. This is C-DEBI contribution 391.

I acknowledge my co-authors on Chapter 3: Michael Manga, Tobias Keller, and Wim Degruyter. This study would not have been conceived without the support of the Cooperative Institute for Deep Earth Research (CIDER) which brought early, mid and late career scientists together for a summer workshop and provided financial support for the continuation of this work through NSF Award EAR-1135452. Special thanks go to the participants in the CIDER working group: Federica Lanza, Michael Farner, Tobias Keller, Gaia Siravo, Helge Gonnermann, Peter Huybers, Michael Manga, and Wouter van der Wal.

My co-authors on Chapter 4 have provided invaluable data and feedback on the project: Slawek M. Tulaczyk, Oliver J. Marsh, Jill A. Mikucki, Timothy P. Stanton, Timothy O. Hodson, Matthew R. Siegfried, Ross D. Powell, Knut Christianson, and Matt A. King. Timour Radko also provided helpful comments on the analysis of the observed double-diffusive staircase. Additional funding for

instrumentation development was provided by grants from the Gordon and Betty Moore Foundation, the National Aeronautics and Space Administration (Astrobiology and Cryospheric Sciences programs) and the US National Oceanic and Atmospheric Administration. We acknowledge Keith Nicholls and Hugh Corr of the British Antarctic Survey for design and loan of the ApRES instrument. M.A.K. is a recipient of an Australian Research Council Future Fellowship (project number FT110100207) and his research was supported under Australian Research Council's Special Research Initiative for Antarctic Gateway Partnership (Project ID SR140300001). M.R.S. was supported by NSF-ANT-0838885 and the George Thompson Postdoctoral Fellowship and Stanford University. This research is based on data services provided by the UNAVCO Facility with support from the National Science Foundation (NSF) and National Aeronautics and Space Administration (NASA) under NSF Cooperative Agreement No. EAR-0735156.

Chapter 2 of this dissertation is a reprint of the following previously published material: Begeman, C. B., Tulaczyk, S. M., & Fisher, A. T. (2017). Spatially Variable Geothermal Heat Flux in West Antarctica: Evidence and Implications. *Geophysical Research Letters*, *44*. https://doi.org/10.1002/2017GL075579. The dissertation author was the primary investigator and author of this material.

Chapter 3 of this dissertation is currently being prepared for submission for publication. The dissertation author was the primary investigator and author of this material.

Chapter 4 of this dissertation has been submitted to Journal of Geophysical Research, Oceans: Begeman, C. B., Tulaczyk, S. T., Marsh, O. J., et al. (submitted 2018). Ocean stratification and low melt rates at the Ross Ice Shelf grounding zone. *Journal of Geophysical Research, Oceans.* The dissertation author was the primary investigator and author of this material.

Chapter 1 Introduction

1.1 Motivation

Sea level rise is a major societal concern, as a tenth of the world's population live within 10 m of present-day sea level. Sea level rose at a rate of 3.2 mm yr^{-1} during 1993-2010 (Nerem et al., 2010); about a third of this rise is due to thermal expansion of seawater (IPCC AR5 WG1, p.295) and the rest to contributions from land ice. While the long-term contribution of thermal expansion to sea level rise is limited (<0.5 m by 2100) (Mengel et al., 2016), there is a large supply of land ice, enough to raise sea level by ~65 m (J. L. Chen et al., 2006; Fretwell et al., 2013; Marzeion et al., 2012). Thus the net gain or loss of land ice, its mass balance, is important for sea level projections.

Antarctica is the largest repository of ice on Earth, holding 58 m of sea level rise within its ice sheet. The Antarctic Ice Sheet's mass balance is primarily controlled by the precipitation of snow (accumulation) and the movement of ice across the grounding line, the transition between grounded and floating ice (Eric Rignot et al., 2008) (Figure 1.1). While ice melting is a relatively minor direct source of ice loss in Antarctica, it can increase ice loss indirectly by accelerating the flow of ice across the grounding line. On land, melting of the ice sheet at its base accelerates ice flow by reducing friction between the ice base and the underlying bedrock or sediments (Budd et al., 1984). Basal melting of floating ice shelves also accelerates ice flow by reducing the resistance to ice flow offered by the ice shelf, known as buttressing (Gagliardini et al., 2010).

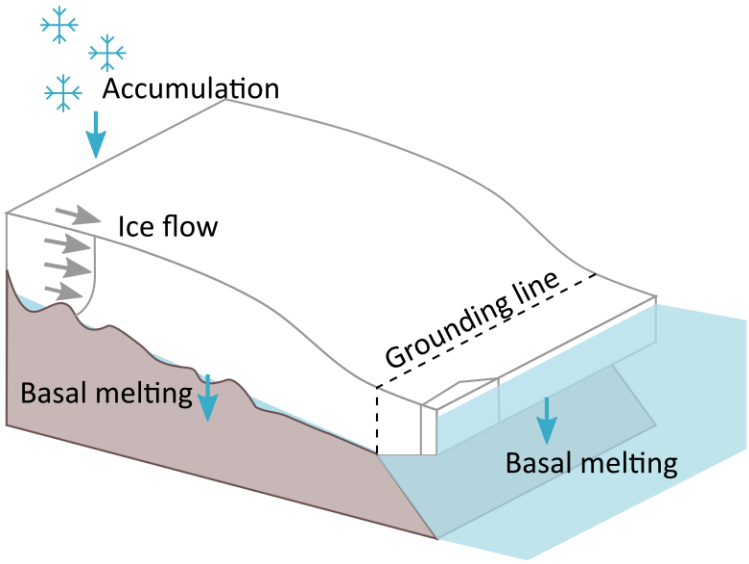

Figure 1.1. Key mass balance terms of the Antarctic Ice Sheet. Accumulation is the key source term and flow across the grounding line is the key loss term in Antarctic Ice Sheet mas balance. Basal melting on land and of floating ice mostly affect mass balance indirectly through its effect on ice velocity.

This thesis addresses several aspects of the basal melting of ice sheets. Geothermal heat flux is one of the least well-understood contributions to basal melting. In Section 1.1 we review the current understanding of sensitivity of ice dynamics to geothermal heat flux and ongoing challenges in determining this flux. We present a new measurement of geothermal heat flux below the West Antarctic Ice Sheet and explore the regional variability in geothermal heat flux (Chapter 2). Sub-ice volcanism can enhance basal melting, through geothermal heat flux or by direct contact between erupted material and ice. In Section 1.2 we discuss current literature that postulates that deglaciation enhances volcanism. We then present our own assessment of a possible mechanism by which deglaciation triggers eruptions (Chapter 3). In Section 1.3, we review aspects of sub-ice-shelf oceanography relevant

to ice-shelf melting. This sets the stage for Chapter 4, in which we relate basal melting near the grounding zone of an ice shelf to local oceanographic conditions. We end each introductory section with a list of key questions and briefly explain how each chapter will address them.

1.2 Geothermal heat flux below ice sheets

At present, we have little knowledge of the role geothermal heat flux (GHF) plays in present-day ice dynamics, as the GHF field below ice sheets is largely unknown. We have a theoretical understanding of several mechanisms by which GHF could influence ice dynamics that have been tested with ice-sheet modeling studies. GHF may enhance ice flow within ice streams by increasing basal melt rates; this subglacial meltwater then reduces friction between ice and the basal substrate (Budd et al., 1984). Modeled ice stream flow is enhanced by GHF, given a modeled basal friction coefficient that is sensitive to the amount of basal water (Näslund et al., 2005; Seroussi et al., 2017)(Näslund et al., 2005; Seroussi et al., 2017)(Näslund et al., 2005; Seroussi et al., 2017). Subglacial water availability may also affect ice flow by increasing the porewater pressure of subglacial sediments, making them more easily deformable (Bougamont, 2003). Warming of basal ice by GHF can enhance ice deformation because the viscosity of ice is inversely related to temperature (Weertman, 1983). Thus, high GHF can enhance modeled ice flow even in the absence of basal melting (Pittard et al., 2016).

The surface velocity field results from the force balance of the ice sheet and its flow properties. Thus, this field contains information about how GHF is affecting

ice viscosity, basal friction, and subglacial sediment deformation. Currently ice-sheet models use the surface velocity signal to infer a basal friction field given a flow law for ice and a GHF field. Thus, errors in the GHF field may be converted into errors in the basal friction field. Accurate predictions of ice-sheet mass balance may depend on deconvolving GHF, which evolves on long timescales, from basal friction, which may evolve on much shorter timescales (e.g., Beem et al., 2014). Thus, improvements to the GHF field may simultaneously improve inversions for basal friction. The GHF field may also offer insight into the geology and tectonic history of the accreted terrains of West Antarctica and its rift system and the East Antarctic craton, which itself comprises distinct tectonic provinces .

The only way to directly measure GHF to the ice-sheet base is to measure the thermal gradient in the subsurface and thermal conductivity of the substrate. GHF measurements in Antarctica are sparse compared with other continents. Direct measurements of GHF in West Antarctica are limited to exposed land or continental shelves, a sub-ice-shelf measurement, and one measurement below an active ice stream (Fisher et al., 2015)(Fisher et al., 2015). Climatic perturbations to the surface temperature gradient have also limited the usefulness of GHF measurements. Geothermal gradients on the continental shelf have been impacted by fluctuations in the oceanic bottom water temperature (Dziadek et al., 2017).

GHF measurements are not commonly collected through ice boreholes. Access to the ice bed is often avoided to prevent contamination from drilling operations in the absence of clean access methods. Instead, many studies have

attempted to infer GHF from basal ice temperature gradients. One of the main difficulties with this inference has been a poorly-constrained vertical ice velocity, which decays to zero at the ice base (Clow et al., 2012; Engelhardt, 2004). The uncertainties of these measurements are on the order of 10s of mW m^{-2}, but could be higher where subglacial melting, freezing, or water flow occur.

The distribution of subglacial water may be a glaciological indicator of the GHF field. Actively draining or filling subglacial lakes, which can be identified from surface elevation changes, have been used to set a lower bound on GHF for lake preservation at those sites (Siegert & Dowdeswell, 1996). A more recent study used a radar-derived distribution of subglacial water, a water routing algorithm, and an estimate of catchment-wide basal melt rates to derive a catchment-wide GHF field (Schroeder et al., 2014). The application of this approach is limited by appropriate geological conditions for detecting basal water, the sensitivity of water-routing algorithms to errors in bed topography, and poorly-constrained basal melt rates. Additionally, these approaches neglect the role that groundwater may play in determining the distribution of subglacial water.

The most common approach to GHF mapping over large regions has been to use geophysical methods to constrain thermal conditions at depth. These constraints include seismic topography estimates of upper mantle temperature (An et al., 2015) and satellite magnetic field estimates of the depth of the 540 °C isotherm (Fox Maule et al., 2005; Martos et al., 2017). However, to convert these constraints into a GHF field, the crustal contributions to GHF are required. The distribution of radiogenic

heat production in the crust is a major source of uncertainty. Some constraints on radiogenic heat production are offered by sampled rocks (Burton-Johnson et al., 2017; Carson et al., 2014; Goodge, 2018), but it is often unclear over what spatial scales and depths these measured production rates are representative, given our limited knowledge of subglacial geology. Additional uncertainties are associated with the thermal conductivity of materials at depth, and the potential role of crustal fluids in redistributing heat.

In 2015, a borehole was drilled through the West Antarctic Ice Sheet, to the base of the Whillans Ice Stream at the grounding zone. This offered an opportunity to directly measure GHF. Our team was motivated to collect a measurement in this ice stream because a previous direct measurement of GHF upstream suggested locally high GHF . This grounding zone measurement allowed us to determine how spatially-confined this high GHF was. We collected measurements of the geothermal gradient using a probe designed at built at University of California, Santa Cruz, and sediment cores were used to measure the thermal conductivity of subglacial sediments.

Key questions

What is the distribution of GHF in West Antarctica?

We constrained the GHF field in West Antarctica through a new direct measurement. This measurement was collected through an ice borehole near the Transantarctic Mountains where elevated mantle temperatures and mantle melt are inferred.

What spatial variability in GHF is present in West Antarctica?

By measuring GHF 100 km from a previous GHF measurement, we provided a lower bound on the spatial variability of GHF. These two measurements are the most closely spaced measurements below the West Antarctic Ice Sheet to date. In Chapter 2, I discuss sources of spatial variability in the GHF field in West Antarctica and provide some estimates of the magnitude and potential causes of this variability.

Is spatial variability in GHF relevant to the dynamics of the West Antarctic Ice Sheet?

We provide a comparison between GHF and other heat sources in the sector of West Antarctica where these measurements are collected. This comparison yields insight into the GHF contribution to subglacial melting within ice streams, the conduits of ice loss for the West Antarctic Ice Sheet. We also calculate steady-state ice temperature profiles in slow-flowing regions of the ice sheet to determine whether spatial variability in GHF might affect the longevity of these features, which stabilize the current grounding line and ice shelf in this sector of the ice sheet.

1.3 A possible link between deglaciation and volcanism

Glaciovolcanism denotes the interactions between magma and ice, in all its forms . The potential for glaciovolcanism is widespread, as ice-covered volcanoes are present in both polar regions and tropical regions and on every continent except Australia. Glaciovolcanism has attracted interest because of the unique volcanic hazards and eruptive styles associated with volcano-ice interactions and because of potential feedbacks between volcanism and climate.

It is relatively uncontroversial that volcanism can also affect local ice loss, through enhanced GHF (Jarosch & Gudmundsson, 2007), contact between erupted debris and ice (M. T. Gudmundsson et al., 1997), and the albedo-reducing effect of ash cover on ice (Conway et al., 2010)(Conway et al., 2010). During at least some periods in geologic history, it is clear that volcanism affected global climate through volcanic greenhouse gas emissions. The hypothesis that ice loss can affect volcanism is more controversial. However, there are multiple lines of evidence from both global and local eruption records that point to an increase in volcanism during deglaciations (reviewed by Tuffen, 2010; Watt et al., 2013). Given that ice loss from mountain glaciers has accelerated in the last several decades, will be another period of enhanced volcanism (Tuffen, 2010)? Since deglaciation-induced volcanism may lead to more rapid ice retreat and sea level rise, this is an important question for the glaciology community.

There is currently no consensus on the mechanisms responsible for deglaciation-induced volcanism. We consider several mechanisms in terms of how they affect magmatic fluxes through the crust (Figure 1.2).

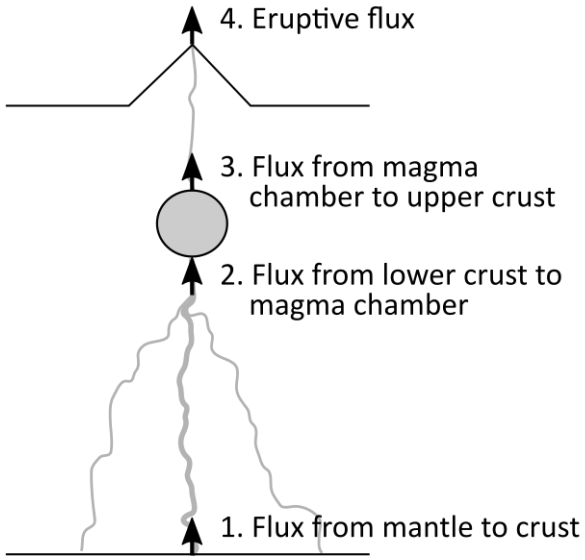

Figure 1.2. Mechanisms for increasing eruptive flux during deglaciation organized by fluxgates through the crust.

Flux from the mantle to the crust may increase if pressure perturbations from ice load changes reach the mantle and trigger decompression-melting. An increased mantle melting signature has been detected in the geochemistry of erupted deposits in Iceland (Hardarson & Fitton, 1991). Modeling suggests that ice unloading in Iceland could have increased the volume rate of mantle melting 20- to 30-fold (Jull & McKenzie, 1996; Sigvaldason et al., 1992). This mantle melting response to surface unloading may be uniquely important in Iceland due to its tectonic setting at a spreading center. Eruptive flux at other volcanoes changes over timescales that are likely too short for mantle melting, favoring a crustal stress mechanism for the deglacial response (Rawson et al., 2016).

Glacial isostatic adjustment might enhance melt migration through the lithosphere by generating deviatoric tensile stress in the lower crust during glaciation and in the upper crust during deglaciation (Nakada & Yokose, 1992; Stevens et al., 2016). Dyke orientations in Iceland suggest that the stress field from ice unloading impacts the dynamics of dyke propagation (Hooper et al., 2011). Furthermore, fractures opened in the anisotropic stress field that could be generated by deglaciation may be larger than those generated in an isotropic stress field . Thus, the volume of erupted material may be larger during deglaciation.

Changes to the crustal stress field can also change the conditions for dyke initiation (Albino et al., 2010; Bakker et al., 2016; Sigmundsson et al., 2010). Generally, the confining pressure in the crust decreases during deglaciation. This increases the deviatoric tensile stress created by magma pressure in the surrounding crust and promotes dyke initiation. Previous studies have suggested that this effect could trigger eruptions for magmatic systems already close to eruption conditions (Albino et al., 2010) or produce a lagged response, depending on the timescale of ice unloading relative to the viscous relaxation timescale (Jellinek et al., 2004).

Most of the proposed mechanisms are related to the direct perturbation in the crust or mantle caused by an ice load. However, it has also been noted that ice can indirectly change the stress distribution in the crust, through thermal perturbations that weaken the strength of rock and induce slope failures (Huggel et al., 2008), hydrologic changes that promote fault motion or slope failure (Capra, 2006), or enhanced surface load changes through glacial erosion (Sternai et al., 2016).

Likely no single mechanism explains the full change in eruption frequency from glaciations to deglaciations. In Chapter 4 we consider one of these mechanisms, changing the conditions for dyke initiation, which is broadly applicable to glaciated volcanoes. Our goal is to determine the sensitivity of eruption frequency to glacial loading and unloading via this mechanism. While the glacial changes in crustal stress have been examined in previous studies, the change in magma pressurization rates due to surface loading and unloading has not been included in these models with phase changes. To explore this sensitivity, I adapted a thermomechanical magma reservoir model (Degruyter & Huber, 2014) to account for both crustal pressure and magma pressure changes.

Key questions

How much do eruption frequencies change during glacial cycles as a result of direct crustal stress changes from ice loss?

We simulate magma reservoir dynamics and eruption timing using a thermomechanical magma reservoir model under slow to moderate loading and unloading rates corresponding to glacier growth and retreat. We quantify the change in dyke initiation frequency for these glaciated cases from cases with no load changes. These results allow us to address the following related questions:

a. Is a change in the frequency of dyke initiation sufficient to explain a change in eruption frequency between glaciation and deglaciation, assuming the likelihood of dyke propagation to the surface remains constant?

b. Is this change sufficient to produce an increase in eruption frequency at present rates of ice retreat?

What are the first-order controls on eruption sensitivity to glacial load changes?

We determine the key controls on eruption sensitivity to glacial load changes within the modeling framework by varying parameters that control magma reservoir evolution: the timescales for magma recharge, viscous relaxation, and reservoir cooling. We also vary load rate and determine how eruption frequency depends on the lithospheric pressure change at the magma reservoir.

Do magma reservoir dynamics play a significant role in the eruptive response to load changes?

We compare the standard simulations with simulations that only include the effects of unloading on magma reservoir processes and not the effects on the dyke initiation threshold to determine the relative importance of magma reservoir processes in the eruptive response to deglaciation. We parse this sensitivity by comparing the phase changes, viscous relaxation and other processes between loading, no loading and unloading cases. This study will guide future studies regarding what magma chamber dynamics may be relevant to the magmatic response to unloading.

1.4 Sub-ice-shelf oceanography and ice-shelf melting

Ice shelves surround 50-75% of the Antarctic coastline, and the majority of ice drains through these features (Rignot et al., 2011, 2013). Ice shelves slow the flow of ice from the interior of the ice sheet, evidenced by increased ice flow after the loss of ice-shelf area (Rignot et al., 2004). Ice sheet modeling studies indicate that ice

flow is also sensitive to changes in ice shelf thickness, losing up to the same volume of grounded ice as the volume of floating ice that was lost . Thus, ice-sheet mass balance is impacted by ice-shelf melting. Although we can measure present-day ice-shelf melting by satellite, we don't fully understand how ice-shelf melting relates to ocean conditions, which we cannot remotely sense. This relationship is believed to be key to improving sea-level rises projections from coupled ice-sheet and ocean models.

Ice shelves along the Antarctic coast are threatened by the incursion of warm water onto the continental shelf . To what degree these ice shelves will melt if ocean water warms is a subject of much concern. The oceanic heat that is available for melting, called thermal driving, is the difference between the sub-ice-shelf seawater temperature and the salinity- and pressure-dependent melting point at the ice-shelf base. Thus, ice-shelf melting at thermodynamic equilibrium is a function of the seawater temperature and salinity at the ice-shelf base and its depth. Continental shelf waters around Antarctica range from -2 to 4 °C (Schmidtko et al., 2014). Sub-ice-shelf seawater salinities are generally high as a result of sea ice formation, but can fluctuate with sea ice extent and volume (Jacobs & Giulivi, 2010) and land ice meltwater fluxes . The seafloor depth around the Antarctic coasts varies from 120 - 1200 m (Fretwell et al., 2013). The combined effect of a deep continental shelf and high salinities results in melting points of -1 to -2 °C (IOC et al., 2010).

The seawater temperature and salinity in the ice-shelf cavity is not well constrained due to the difficulty of accessing this environment. Limited sub-ice-shelf

oceanographic observations suggest a two-layer model. The lower layer is a mass of salty (and thus dense) continental shelf water. The upper layer, called Ice Shelf Water, is a mixture of lower layer water and cold, fresh water from ice-shelf basal melting, and in some places from subglacial ice melting. Ice Shelf Water, because of its buoyancy, rises along the ice-shelf base toward the open ocean.

Ocean models currently used to predict ice-shelf melting do not capture turbulence at small enough scales to accurately predict the oceanic heat and salt flux within a few meters of the ice-shelf base. Thus, parameterizations are used to predict ice-shelf melt rates from the seawater temperature, salinity and velocity at the nearest grid cells to the ice-shelf base. These parameterizations can reproduce mean ice-shelf melt rates and some of the observed spatial patterns of ice-shelf melting . However, there is reason to doubt that these parameterizations can accurately predict the response of ice shelves to changing ocean conditions.

Simultaneous observations of ice-shelf melting and oceanographic conditions (presented in Chapter 4 and Jenkins et al., 2010) are not consistent with currently-used parameterizations. Furthermore, the drag coefficient used to estimate shear stress at the ice-shelf base in these models is unknown and may be spatially and temporally variable. This may cause order-of-magnitude variability in basal melt rates. A more fundamental uncertainty is the relationship between buoyancy stratification, current velocity, and eddy diffusivities. These parameterizations assume that the heat flux to the ice base is linearly proportional to both thermal driving and the mean horizontal velocity near the ice base. This has not been established by rigorous studies of sub-

ice-shelf turbulence. This functional dependence is needed to determine how sensitive basal melting is to future changes in ocean conditions.

Under-ice turbulence is complicated by the freshwater flux from ice-shelf melting combined with a negative heat flux associated with the latent heat of melting The buoyancy flux due to seawater dilution may reduce the scale of turbulent mixing near the boundary, as it does in the atmospheric boundary layer, reducing the oceanic heat flux (McPhee, 1981). However, the unstable temperature gradient that is generated may induce small-scale ocean mixing, double-diffusive convection, that is not captured in ocean models (e.g., Turner, 1965; Radko, 2013). These dynamics are being explored though sub-ice-shelf turbulence observations and turbulence modeling .

The narrow sub-ice-shelf cavity near the grounding line is a particularly critical region to investigate ice-shelf melting because upstream ice loss is most sensitive to ice shelf thinning in this zone (Reese et al., 2018). We have the least information about water mass properties near the grounding line because it is far from the ice-shelf front, where oceanographic observations are most often collected. In this study, we collect oceanographic observations in a narrow sub-ice-shelf cavity a few km from the grounding zone of the Ross Ice Shelf, the largest ice shelf in Antarctica.

Key questions

What is the ice-shelf basal melt rate close to the grounding zone?

Satellite-derived measurements of ice shelf melting require the ice-shelf to be in isostatic equilibrium to translate surface elevation changes into ice-shelf melt rates.

Since the ice shelf is not in isostatic equilibrium within ~10 km of the grounding line, we do not generally have knowledge of the spatial distribution of ice-shelf melting in this zone. For our study, we collect ground-based radar measurements that provide high spatial resolution, high temporal resolution, and high accuracy in melt rates from 0 to 20 km from the grounding line.

Do ice-shelf melting parameterizations accurately describe ocean fluxes in different sub-ice-shelf settings?

At this grounding zone site we simultaneously measure ocean conditions and ice-shelf melting. We compare the measured ice-shelf melt rate with ice-shelf melting parameterizations using observed ocean conditions. The setting where we collect these measurements has colder seawater and lower flow conditions than the one previous setting where this comparison has been made (Jenkins et al., 2010). This provides an opportunity to constrain eddy diffusivities within these parameterizations.

What dynamics control mixing lengthscales close to the ice base?

Given the gaps in our understanding of sub-ice-shelf turbulence introduced previously, there is no ready framework through which to analyze the observed structure of stratification at our site. We consider several possible explanations for the characteristics of the stratification that we observe, in an attempt to understand the turbulent dynamics that influenced that stratification. We make the case that double-diffusive dynamics influence stratification and oceanic heat and salt fluxes at this site.

The contribution of tidal forcing to ice-shelf melting remains somewhat enigmatic. Modeling studies suggest that tidal mixing varies regionally and tidal

forcing may increase ice-shelf melt rates in some locations while decreasing melt rates in others (Mueller et al., 2018). Tidal variations in current velocity below ice-shelves are thought to lead to time-variable oceanic heat fluxes to the ice base. It has also been proposed that in narrow ocean cavities tidal forcing may destroy stratification. We analyze time series of current velocity at two different parts of the tidal cycle and a time series of ice-shelf elevation at the site. We evaluate the strength of tidal forcing at our site, which lies within a narrow ocean cavity, and determine the tidal dissipation needed to destroy stratification.

Chapter 2 Spatially variable geothermal heat flux in West Antarctica

Abstract

Geothermal heat flux (GHF) is an important part of the basal heat budget of continental ice sheets. The difficulty of measuring GHF below ice sheets has directly hindered progress in understanding of ice sheet dynamics. We present a new GHF measurement from below the West Antarctic Ice Sheet, made in subglacial sediment near the grounding zone of the Whillans Ice Stream. The measured GHF is 88 ± 7 mW m^{-2}, a relatively high value compared to other continental settings and to other GHF measurements along the eastern Ross Sea of 55 mW m^{-2} and 69 ± 21 mW m^{-2}, but within the range of regional values indicated by geophysical estimates. The new GHF measurement was made ~100 km from the only other direct GHF measurement below the ice sheet, which was considerably higher at 285 ± 80 mW m^{-2}, suggesting spatial variability that could be explained by shallow magmatic intrusions or the advection of heat by crustal fluids. Analytical calculations suggest that spatial variability in GHF exceeds spatial variability in the conductive heat flux through ice along the Siple Coast. Accurate GHF measurements and high-resolution GHF models may be necessary to reliably predict ice sheet evolution, including responses to ongoing and future climate change.

2.1 Introduction

Geothermal heat flux (GHF) is a significant source of heat in polar subglacial environments. It affects the temperature at the base of ice sheets, impacting the ice

sheet mass balance directly through basal melting or freezing. GHF can have a large indirect effect on ice sheet mass balance when it brings the basal temperature above the melting point because the presence of basal meltwater reduces basal resistance, facilitating fast sliding of ice [*Weertman*, 1964]. GHF is prescribed as part of the lower boundary conditions for ice sheet models, which calculate patterns of basal melting and freezing to determine the degree of ice sliding. Ice sheet models are sensitive to the magnitude and spatial variability of GHF, particularly when the GHF contribution shifts basal temperatures across the melting point [*Bougamont et al.*, 2015; *Pittard et al.*, 2016].

Despite the importance of GHF below ice sheets, there are relatively few direct measurements of this key parameter [*Davies and Davies*, 2010], mainly because it is so difficult to access the subglacial environment. Prior to this study, the only direct GHF measurement below the WAIS was made at Subglacial Lake Whillans (SLW) [*Fisher et al.*, 2015]; estimates were made at two additional locations using basal ice temperatures and assumptions about local ice dynamics [*Engelhardt*, 2004a; *Clow et al.*, 2012]. GHF has been inferred for some regions of the WAIS from the distribution of subglacial water [*Siegert and Dowdeswell*, 1996; *Schroeder et al.*, 2014]. Due to the paucity of observations, the GHF distribution used in ice sheet models typically falls within a relatively narrow range and has low spatial variability, based on geological or remotely-sensed properties of the underlying lithosphere [*Pollack et al.*, 1993; *Shapiro and Ritzwoller*, 2004; *Maule*, 2005; *An et al.*, 2015; *Burton-Johnson et al.*, 2017]. GHF models of West Antarctica are

inconsistent with one another in both magnitude and distribution (Figure S2.1), suggesting that GHF is not well constrained.

2.2 Materials and Methods

We determined the GHF 3 km downstream of the Whillans ice stream Grounding Zone (WGZ) using an ice borehole to collect measurements of thermal gradient and thermal conductivity.

2.2.1 Temperature gradient in sediments

The ice drilling operations are described in Tulaczyk *et al.* [2014]. The geothermal probe used to measure the thermal gradient is the same tool used at SLW [*Fisher et al.*, 2015]. For the present study, the geothermal probe was deployed twice, on 15 January 2015 and 18 January 2015, resulting in a horizontal distance of 3 m between measurements due to ice movement. The probe makes subsurface measurements with three autonomous sensor/logger systems, with sensor spacing of 62 cm. Autonomous sensors/loggers were calibrated before deployment with absolute accuracy of ±0.002°C [*Fisher et al.*, 2015]. The sensors/loggers were programmed just before deployment for synchronous data collection every 2s. After data were recovered, and calibration corrections were applied, we performed an additional shift to individual sensors (0.003 – 0.008°C) based on measurements made when the geothermal probe was held stationary in the water column (Figure S2.2). This is the routine approach for GHF measurements in the deep sea, and assures that small variations in apparent temperature (generally due to electronic drift) do not bias geothermal data.

After the probe was inserted into the sediment at WGZ, it was held still for ~10 minutes to record the transient temperature response. Data from this measurement period for each sensor were fitted to a conductive heat flow model of temperature equilibration [*Bullard*, 1954] using TP-Fit software [*Heesemann et al.*, 2006]. The modeled equilibration period started ~100 s after penetration, to avoid deviations from the idealized model used to fit the data (a thin line source), and lasted 5-8 minutes. Processing of the data was managed sensor by sensor, with care taken to avoid data intervals that included evidence for probe motion, expressed as frictional heating that lead to subtle deviations in the standard equilibration curve. Data processing was completed with thermal conductivity values that are consistent with measurements described in section 2.2. Equilibration of conventional oceanographic heat flow probes often takes longer than the usual 6-7 minute measurement window [*Davis and Fisher*, 2011], but the geothermal sensor/logger systems used in this study have sensors mounted within 5-mm outer diameter stainless steel tubing, which equilibrates quickly with surrounding material. Because of this, sensors were nearly equilibrated by the end of the useful measurement window, and extrapolation to full equilibration was relatively insensitive to model parameters (thermal conductivity, thermal diffusivity, time shift to improve model fit). The greatest source of uncertainty in equilibrium temperature (0.001-0.006 °C) came from selection of alternative measurement windows used for extrapolation to *in-situ* conditions.

2.2.2 Thermal conductivity

Sediment was recovered with a gravity corer in a 5.5 cm diameter polycarbonate liner through the same borehole adjacent to the thermal gradient measurements (sediment core WGZ-GC-1). Thermal conductivity, *k*, was measured in the laboratory on a 55 cm section of this core, using the needle probe method [*Von Herzen and Maxwell*, 1959], with measurements made every 1 cm for 40 cm. For each measurement, we drilled a 1.6-mm-diameter hole through the core liner, stopping before penetrating the core itself. We placed a 5-cm-long needle probe, containing a thermistor and heater wire, through the hole and into the sediment, perpendicular to the axis of the core. Constant heating was applied, and the temperature rise during the first 10 to 50 s followed a consistent ln(time) trend and was used for interpretation. The standard deviation of individual *k* values, based on fitting of data to a model of line-source heating, was ±0.0025 $Wm^{-1}{}^{\circ}C^{-1}$, and tests made with the same sized core liner filled with water solidified by gelatin yielded values consist with water ±5%. We interpret individual *k* values measured with the needle probe to have an uncertainty of ±5%, and applied corrections for the difference between core and laboratory temperatures, an adjustment of –0.193% $^{\circ}C^{-1}$ [*Morin and Silva*, 1984]. The effective conductivity of the core was calculated as the harmonic mean (± standard deviation of measurements), which is appropriate for vertical heat conduction through a heterogeneously layered system [*Bullard*, 1939]. This calculation is dominated by conductivity values on the lower end of the measured range, so is conservative when calculating the vertical heat flux, which is the product

of thermal gradient and thermal conductivity. We applied a geometric mean model for a two-phase media of solid and fluid to calculate apparent trends in sediment porosity from thermal conductivity data [*Brigaud and Vasseur*, 1989].

2.2.3 Grain size

Since variations in grain size can influence the thermal conductivity of sediments [*Gangadhara Rao and Singh*, 1999], we analyzed sediment samples to determine grain size, using the same core for which we measured thermal conductivity, in 1 cm depth increments. Grains with diameters <1 mm were analyzed with a laser-diffraction, particle size analyzer (PSA). The PSA uses light scattering to quantify particle size distribution within a liquid suspension, using a 5 mW laser source having a 750-nm wavelength. Samples were suspended in an eluent containing 0.1 g/L of sodium metaphosphate to deflocculate small particles, and circulated continuously during measurement. The result for each sample is a probability density function of grain sizes within 93 logarithmically-scaled bins ranging from <0.4 μm to <1 mm (Figure S2.4). To determine size fractions >1 mm which could not be analyzed with the PSA, samples were cut from the core and wet-sieved to isolate 1–2 mm and >2 mm diameter size classes, which were weighed (Figure S2.5). Results from the sieve and PSA methods were combined for each sample, assuming consistent grain density in the coarse and fine fractions.

2.2.4 Spatial variability in other heat flux terms at the ice sheet bed

To place the observed GHF variations in the context of other factors influencing the basal thermal energy balance of the ice sheet, we offer basal heat flux

estimates characteristic of the Siple Coast. To solve for the vertical conductive heat flux into the ice, q_i, we use the analytical solution of Robin [1955] for the 1-D thermal advection-diffusion equation. This solution assumes that the vertical velocity v_z decreases linearly from the accumulation rate at the surface to 0 at the ice sheet base (Text S2.2, Figure S2.6). We consider the steady-state case for an ice sheet in mass balance to gain insight into the most important terms in the basal thermal energy balance. We take the derivative of the Robin [1955] solution, to yield the temperature gradient at the base of the ice, $dT/dz|_b$, and multiply by the thermal conductivity of ice, k_i, to solve for q_i:

$$q_i = k_i \frac{dT}{dz}\Big|_b = k_i \frac{2(T_b - T_s)\sqrt{P/2}}{h\sqrt{\pi}\, erf\left(\sqrt{P/2}\right)} \quad (2.1).$$

T_b and T_s are the temperature at the base and surface of the ice sheet, respectively; h is the ice thickness; and P is the Peclet number, the ratio of thermal advection to diffusion, calculated as $ah\kappa^{-1}$ where a is the accumulation rate and κ is the thermal diffusivity. k_i is calculated as a function of temperature [*Cuffey and Paterson*, 2010].

In these calculations, we assume T_b is at the pressure melting point, $T_m(p)$, the maximum basal temperature for a frozen bed. Thus, these q_i such that $T_b$solutions represent a local upper bound on the vertical conductive heat flux through ice. $T_m(p)$ is calculated using freshwater properties [*IOC et al.*, 2010] and p is calculated as a function of ice thickness with an average ice density of 900 kg m^{-3} to account for the effects of air bubbles and firn.

Calculated q_i values depend mainly on three independent variables: ice thickness [*Fretwell et al.*, 2013], ice accumulation rate [*Arthern et al.*, 2006; *van de Berg et al.*, 2006], and mean annual surface temperature [*Comiso*, 2000] (error estimates in Table S2.6, sensitivity analysis in Figure S2.7). To illustrate the contribution of variability in each of these factors to variability in q_i, we present calculations of q_i along a profile near the Ross Ice Shelf grounding line, varying one factor while holding the rest at their average value across that profile ($\bar{a}$ = 12 cm yr^{-1}, $\bar{h}$ = 800 m, $\overline{T_s}$ = -21 °C).

We also present an estimate of heat production by friction between the ice sheet base and the subglacial stratum. This shear heating is the product of basal velocity and basal drag along flow. Yield strengths of till collected below the Whillans Ice Stream are a few kPa [*Tulaczyk et al.*, 2000]. Thus, the basal velocity approaches the surface velocity. In this calculation of the shear heat flux, we take basal velocity equal to the surface velocity, representing an upper bound on the shear heat flux. Since basal drag is poorly-constrained, we calculate shear heat flux profiles using a range of basal drag values from 2 to 10 kPa.

Although we do not account for heat sources and sinks due to freezing or melting and heat advection due to subglacial water flow, these are consistent with our calculated q_i, which is an upper bound given $T_b = T_m(p)$. This analytical approach neglects lateral ice advection, which may alter q_i within ice streams if lateral gradients in surface ice temperature are significant. However, along the Siple Coast surface temperature gradients are small [*Comiso*, 2000], and this analytical approach

reproduces the ice temperature profile reasonably well at SLW [*Fisher et al.*, 2015]. A more thorough analysis of this source of variability would entail 3-D ice sheet modeling.

2.3 Results and Discussion

2.3.1 GHF observations

Two measurements of the thermal gradient at the WGZ show good agreement, yielding a temperature gradient of 0.050 ± 0.004 °C m^{-1} (mean ± S.D.) (Figure 2.1; for the full record, see Figure S2.2 and Data Set S2.1). The thermal conductivity (*k*) of sediments collected at the site range from 1.6 to 2.1 W $m^{-1}°C^{-1}$, with local variations that are likely associated with differences in grain size [*Gangadhara Rao and Singh*, 1999] (Figure S2.4), grain lithology, and/or porosity [*Brigaud and Vasseur*, 1989] (Figure 2.1c, Data Set S2.2). There is no clear trend in *k* with depth, and we use the harmonic mean of measured *k* values, 1.77 ± 0.15 W $m^{-1}°C^{-1}$, to calculate GHF.

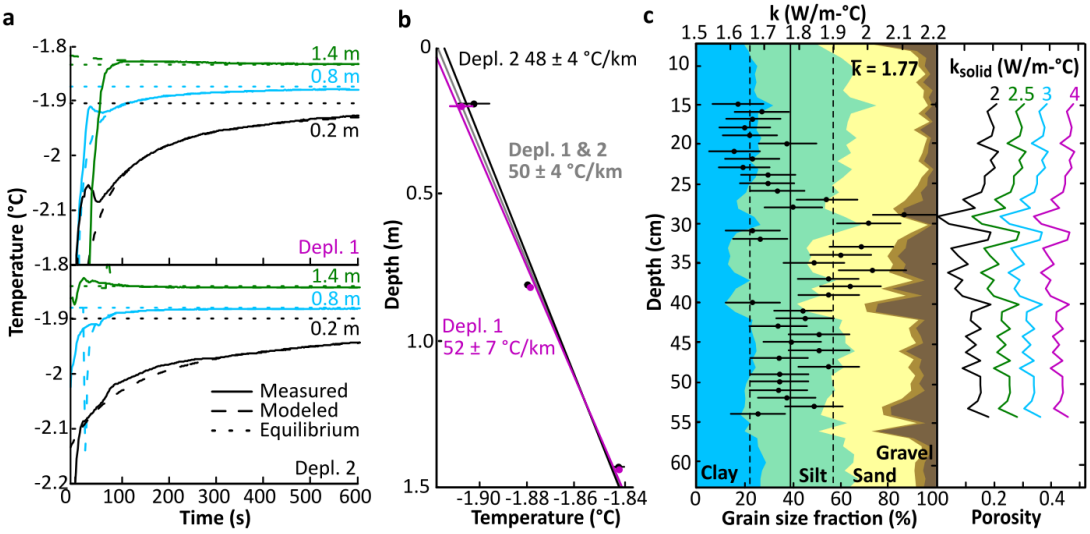

Figure 2.1. Temperature and thermal conductivity data from the WGZ. **a.** Temperature records for each sensor (depth in sediments labeled) during two geothermal probe deployments starting at the time of sediment penetration. **b.** Thermal gradient for each deployment and for the combined dataset constrained by equilibrium temperatures ± 1 S.E. **c.** Thermal conductivity (k) of sediments with ±5% errors and combined harmonic mean (labeled, solid vertical line) ± 1 S.D. (dashed lines). Cumulative grain size fractions indicated in color; gravel fraction is divided at 1 mm diameter. Inferred porosity for constant grain thermal conductivities (k_{solid}).

At the WGZ, the vertical, conductive GHF is 88 ± 7 mW m^{-2} (mean ± 1 S.E., Table S1). The shallowest equilibrium sediment temperatures have the largest uncertainties (Figure 2.2b), perhaps because of disruption of shallow sediments by probe insertion. If these data are omitted, then the geothermal gradient is ~18% greater, and GHF is 104 ± 3 mW m^{-2}. In contrast, the same tools and methods were applied at SLW, ~100 km away, yielding GHF of 285 ± 80 mW/m^2 [*Fisher et al.*, 2015]. An earlier measurement below the Ross Ice Shelf at J9, ~200 km from the WGZ, indicated GHF of 55 mW m^{-2} (Figure 2.2) [*Foster*, 1978].

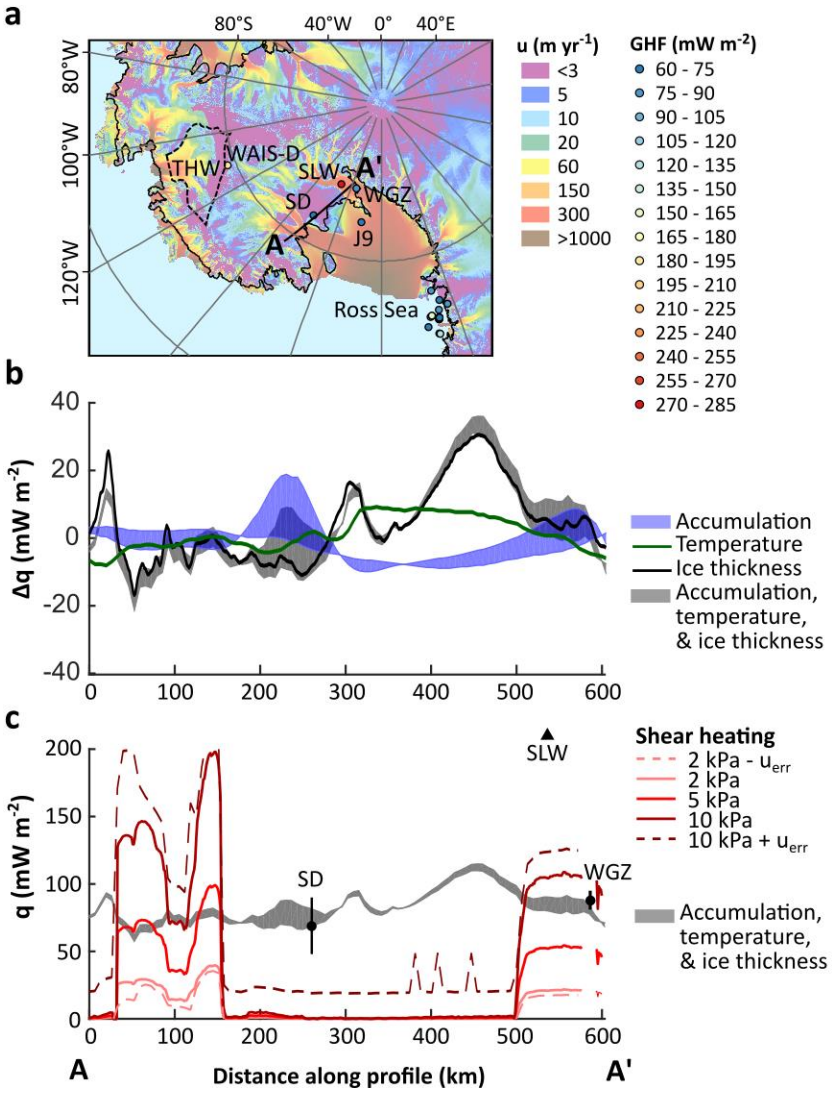

Figure 2.2. a. GHF measurements and estimates for West Antarctica [*Foster*, 1978; *Engelhardt*, 2004; *Fudge et al.*, 2013; *Fisher et al.*, 2015] and the Western Ross Sea region [*Morin et al.*, 2010 and references therein; *Schröder et al.*, 2011] overlain on ice velocity [*Rignot et al.*, 2011]. Grounding line outlined in black [*Bindschadler et al.*, 2011]. Profile line (A-A') shown in black. Extent of GHF estimates below Thwaites Glacier (THW, dashed line) [*Schroeder et al.*, 2014]. **b.** Estimates of spatial variability in heat conduction and production along the profile line shown in (a), as difference from mean conductive heat flux along that profile (79 mW m^{-2}). **c.** Shear heat flux estimates calculated from ice velocity and associated errors. GHF measurements and estimates close to the profile line are plotted (mean ± 1 S.E., SLW value lies off-axis).

2.3.2 Processes contributing to elevated and variable GHF in West Antarctica

There are a number of factors that can contribute to elevated and/or variable GHF, acting over a range of length scales (Table 2.1). We examine each of these factors to determine which could explain large variations in GHF (200 mW m^{-2}) over relatively short distances (≤100 km), as observed below the Whillans Ice Stream. The spatial scales of crustal thickness variability are too broad and the magnitude of resulting GHF deviations too small to explain the observed GHF variability [*Fox Maule et al.*, 2005; *Chaput et al.*, 2014] (Text S2.1c, Fig 2.3a). Thermal conductivity variability can produce small-scale GHF variability by conductive refraction, but the maximum difference in GHF is 30 mW m^{-2} (Text S2.1a). While variability in crustal radiogenic heat production can produce small-scale GHF variability as well, it is unlikely to enhance GHF by more than 18 mW m^{-2} (Figure 2.2a, Text S2.1b) [*Vilà et al.*, 2010]. Erosion and lithospheric extension in West Antarctica produce small rates of vertical advection that enhance GHF by ≤10 mW m^{-2} (Text S2.1d,e) [*Lachenbruch*, 1978; *Mancktelow and Grasemann*, 1997].

Table 2.1. Observational constraints on GHF variability and candidate explanations.

	Magnitude of GHF difference (mW m-2)	Lateral extent of GHF difference (km)
Observations (SLW-WGZ)	197 ± 85	108
Observations (WGZ-J9)	33 ± 7	228
Candidate explanations		
Hydrothermal circulation	1000s	0.1 – 100s

Magmatic intrusion	1000s	<10
Crustal thickness variability	≤60	>130
Thermal conductivity variability	<30	>1
Radiogenic heat production	≤18	<20
Lithospheric extension	≤10	≥75
Erosion	<4	10 – 200

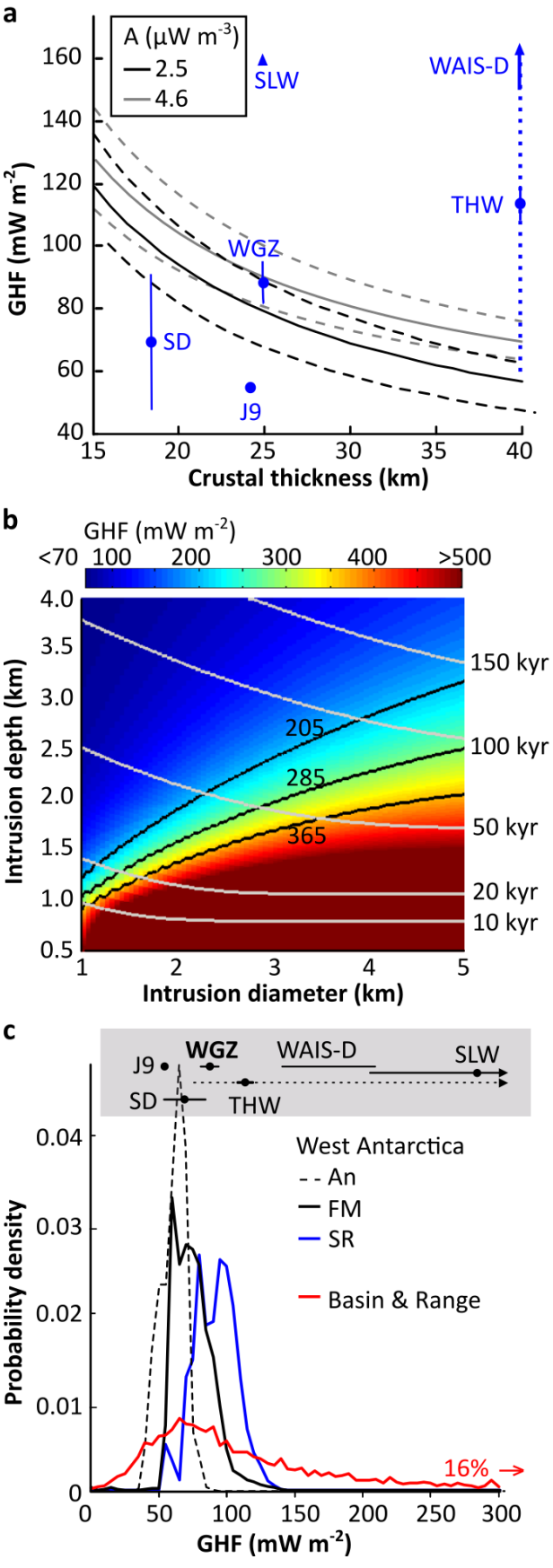
a
A (μW m-3)
2.5
4.6
SLW
WAIS-D
THW
WGZ
SD
J9
GHF (mW m-2)
Crustal thickness (km)
b
GHF (mW m-2)
<70 100 200 300 400 >500
Intrusion depth (km)
Intrusion diameter (km)
205
285
365
150 kyr
100 kyr
50 kyr
20 kyr
10 kyr
c
J9
WGZ
WAIS-D
SLW
SD
THW
West Antarctica
An
FM
SR
Basin & Range
16%
Probability density
GHF (mW m-2)

Figure 2.3. **a.** Analytical model for GHF based on Fox Maule *et al.* [2005] (black and grey lines) compared with GHF measurements and estimates (blue) as a function of magnetic crustal thickness. The SLW value lies well above the plot. Dotted lines show the envelope of ±15% variation in crustal thermal conductivity from 2.8 W $m^{-1}°C^{-1}$. **b.** GHF anomaly due to modeled magmatic intrusions with cubic geometry. Intrusion depths are the distance from the surface of the crust to top of the intrusion. GHF values are the maximum achieved at the surface over the center of the intrusion. Black contours represent mean ± 1 S.E bounds on GHF at SLW. Grey contours mark the time since emplacement at which the maximum GHF values plotted are achieved. **c.** Probability density functions of GHF models for West Antarctica [*Shapiro and Ritzwoller*, 2004; Fox *Maule et al.*, 2005; *An et al.*, 2015] and GHF measurements in the Basin and Range Province, USA, 16% of which exceed 300 mW m^{-2} [*National Geothermal Data System*]. **a and c.** GHF measurements and estimates for West Antarctica plotted as mean ± 1 S.E., where available (references in Figure 2.2). GHF estimates below Thwaites Glacier (THW), shown in Figure 2.3a, plotted as mean, ± 1 S.D. (solid line), and the full range of THW values (dotted line) which extends off-axis to 375 mW m^{-2} [*Schroeder et al.*, 2014].

Two remaining processes could generate the observed spatial variability in GHF: (a) recent magmatism at shallow crustal depths, and/or (b) advection of heat by crustal fluid flow, potentially associated with hydrothermal circulation. The influence of magmatic intrusions on GHF is estimated using the analytical, transient solution of Lachenbruch *et al.* [1976] for a prismatic intrusion (Figure 2.2b). In this model, the thermal conductivity of the surrounding crust is homogeneous and set to 2.8 W $m^{-1}°C^{-1}$, the initial temperature of the intrusion is set to 1000°C, and the background GHF at the surface outside of the influence of the intrusion is set to 70 mW m^{-2}. GHF values in excess of 200 mWm^{-2} are reached as a result of intrusions <5 km in diameter emplaced within the last 150 kyr. These intrusions can generate elevated GHF with spatial footprints less than 10 km [*Lachenbruch et al.*, 1976]. Geophysical observations have been interpreted as indicating extensive magmatism within the West Antarctic Rift System (WARS) [*Behrendt et al.*, 1994; *Trey et al.*, 1999;

Decesari et al., 2007; *An et al.*, 2015], including volcanism within the last several decades [*Blankenship et al.*, 1993; *Corr and Vaughan*, 2008; *Lough et al.*, 2013]. Magmatic intrusions in the lower crust are thought to cause geothermal gradients of 50-100 °C km^{-1} in McMurdo Volcanic Province [*Berg et al.*, 1989] (Figure S2.9), a range that overlaps with the geothermal gradient of 91-162 °C km^{-1} measured at SLW [*Fisher et al.*, 2015].

The flow of crustal fluids can also increase GHF within a broad area or redistribute heat locally, depending on fluid pathways, flow rates, and the depth of circulation [*Fisher and Harris*, 2010]. Hydrothermal circulation in basement rocks, even below sediments, can generate GHF anomalies with spatial scales of several to tens of kilometers [e.g., *Fisher et al.*, 1990; *Davis et al.*, 1997]. Vigorous local convection can lead to isothermal conditions in a buried aquifer, resulting in large differences in GHF (several hundred mW m^{-2}) through overlying strata as a function of depth to the aquifer top [*Davis et al.*, 1997; *Spinelli and Fisher*, 2004]. Where basement is exposed at the base of the ice, it may provide a conduit for discharge and recharge of hydrothermal fluids, increasing and decreasing GHF, respectively [e.g., *Davis et al.*, 1992; *Villinger et al.*, 2002; *Fisher et al.*, 2003]. The magnitude of GHF anomalies where basement outcrops at the surface can be several W m^{-2}, relative to background values of ~100 mW m^{-2} [e.g., *Davis et al.*, 1992; *Villinger et al.*, 2002; *Fisher et al.*, 2003]. The gravity data collected at WGZ suggests that basement topography may exist [*Muto et al.*, 2013], but there is no such evidence at SLW. The gravity data is consistent with a crustal fault, which could enhance permeability by

several orders of magnitude relative to unfaulted bedrock [*Seront et al.*, 1998], focusing vertical fluid advection and elevating GHF. Thus, either magmatism or advection of heat by fluids may contribute to high and spatially-variable GHF in West Antarctica.

These two processes have also played a role in generating GHF variability in other rift systems [*Reiter et al.*, 1975]. The observed variability of the GHF in West Antarctica is consistent with that of other rift systems [*Davies and Davies*, 2010] such as the Basin and Range Province of North America, which is often considered to be a geologic analog for the WARS in terms of the scale, degree of extension, and present crustal thickness [*Coney and Harms*, 1984; *Trey et al.*, 1999]. Currently available GHF constraints are consistent with the broad distribution of GHF values in the Basin and Range Province, 16% of which exceed 300 mW m^{-2} (Figure 2.3c). The apparent spatial correlation between rift basins and ice streams in West Antarctica [*Anandakrishnan et al.*, 1998; *Decesari et al.*, 2007; *Bingham et al.*, 2012] suggests that rifting-related processes such as magmatism or preferential advection of crustal fluids may affect ice dynamics by enhancing GHF.

2.3.3 Implications of high and variable GHF for slow-flowing ice

Given that GHF measurements reveal a wide range of variability, from tens of mW m^{-2} over distances of ~200 km (WGZ, J9, SD) to ~200 mW m^{-2} over ~100 km (WGZ, SLW), we compare this variability with independent estimates for the variability in heat flux on the Siple Coast (Figure 2.2b).

Estimated lateral variations in the vertical conductive heat flux are dominated by spatial variations in ice thickness. Calculated fluxes increase by 7 mW m^{-2} per 100 m decrease in ice thickness, resulting in spatial variations of 7-28 mW m^{-2} over 100 km from interstream ridge to ice stream trough. In contrast, estimated lateral variations in the vertical conductive heat flux due to changes in accumulation rate are generally <10 mW m^{-2} per 100 km. Estimated lateral variations in the vertical conductive heat flux due to changes in surface temperature are generally <5 mW m^{-2} per 100 km. The frictional heat flux due to ice sliding over subglacial sediments is poorly-constrained due to uncertainties in basal resistance and basal sliding velocity, but is estimated to be <125 mW m^{-2} near WGZ where ice velocity is around 300 m yr^{-1}. These sources of variability in heat flux are less than the spatial variability in GHF of ~200 mW m^{-2} per 100 km (WGZ, SLW) and of the same magnitude as the spatial variability between other GHF estimates (WGZ, J9, SD).

2.4 Conclusions

Current geophysical GHF models underestimate the observed magnitude and spatial variability of GHF, which may be enhanced by magmatism or advection of crustal fluids. Large differences in sea level rise predictions from Antarctica result from two GHF models with narrow GHF distributions [*Bougamont et al.*, 2015]. The observed spatial variability in GHF raises the possibility that GHF plays a greater role in ice dynamics than generally considered. Zones of elevated GHF below the WAIS can produce considerable volumes of subglacial meltwater [*Vogel and Tulaczyk*, 2006] and may contribute to the development and dynamics of subglacial lakes, the

advection of organic and inorganic compounds into subglacial habitats, and thus the presence and metabolism of microbial biomes [*Jørgensen and Boetius*, 2007; *Christner et al.*, 2014]. Seroussi *et al.* [2017] found that locally high GHF (≥150 mW m^{-2}) below the Whillans Ice Stream was needed to reproduce the observed subglacial lakes in an ice sheet model. As the ice sheet thins, increasing the vertical conductive heat flux, GHF variability may be more important to predictions of the basal thermal regime, particularly the development of basal frozen zones such as ice rises that might stabilize ice retreat [*Rignot et al.*, 2004; *Favier and Pattyn*, 2015].

Bed topography and ice sheet thickness are relatively well-constrained for much of West Antarctica [*Fretwell et al.*, 2013]. Spatial variability in GHF may contribute more to the uncertainty in the basal thermal regime of West Antarctica than does the remaining uncertainty in ice thickness, which is equivalent to GHF uncertainty of 4 mW m^{-2} along the Siple Coast (Table S6). More direct GHF observations are needed to constrain continental GHF models. Ice sheet modeling could direct GHF observations to locations where future ice sheet mass balance is most sensitive to GHF, to maximize the impact of field measurements. Until such observational constraints become available, we recommend running ensembles of ice sheet models for multiple spatial distributions of GHF below the WAIS, including distributions as broad as that in the Basin and Range Province, to set more realistic limits on rates of ice loss.

Data availability

The geothermal heat flux and thermal conductivity measurements are available in the Global Heat Flow Database, and Data Sets S1 and S2. Grain size data are available in the EarthChem Library, (Branecky Begeman, Carolyn; Tulaczyk, Slawek M.; Fisher, Andrew T. (2017): Grain Size Data for Sediment Core WGZ-GC-1), and Data Set S2. The vertical conductive flux estimates are available in figshare doi: 10.6084/m9.figshare.5414062. The authors declare that all other data supporting the findings of this study are available within the paper and its supplementary data files. The methods used to analyze sediment core WGZ-GC-1 were destructive, so samples are not available for further analysis. The following datasets were used in this study: bed elevation available at https://nsidc.org/data/docs/daac/nsidc0422_antarctic_1km_dem/, ice thickness available at https://legacy.bas.ac.uk//bas_research/data/access/bedmap/database/, accumulation and mean annual surface temperature available at http://websrv.cs.umt.edu/isis/index.php/Present_Day_Antarctica, and GHF data from the Basin and Range Province available at http://geothermal.smu.edu/gtda/.

Chapter 3 The volcanic response to deglaciation: a role for magma chamber dynamics

Abstract

The frequency of volcanic eruptions increased during the last deglaciation, between 15,000 and 10,000 years ago. Will volcanic eruptions be more frequent under present-day glacier retreat rates? We use a thermomechanical magma chamber model to determine what conditions make volcanoes sensitive to surface load changes. Our methodology advances the study of this problem by including phase changes in the magma chamber, the viscoelastic response of the chamber-crust system, and load-induced changes in the critical overpressure for dyke initiation, which have previously been considered in isolation. While a change in the critical overpressure for dyke initiation may dominate the eruptive response to deglaciation at high magma recharge rates, magma chamber dynamics have a significant influence on eruption frequency under lower magma recharge rates and higher crustal relaxation rates. Pressure-dependent volatile exsolution contributes significantly to magma pressurization when it triggers a positive feedback with viscous relaxation. Our sensitivity analysis of magma chambers undergoing surface load changes can help guide future studies of the magmatic response of ice-covered volcanoes.

3.1 Introduction

Statistically, the global frequency of volcanic eruptions increased during the last deglaciation (Huybers & Langmuir, 2009; Kutterolf et al., 2013). This observation, and supporting local observations from glaciated regions (Bacon &

Lanphere, 2006; Glazner et al., 1999; Jellinek et al., 2004; Praetorius et al., 2016; Rawson et al., 2016; Watt et al., 2013), suggest that subaerial volcanism is anticorrelated with ice volume. Submarine volcanism, on the other hand, shows a positive correlation with ice volume, consistent with a local decrease in crustal load as sea levels fall (Tolstoy, 2015). Possible feedbacks between volcanism and glacial cycles are a priority for the research community, according to a report commissioned by the National Academy of Sciences (Committee on Improving Understanding of Volcanic Eruptions et al., 2017, henceforth ERUPT17). These feedbacks may include increased volcanic greenhouse gas emissions (McKenzie et al., 2016), enhanced ice melting from geothermal heat or the heat of erupted debris (Jarosch & Gudmundsson, 2007; Julio-Miranda et al., 2008), and decreased ice albedo from eruptive debris on the ice surface (Rivera et al., 2006). To assess the strength of these feedbacks, we investigate the strength of the volcanic response to deglaciation and the processes that allow a response.

If volcanoes responded to ice retreat during the last deglaciation, could they respond to present-day ice retreat (Tuffen, 2010; ERUPT17)? The volcanic response to ice loss is a particularly relevant area of investigation given the acceleration of glacial ice loss observed in the last century (Jomelli et al., 2009; Marzeion et al., 2012; Thompson et al., 2009), not only for climate dynamics but also for predicting volcanic hazards. Volcanic hazards can be enhanced in the presence of ice or snow, for example, by the formation of lahars from interactions between pyroclastic density currents and ice (Pierson et al., 1990) and floods of glacial meltwater (jökulhaups)

(Major & Newhall, 1989). Thus, it is important to identify which volcanoes are most likely to be affected by ice retreat.

To determine the characteristics that make volcanoes sensitive to ice loss, we need to understand the mechanisms responsible for increased eruption frequency during the last deglaciation. Proposed mechanisms for this response fall into two broad categories: controls on magma supply to the crustal reservoir and controls on magma storage in the crustal reservoir. Deglaciation has been proposed to increase magma supply to the magma plumbing system through mantle decompression melting (Jull & McKenzie, 1996; Maclennan et al., 2002; Pagli & Sigmundsson, 2008) and to enhance melt migration through the lithosphere (Stevens et al., 2016). Controls on magma storage may include decompression-induced volatile exsolution (Tuffen et al., 2010) and crustal stress changes that make dyke initiation or propagation more favorable. Deglaciation directly causes crustal stress changes by changing the ice load and may also trigger further crustal stress changes. These indirect effects may include hydrologic changes that promote motion along existing weaknesses (Capra, 2006), thermal perturbations that contribute to edifice collapse (Huggel et al., 2008), fault motions that relieve crustal stress (Hall, 1982), and glacial erosion (Sternai et al., 2016).

Crustal stress changes at and around the magma reservoir are ubiquitous features of ice unloading. Previous studies of the elastic and viscoelastic response to an unloading event indicate that the primary effect is to promote dyke initiation for a broad range of magma chamber conditions and load geometries (Albino et al., 2010;

Pagli et al., 2007; Sigmundsson et al., 2010). While these studies include the direct change in magma chamber pressure due to unloading, they have not addressed the dynamic magma chamber pressure response to unloading. The relative importance of magma chamber dynamics compared with the change in threshold for dyke initiation to the deglacial magmatic response is unclear.

Magma chamber pressure can have a nonlinear response to glacial loading and unloading as a result of the coupled evolution of magma chamber pressure, volume, and density through phase changes and the viscoelastic response of the chamber-crust system (Jellinek et al., 2004; Jellinek & DePaolo, 2003), crystallization, and volatile exsolution. Volatile exsolution may be particularly important to the magmatic response by changing the bulk density and compressibility of the magma chamber. It also has implications for volcanic hazards, affecting eruption explosivity (Wilson et al., 1980) and magma viscosity (Friedman et al., 1963). We hypothesize that the magmatic response to deglaciation, specifically the eruption frequency, is influenced by these dynamics. To evaluate this hypothesis, we simulate magma chamber response to glaciation and deglaciation with a thermomechanical magma chamber model that includes these nonlinear effects (Degruyter & Huber, 2014, henceforth DH14), and compute changes in eruption frequency due to loading and unloading.

This study addresses another research priority identified by the ERUPT17 report – the processes that trigger eruptions. While there are clear examples of rapid, high magnitude unloading events, such as edifice collapse, triggering eruptions (Moore & Albee, 1981; Voight, B. et al., 1981), it is not clear if slow, low magnitude

unloading events, such as present-day mountain glacier retreat, can trigger eruptions. Although the focus of this study is ice mass changes, the results of this study can be applied to magma chamber evolution under other sources of crustal stress change, such as edifice construction and erosion. This numerical approach allows us to identify "critical thresholds in processes and physical properties that govern shifts in eruptive behavior" (ERUPT17). We use the model to assess whether glacial cycles can shift magma chambers between eruptible and uneruptible states, and to identify the conditions under which magma chambers are most sensitive to deglaciation. These results can help identify volcanoes that have strong climate coupling and thus might respond to present-day ice retreat.

3.2 Methods

3.2.1 Thermomechanical magma chamber model

We simulate magma chamber evolution under load changes with the box model developed by DH14. The model is presented briefly here and in Text S3.1; we refer readers to DH14 for further details. In this model the magma chamber is homogeneous and composed of three phases: magma melt, exsolved gas and crystals. The mass flux of magma melt with 5 wt% dissolved water to the chamber is constant and thus assumed independent of pressure conditions in the chamber or surrounding crust. Although this assumption is not necessarily justified, it allows us to evaluate the sensitivity of magma chamber processes to surface load changes independent from controls on magma recharge. The mass flux out of the chamber is zero except

when an eruption is occurring, during which it exceeds the mass flux into the chamber until the chamber pressure is equal to the crustal pressure.

Total mass, water mass, and enthalpy are all conserved. Melt, gas and crystal phases are assumed to be in thermodynamic equilibrium. The temperature evolution of the magma chamber is governed by magma fluxes, heat conduction to the crust, latent heat of crystallization and exsolution, and pressure-volume work. Since the magma chamber is homogenous, we cannot represent compositional zonation, stratification or heterogeneity in the enthalpy field that may affect magma dynamics. The chamber becomes uneruptible when it is mechanically locked with crystals, assumed to occur when the crustal mass fraction is 0.5 (Marsh, 1981).

Water is the only volatile considered, and thus the gas phase represents water in a supercritical fluid state. Water exsolution is expected to dominate the eruptive response over other volatiles, as it is more soluble than carbon dioxide (Tait et al., 1989). Phase changes in the magma chamber affect the compressibility, density of the magma chamber and its enthalpy balance. Exsolution is assumed to be in thermodynamic equilibrium on the timescales of ice load change. The magma chamber is a closed-system between eruptions; that is, there is no gas escape. Thus, our results represent an upper bound on the exsolution contribution to magma pressurization. An exsolution response during deglaciation could also be limited by the availability of dissolved volatiles, which is not a limiting factor in our simulations with water-saturated magma (at 5 wt% water).

The pressure evolution of the magma chamber is governed by the magma fluxes, the viscoelastic response of the chamber-crust system, thermal expansion and density changes. Viscoelastic deformation of the crust and eruption timing are governed by magma chamber overpressure. Magma chamber overpressure is the amount by which magma chamber pressure exceeds the pressure in the crust:

$$\Delta P_{ch} = P_{ch} - P_{crust} \quad (3.1)$$

where P_{cr} is the lithostatic pressure. The evolution of magma chamber volume is described by

$$\frac{1}{V}\frac{dV}{dt} = \frac{1}{E}\frac{dP_{ch}}{dt} + \frac{\Delta P_{ch}}{\eta} - \alpha\frac{dT}{dt} \quad (3.2)$$

where E is the bulk modulus of the crust, η is the effective viscosity, and α is the coefficient of thermal expansion. The pressure evolution in the magma chamber corresponds to a spherical chamber under radially symmetric deformation.

The model simulates an eruption when the magma chamber pressure exceeds the fracture pressure, P_{crit}, the threshold for dyke initiation. Thus, whenever a dyke is initiated it is presumed to result in an eruption. The critical magma chamber overpressure for eruption, ΔP_{crit}, is:

$$\Delta P_{crit} = P_{crit} - P_{crust} \quad (3.3)$$

ΔP_{crit} may range from 1 to 85 MPa (Grosfils, 2007; Gudmundsson, 2006; Rubin, 1995), and in the model is set at 20 MPa. In principle, the eruption frequency sensitivity to loading and unloading is independent of the initial critical magma overpressure chosen (Text S3.2). However, because pressure-dependent phase

changes are non-linear functions of pressure, the modeled sensitivity could vary with initial critical magma overpressure.

We are concerned with eruption periods ranging from several years to 40 kyr, the Milankovitch frequency, which we consider to be a reasonable threshold for a contribution to glacially-modulated changes in eruption frequency. In this model, we simulate eruptions triggered by mass injection and second boiling. We do not simulate eruptions triggered by buoyancy, but this mechanism is thought to be important only for long eruption periods, $O(10^5)$ years (Caricchi et al., 2014), longer than the eruption periods we consider.

The model solves a system of coupled ordinary differential equations for conditions inside the magma chamber: pressure, temperature, the volume fractions of different phases, chamber volume, melt density, and crystal density. The gas density, crystal fraction, dissolved water mass fraction, and melt fraction are then obtained by an equation of state for water (Huber et al., 2009), a melting curve (Huber et al., 2010), a solubility model for water (Dufek & Bergantz, 2005), and the closure condition that the volume fractions of each phase sum to 1, respectively. The pressure-dependence of water solubility in melt is important for evaluating glacially-triggered volatile exsolution and is shown in Figure S 3.1.

We use the MATLAB solver *ode15s* which is appropriate for stiff problems and conducts adaptive time-stepping based on the convergence characteristics of each attempted solution. The absolute error tolerance and relative error tolerance are set to 10^{-5}. Typical time steps are 10-60 days. The model is consistent with an earlier and

simpler model of spherical magma chamber pressure evolution including viscoelasticity, crystallization and exsolution (DH14; Tait et al., 1989).

Several characteristic magma chamber timescales introduced by DH14 are diagnostic:

a magma recharge timescale,

$\tau_{in} = \frac{\rho_0 V_0}{\dot{M}_{in}} = \frac{4\pi}{3}\frac{\rho_0 R_0^3}{\dot{M}_{in}}$ (3.4),

a chamber cooling timescale,

$\tau_{cool} = \frac{R_0^2}{\kappa}$ (3.5),

a crustal relaxation timescale,

$\tau_{relax} = \frac{\eta_0}{\Delta P_{crit}}$ (3.6).

and the ratios of these timescales,

$\theta_1 = \tau_{cool}/\tau_{in}$ (3.7)

$\theta_2 = \tau_{relax}/\tau_{in}$ (3.8).

Eruptions can be triggered by mass injection or second boiling. The second boiling regime is characterized by exsolution induced by crystallization that enriches the melt in volatiles. As the gas phase is less dense, exsolution leads to a volume increase that pressurizes the magma chamber. Second boiling dominates magma pressurization over mass injection when $\tau_{cool} < \tau_{in}$, and mass injection dominates when $\tau_{cool} > \tau_{in}$. DH14 found that no eruptions occur when magma pressurization is balanced by viscous relaxation of the crust, $\tau_{in} > \tau_{relax}$ for the mass injection regime and $\tau_{cool} > \tau_{relax}$ for the second boiling regime.

3.2.2 Stress modification by glacial loads

Rather than model the stress transmission in the crust from the ice base to the magma chamber (Albino et al., 2010; Bakker et al., 2016), which has been examined by previous studies, we use the insights from these studies, reviewed in Text S3.3, to prescribe stress perturbations at the magma chamber wall and to the magma pressure. Three pressure terms in the model are affected by loading or unloading. Each term is expressed as a combination of an initial pressure state and a loading or unloading component designated with the "load" subscript.

$$P_{crust} = P_{crust,0} + P_{crust,load} \quad (3.9)$$

$$P_{ch} = P_{ch,0} + P_{ch,load} \quad (3.10)$$

$$P_{crit} = P_{crit,0} + P_{crit,load} \quad (3.11)$$

P_{crust} is the lithostatic pressure, P_{ch} is the magma chamber pressure, and P_{crit} is the fracture pressure. The initial values is designated by a "0" subscript and the loading or unloading component is designated by a "load" subscript (Figure 3.2). All pressure-dependent terms in the magma chamber model are modified to include the load component, $P_{ch,load}$. Loading suppresses dyke initiation, and thus eruption, when $P_{crit,load} - P_{ch,load} > 0$, and promotes dyke initiation when $P_{crit,load} - P_{ch,load} < 0$.

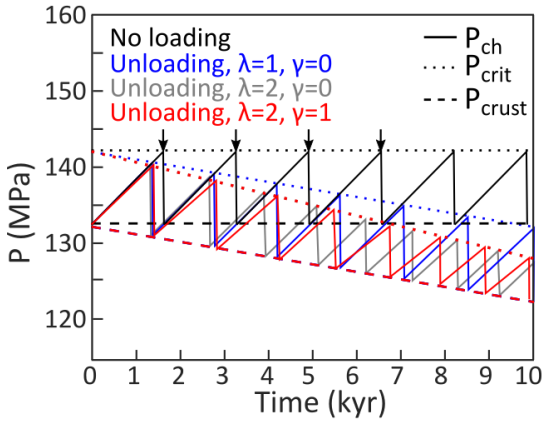

Figure 3.1. Load-induced modifications to compressive stress in the crust (P_{crust}), magma chamber pressure (P_{ch}) and fracture pressure (P_{crit}) are shown schematically. The constant load case is shown in black. Blue, red, and grey curves show the effects of varying load parameters (λ, γ) under a constant unloading rate of 1 MPa kyr^{-1}.

Glacier thickening or thinning induces a stress perturbation in the crust that decays with depth (e.g., Jeffery, 1921). We do not model this process and instead prescribe the crustal pressure, P_{crust}, at the depth of the magma chamber. In our discussion of the model results we assume that an increase in P_{crust} corresponds to an increase in ice thickness and a decrease in P_{crust} corresponds to a decrease in ice thickness. This positive correlation is generally true for magma chamber depths that are less than 2 times the loading radius (Pinel & Jaupart, 2000).

We approximate the change in fracture pressure as a linear function of the change in crustal pressure:

$$P_{crit,load} = \lambda P_{crust,load} \quad (3.12)$$

where λ is a scaling coefficient. The elastic finite element modeling of Albino et al. (2010) indicates that this is a reasonable approximation if the loading radius is at least 2 times the magma chamber radius and the magma chamber is at least 1 km from the

surface. λ is greater than 1 when the magma chamber is spherical or prolate ellipsoid, the loading radius is at least 2 times the magma chamber radius (as before), and the magma chamber radius is less than 2 times the magma chamber depth (regime diagram shown in Figure S3.2). Albino et al. (2010) report λ values from 1 - 2.5. For this study we set $\lambda = 2$ such that the change in critical magma overpressure is equal to the load. It follows from Equations 3.3, 3.9, 3.11 and 3.12 that

$$\Delta P_{crit} = \Delta P_{crit,0} + (\lambda - 1) P_{cr,load} \quad (3.13).$$

We also approximate the change in magma chamber pressure as a linear function of the change in crustal pressure:

$$P_{ch,load} = \gamma P_{cr,load} \quad (3.14)$$

where γ is a coefficient. γ is always positive because magma chamber pressure is always positively correlated with loading (Albino et al., 2010). This approximation is valid if the loading radius is at least 2 times the magma chamber radius (again as before), though γ should be a function of magma compressibility, which does change during our simulations. Since our magma chamber model includes the effects of magma compressibility on magma chamber pressure, it is reasonable to set $\gamma = 1$ and allow the model to respond to the crustal pressure perturbation.

The change in fracture pressure exceeds the change in magma overpressure for spherical and oblate ellipsoid magma chambers (Albino et al., 2010). Thus, previous studies have predicted that the net effect of loading is to suppress dyke initiation and the net effect of unloading is to enhance it. Since this model assumes that dyke initiation leads to eruption, loading increases eruption period and unloading

decreases eruption period. A schematic eruption record considering only magma recharge and eruption is shown in Figure 3.3. Since $\lambda > 1$, eruptions become more frequent as unloading progresses, in the absence of magma chamber dynamics.

For prolate ellipsoidal magma chambers, unlike spherical and oblate ellipsoidal magma chambers, the fracture pressure may increase with unloading, while the magma pressure decreases (Albino et al., 2010). Our model results are not directly applicable to these magma chamber geometries. Since these relationships rely on studies of idealized magma chambers in a lithostatic stress field, our model results may not reflect the response of magma chambers with complex geometries or where the stress field in the crust differs significantly from lithostatic.

3.2.3 Simulations

Whereas viscoelastic finite element models have often examined the instantaneous crustal stress response to loading and unloading, glaciation and deglaciation may be better captured by gradual loading and unloading. We choose loading and unloading rates at the magma chamber walls that are similar to the magnitude of change produced by modern deglaciation and gradual glaciation. Typical present-day thinning rates of mountain glaciers and ice caps are generally in the range 0.2 – 0.7 m yr^{-1} (Ragettli et al., 2016; Thompson et al., 2009; Tuffen, 2010). Ice thinning of 0.1 m yr^{-1} imparts a 0.9 MPa kyr^{-1} pressure rate of change at the surface of the crust. Thus, given the decay of the stress perturbation with depth in the crust, present-day ice thinning rates impart on the order of 1 MPa kyr^{-1} crustal stress change at the wall of an upper- to mid-crustal magma chamber. Ice thickening rates

could be 10-50% of the thinning rates, given the asymmetry seen in $\delta^{18}O$ proxy records of ice volume (Broecker, 1984). For this study, we consider normal stress changes at the chamber wall of 0.1-1 MPa kyr^{-1}. Although ice thinning rates can be much higher over short timescales with pulses of ice thinning reaching several m yr^{-1} (Carlson et al., 2008), we focus on this lower range of loading and unloading rates to address present-day ice retreat and to fill gaps in our understanding of eruption sensitivity to gradual changes.

We run several series of magma chamber simulations with load rates of -1, -0.1, 0, 0.1 and 1 MPa kyr^{-1}. To explore the parameters space, we randomly vary magma chamber properties within a pre-defined range: magma recharge from 10^{-2} to 10^{3} kg s^{-1}, chamber radius from 0.5 to 5 km, and crustal viscosity from 10^{19} to 10^{22} Pa s (n = 8533). To investigate the effect of viscous relaxation, we also run a set of simulations with an "elastic" end-member with crustal viscosity of 10^{60} Pa s (n = 1440).

The lithostatic pressure is chosen to be equivalent to a shallow crustal magma chamber, corresponding to a depth of 5 km given crustal density of 2700 kg m^{-3}. Since pressure-dependent phase changes are non-linear functions of pressure, the eruption frequency sensitivity to surface loading may vary with magma chamber depth. Shallower magma chambers might experience a stronger exsolution response to loading and unloading. Gas solubility in the melt is about 3 times more sensitive to pressure at 2 km depth (0.03% MPa^{-1}) than it is at 5 km depth, the depth of these

simulations (0.01% MPa^{-1}) (Huber et al., 2010). Other parameters are chosen according to a silicic magma chamber (Table 3.1).

Table 3.1. Variables and parameters of the thermomechanical magma chamber model.

Symbol	Definition	Value
c_m	Specific heat of melt	1200 J kg^{-1} K^{-1}
c_g	Specific heat of gas	3880 J kg^{-1} K^{-1}
c_{cr}	Specific heat of crustal rocks	1200 J kg^{-1} K^{-1}
L_e	Latent heat of exsolution	61 x 10^4 J kg^{-1}
L_m	Latent heat of melting	29 x 10^4 J kg^{-1}
$\dot{M}_{in}$	Mass inflow rate	10^1 - 10^3 kg s^{-1}
$\dot{M}_{out}$	Mass outflow rate	10^4 kg s^{-1}
$m_{eq,0}$	Dissolved water fraction of melt entering chamber	0.05
$\Delta P_{crit,0}$	Initial fracture pressure	20 MPa
$P_{crust,lith}$	Lithostatic pressure	133 MPa
R_{ch}	Chamber radius	0.5 - 5 km
T_0	Magma melt temperature entering chamber	1200 K
T_{liq}	Liquidus temperature	1223 K
T_{solid}	Solidus temperature	973 K
$\alpha_m, \alpha_x, \alpha_{cr}$	Melt, crystal, and crust thermal expansion coefficient	10^{-5} K^{-1}
$\beta_m, \beta_x, \beta_{cr}$	Melt, crystal, and crust bulk modulus	10^{10} Pa
γ	Magma pressure loading coefficient	1.0
$\varepsilon_{g,0}$	Initial gas volume fraction	0.04
η	Crustal viscosity	10^{19} - 10^{22} Pa s
κ	Thermal diffusivity of the crust	10^{-6} m^2 s^{-1}
λ	Fracture pressure loading coefficient	2.0
$\rho_{m,0}$	Melt density	2400 kg m^{-3}
$\rho_{x,0}$	Initial crystal density	2600 kg m^{-3}
ρ_{cr}	Crust density	2700 kg m^{-3}

3.3 Results

Eruptions are more frequent under simulated unloading conditions than under constant load conditions (Figure 3.2). The net effect of deglaciation is to enhance the flux of erupted magma by increasing eruption frequency (Figure S3.3). The change in eruption period in the mass-injection regime is generally less than 1% for load rates of 0.1 MPa kyr^{-1} and on the order of 10% for load rates of 1 MPa kyr^{-1}. The change in eruption period in the second-boiling regime ranges from 1 to 30% for load rates of 0.1 MPa kyr^{-1} and up to 75% for load rates of 1 MPa kyr^{-1}. Eruption periods are more sensitive to loading and unloading as the mass injection timescale increases or the cooling timescale decreases (i.e., second boiling becomes important) and as the relaxation timescale decreases. The patterns of sensitivity are similar for loading and unloading cases (Figure S3.4).

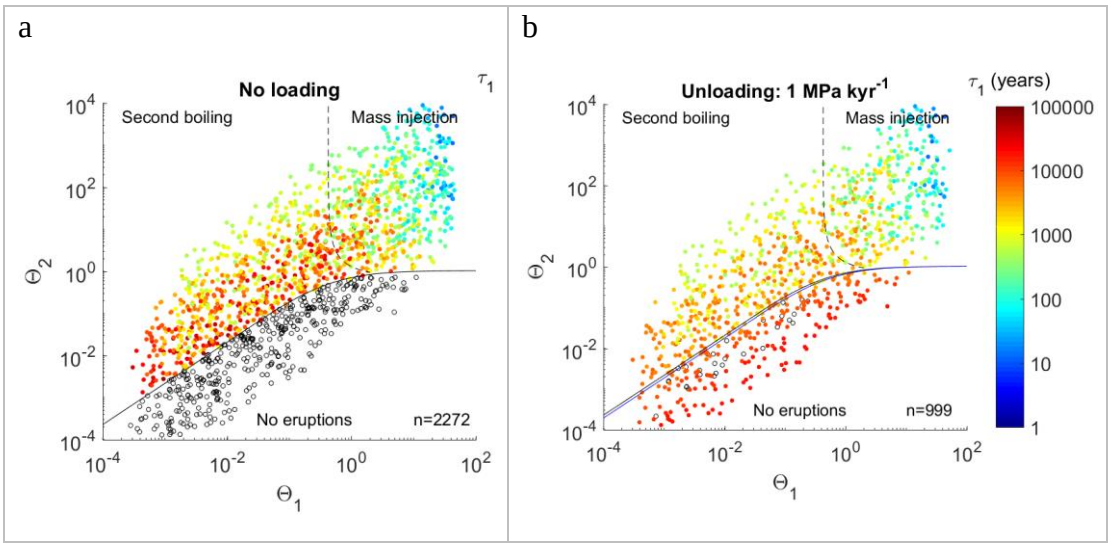

Figure 3.2. Comparison of eruption period between no loading and unloading cases. The black dashed line denotes the boundary between increasing (left) and decreasing (right) gas fraction through time. Empty black circles denote cases for which there is no eruption within 100 kyr of simulation time. The black subhorizontal line is the best fit to the eruption threshold for no loading cases. **a.** Initial eruption period with no

load change. Eruption period increases as the recharge timescale increases and as the relaxation timescale increases. **b.** Initial eruption period given loading rates of 1 MPa kyr^{-1}. The blue horizontal line is the best fit to the eruption thresholds for 0.1 MPa kyr^{-1} unloading.

Glaciation can change the conditions at which a magma chamber transitions from eruptible to uneruptible. Without load changes, there is a well-defined boundary in θ_1-θ_2 space at which the magma chamber transitions from eruptible to uneruptible, the eruption threshold:

$$\theta_2 = \frac{b_3\theta_1}{b_1\theta_1 + b_2 - 1} \quad (3.15)$$

where b_1, b_2 and b_3 are coefficients (DH14, Figure 3.4a). The values of these coefficients for our model parameters without load changes are 2.4, 2.1, and 2.5, respectively. For loading and unloading rates of 0.1 MPa kyr^{-1}, the threshold between eruptible and uneruptible magma chambers is well-characterized by Equation 3.16 but with a change in slope equivalent to a 20% change in b_2 (Figure 3.2b). This shift in eruption threshold is equivalent to changing the minimum viscosity to sustain eruptions changes by a factor of 1-5 depending on the chamber radius. However, for loading and unloading rates of 1 MPa kyr^{-1}, the eruption threshold is not well-described by Equation 3.16, as loading suppresses eruptions in magma chambers well above the threshold (Figure S3.4d) and unloading triggers eruptions in magma chambers well below the threshold (Figure 3.2b). Eruptions are more likely to be triggered from large magma chambers because of their longer crystallization timescales, resulting in low ΔP_{crit} at the time of eruption.

The percent change in eruption frequency due to loading or unloading is roughly proportional to the lithostatic stress change since the last eruption:

$$\phi_{load} \cong b\, dP_{cr,load} \quad (3.16)$$

where b_{total} is a coefficient with units of Pa^{-1} and ϕ_{load} is the fractional change in eruption period:

$$\phi_{load} = \frac{\tau_{load} - \tau_0}{\tau_0} \quad (3.17)$$

and τ_{load} is the eruption period in the presence of loading or unloading and τ_0 is the eruption period without loading given the same model input parameters. In a nearly elastic crust (high θ_2 values), b is equal to 0.1 MPa^{-1} (Figure 3.7a), with some misfit between Equation 3.16 and simulations due to changing magma compressibility. The sensitivity to load changes is much higher at faster relaxation timescales, as shown in Figure 3.7a where simulations with low Θ_2 values lie off the black line, and for simulations in which unloading triggers eruptions from a previously uneruptible magma chamber (Figure 3.3c).

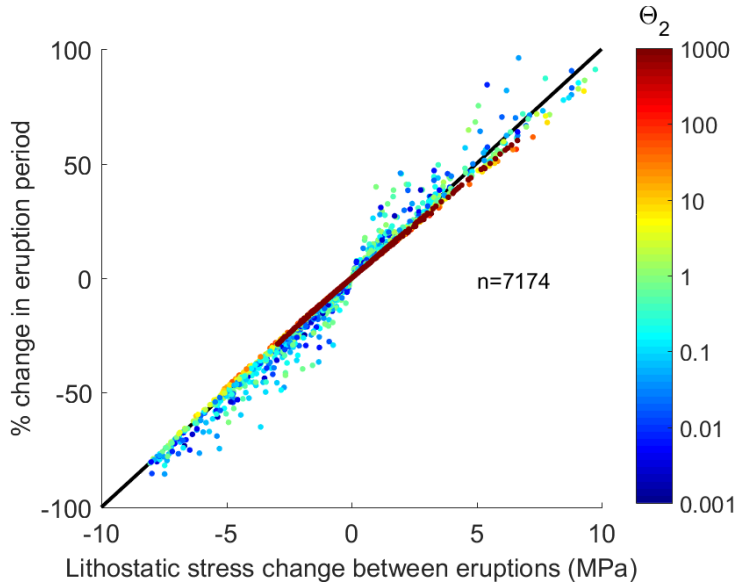

Figure 3.3. Sensitivity of the first eruption period to loading and unloading. Sensitivity is expressed as the fractional change in eruption period compared to the no-loading case for those model parameters. Each point corresponds to a simulation, colored by the ratio of relaxation time to recharge time (Θ_2). Black line corresponds to the fit to the "elastic" end-member simulations with an effective crustal viscosity of 10^{60} Pa s.

One might have assumed that magma chamber dynamics play a relatively small role in the magmatic response to glacial cycles, and that eruption frequency changes could be predicted by the change in fracture pressure alone. We show that this assumption is not valid. Even without a change in the fracture pressure (Series 2), the eruption period is sensitive to load changes (unloading decreases eruption period and loading increases eruption period (Figure 3.7b). Fracture pressure changes are responsible for only half of the sensitivity to loading and unloading, evidenced by 50% reduction in b_1 for cases without fracture pressure changes.

Deglaciation enhances eruption frequency through an increase in magma pressurization by second boiling. In our simulations, the decrease in magma pressure due to unloading is partially offset by the decompression volatile exsolution, and the

increase in magma pressure due to loading is partially offset by pressure-dependent volatile dissolution into the melt. By examining exsolution rates for a range of magma chamber conditions, we find that three dynamical regimes can be defined (Figure 3.8). Zone 1 is characterized by short mass injection timescales and load changes have a negligible effect on exsolution rates. For low to moderate recharge rates, load changes have a significant influence on exsolution rates (Zones 2 and 3). When the crustal viscosity is low, viscous relaxation modifies exsolution rates (Zone 3). Exsolution rates increase through time as viscous relaxation releases magma overpressure. By decreasing eruption periods, unloading reduces average exsolution rates in Zone 3 for most cases.

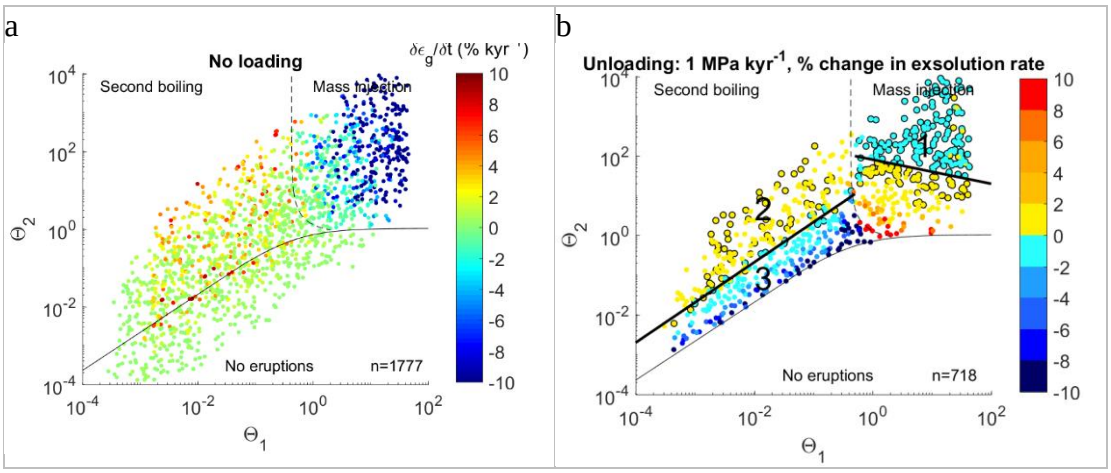

Figure 3.4. a. Exsolution rates without load changes. **b.** Percent change in exsolution rates due to unloading at a rate of 1 MPa kyr^{-1} averaged over one eruption cycle. Zones are numbered and discussed in the text.

Eruption period is more sensitive to unloading than loading except when mass injection dominates (Zone 1) (Figure 3.5). This is not fully explained by the nonlinearity of the pressure-dependent melt solubility, which produces <3% asymmetry in gas exsolved under unloading and gas dissolved under loading. This

asymmetry is enhanced by the interaction between viscous relaxation and volatile exsolution. Magma pressurization from second boiling enhances viscous relaxation; in our simulations the chamber radius increases up to 20% faster in the unloading cases than the loading cases for loading rates of 0.1 MPa kyr^{-1} and up to 80% faster for loading rates of 1 MPa kyr^{-1} (Figure 3.5). The release of magma overpressure through viscous relaxation causes more volatile exsolution. Thus, there is a positive feedback between viscous relaxation and volatile exsolution. Although a growing magma chamber can slow exsolution driven by crystallization, this effect is secondary.

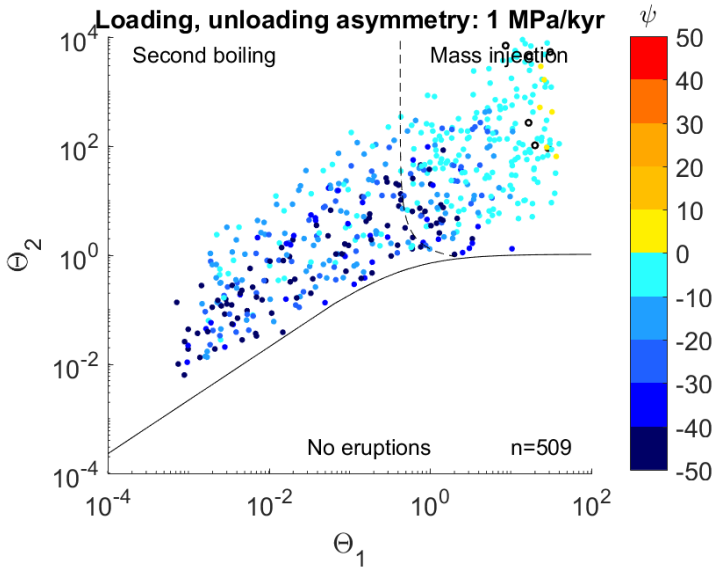

Figure 3.5. Asymmetrical response of eruption period to loading and unloading at a rate of 1 MPa kyr^{-1}. As a measure of this asymmetry, we define $\psi = 100\ \frac{\tau_{load}-\tau_0}{\tau_0-\tau_{unload}} - 1$. Cool colors designate cases for which the fractional change in eruption period is greater for unloading than loading. Warm colors designate cases for which the fractional change in eruption period is greater for loading than unloading. Dots are circled if ψ = 0, that is, if the response is symmetrical within model precision.

3.4 Discussion

In this study we estimated the eruptive response to deglaciation based on two mechanisms, a change in fracture pressure and a change in the rate of magma pressurization. Our simulations indicate that the minimum sensitivity is a function of the lithostatic pressure change between eruptions. However, the eruptive response to deglaciation for magma chambers in a low viscosity crust and significant dissolved water in the melt is influenced by the interaction between volatile exsolution and viscous relaxation. We find that deglaciation may affect volatile exsolution rates both by the direct decompression of magma and by enhanced viscous relaxation which relieves magma overpressure. By decreasing the water content of magma in the chamber, deglaciation may also lead to less exsolution during magma ascent and higher magma viscosities (Friedman et al., 1963). Both factors can affect eruptive style and dyke propagation dynamics.

Our model results indicate a minor change in eruption frequency as a direct result of present-day ice thinning. Typical glacier thinning rates are sufficient to produce on the order of 0.1 MPa kyr^{-1} change in lithostatic stress; in our model this generally produces <10% change in eruption period for eruption periods less than 10 kyr. This change would be difficult to detect and attribute to ice thinning, given many other processes that influence eruption timing and may be unimportant for hazard prediction. However, glaciers may cause much larger changes in stress through edifice collapse by weakening crustal rocks. These larger stress changes can have a greater influence on eruption frequency.

Eruption frequency changes may be enhanced over glacial cycles if glacial loading suppresses eruptions (rather than merely delay them) and unloading reactivates magma chambers that were uneruptible. In our simulations the shift in the threshold conditions for eruptions is very small for load rates of 0.1 MPa kyr^{-1}, suggesting that this effect is relatively unimportant at low loading rates. However, at higher loading rates of 1 MPa kyr^{-1}, magma chambers under a wider range of conditions transitioned from uneruptible to eruptible and vice versa. This raises the possibility that there are conditions for which eruption cycles could become phase locked with either eccentricity (100 kyr) or obliquity (40 kyr) cycles. Futhermore, crustal residence times may also differ between glaciation and deglaciation phases, affecting magma composition. This is compatible with Rawson et al.'s (2016) findings that during and immediately following glaciation erupted magma was more evolved and later in the deglaciation phase erupted magma was less evolved.

The low viscosity cases that undergo this transition from uneruptible to eruptible tend to have low magma overpressures. When crustal viscosity is very low, magma chamber pressure remains close to the lithostatic pressure and a dyke is initiated only when the fracture pressure approaches the lithostatic pressure. The small magma overpressure present at the dyke initiation may not be sufficient to propagate the dyke to the surface. Thus, under these conditions sill or dyke emplacement may be more likely. Thus, the change in frequency of dyke initiation simulated in this study may not cause a change in eruption frequency. Rapid

unloading, on the other hand, may sustain sufficient overpressure to drive dyke propagation to the surface and cause eruptions.

Our finding that magma chambers in low viscosity crust are particularly sensitive to deglaciation may be relevant to studies in West Antarctica, which likely has a warm upper crust due to mantle plume-enhanced conductive heat flux and a history of magmatic, advective heat flux (e.g., Flóvenz & Saemundsson, 1993; Hole & LeMasurier, 1994). Long-lived volcanic arcs such as the Andean Volcanic Belt (e.g., Dungan et al., 2001) may also be sensitive to deglaciation due to lower crustal viscosities. However, low viscosity crusts can also result in more infrequent eruptions, which may make a deglacial change in eruption frequency hard to detect.

3.5 Conclusions

We assessed a proposed mechanism for the magmatic response to deglaciation, decreased fracture pressure and magma pressure, with respect to the strength of climate-volcanism coupling. Simulations with a thermomechanical magma chamber model indicate that this mechanism can produce a magmatic response to ice retreat, increasing eruption frequency, eruptive flux, viscous relaxation, and exsolution rates (Figure 3.9). We found that this mechanism generally produces less than a 10% change in eruption frequency at present-day ice retreat rates. However, this mechanism may have played a larger role during the last deglaciation, which was characterized by more rapid ice retreat. In our simulations, magma chamber dynamics during deglaciation, particularly the interaction between

volatile exsolution and viscous relaxation, contribute as much to the change in eruption timing as the direct effect of glaciation on the fracture pressure.

Our analysis of the relationship between magma chamber properties and their sensitivity to ice thinning can focus future regional investigations of hazards on ice-covered volcanoes. We identify conditions under which volatile exsolution is dynamically important, which is for all but high recharge conditions. We show that magma chambers in a low viscosity crust are particularly sensitive to deglaciation. In a natural magma chamber, there are many complexities and variations in initial conditions that might make a magma chamber more sensitive or less sensitive to deglaciation than our model can capture. The dynamics of dyke propagation are also not included in the present analysis. Although any local determination of eruption likelihood will require careful examination of these conditions, this modeling lays the foundation for these assessments by combining non-linear magma chamber dynamics and load-induced stress changes.

Although our focus in this study is the effect of glacial loads on volcanoes, our methods and results may be applicable to magma chambers experiencing non-glacial changes in crustal stress. Our finding that glacial loading can suppress eruptions is compatible with Pinel and Jaupart's (2000) proposal that edifice construction can suppress eruptions. Erosion rates can induce unloading rates of the same order considered in this study, given that upper crustal rocks and sediments are around 3 times denser than ice (Hallet et al., 1996; Koppes & Montgomery, 2009; Sternai et al., 2016). Declining water levels in nearby water bodies such as glacial

lake outburst floods may also induce crustal unloading (Sternai et al., 2017). Edifice collapse and glacial lake outburst floods may induce more rapid pressure changes than explored in this study (Pinel et al., 2010) and may be associated with a dynamic shift in eruption sensitivity. Although we do not explore the full range of natural surface load changes, this study advances our understanding of the key processes that control magma chamber response to surface loading across a wide range of magma chamber parameters.

Chapter 4 Ocean stratification and low melt rates at the Ross Ice Shelf grounding zone

Abstract

Ocean-driven melting of ice shelves is a primary mechanism for ice loss from Antarctica. However, due to the difficulty in accessing the sub-ice-shelf ocean cavity, the relationship between ice-shelf melting and ocean conditions is poorly understood, particularly near the grounding zone, where the ice transitions from grounded to floating. We present the first borehole oceanographic observations from the grounding zone of the Ross Ice Shelf, Antarctica's largest ice shelf by area. Contrary to predictions that tidal currents near grounding zones mix the water column, we found that Ross Ice Shelf waters were vertically stratified. Current velocities at mid-depth in the ocean cavity did not change significantly over measurement periods at two different parts of the tidal cycle. The observed stratification resulted in low melt rates, inferred from phase-sensitive radar observations. These melt rates were generally <10 cm yr^{-1}, which is lower than average for the Ross Ice Shelf (~20 cm yr^{-1}). Melt rates may be higher at portions of the grounding zone that experience higher subglacial discharge or stronger tidal mixing. Stratification in the cavity at the borehole site was prone to double-diffusive convection as a result of ice-shelf melting, with inverse stability ratios from 9 to 11. Since double-diffusive convection influences vertical heat and salt fluxes differently than shear-driven turbulence, this process may affect ice-shelf melting and merits further consideration in ocean models of sub-ice-shelf circulation.

4.1 Introduction

Antarctic ice shelves presently lose over half of their mass by basal melting (Rignot et al., 2013). Although basal melting of floating ice has a small direct effect on sea level (Shepherd et al., 2010), the indirect effects of ice-shelf thinning can be significant by increasing the flux of grounded ice into the ocean (Pritchard et al., 2012), potentially driving grounding zone retreat (Schoof, 2007). Thus, ice-shelf melting is a key dynamic mechanism connecting ocean warming to future ice-sheet collapse and consequent sea-level rise (Pritchard et al., 2012). Understanding the relationship between ice-shelf melting and ocean conditions is essential for accurate projections of sea-level rise.

Ice-shelf basal melting is driven by the flux of heat from sub-ice-shelf cavity water masses to the ice-shelf base. On broad spatial scales, basal melt rates increase with the thermal driving, the difference between water temperature and the local ice freezing point. For example, high thermal driving (4 °C) in the Amundsen Sea drives high basal melt rates averaging ~15 m yr^{-1} (Rignot et al., 2013; Stanton et al., 2013), and low thermal driving (0.5 °C) in the Ross Sea drives basal melt rates averaging ~0.1 m yr^{-1} (Moholdt et al., 2014). However, several factors generate spatial variability in basal melt rates within regions under similar thermal driving. Stratification typically exists below ice shelves between colder, buoyant meltwater-rich water and warmer, denser continental shelf water (e.g., Jacobs et al., 1979). Meltwater from subglacial outflow or basal melting can generate a buoyant plume that entrains warmer seawater from below, driving high basal melt rates (e.g., Gladish

et al., 2012; Jenkins, 2011). The effect of subglacial water outflow on melt rates tends to be greatest in magnitude and most localized (i.e., channelized) near the grounding zone (Dutrieux et al., 2013; Marsh et al., 2016).

Tidal variations in current velocity can also elevate turbulent heat fluxes to the ice shelf; these variations can be up to several times the mean current velocity below ice shelves (e.g., Nicholls et al., 1997). Numerical modeling indicates that tides enhance ice-shelf melting and its spatial variability (Makinson et al., 2011; Mueller et al., 2012, 2018; Padman et al., 2018). Where the ocean cavity is narrow, as it is near the grounding zone, current shear at water mass boundaries enhanced by tides could be sufficient to destroy stratification (P. R. Holland, 2008; MacAyeal, 1984). A tidally-mixed zone prevents the formation of a meltwater plume close to the grounding zone, where subglacial discharge occurs (P. R. Holland, 2008). Thus, tidally-mixed zones may reduce the distance over which the plume accelerates, and consequently reduce the plume's velocity, turbulent heat fluxes to the ice-shelf base and ice-shelf melt rates. Tidally-mixed zones may also help buffer ice-shelf melt rates near the grounding zone from changes in sub-ice-shelf circulation (P. R. Holland, 2008; MacAyeal, 1984), of which the most concerning for ice-shelf stability has been the incursion of warm Circumpolar Deep Water (e.g., Cook et al., 2016).

The loss of grounded ice is particularly sensitive to ice-shelf melting near the grounding zone compared with ice-shelf melting elsewhere (Gagliardini et al., 2010; Reese et al., 2018; Walker et al., 2008). Despite this relationship, the thin sub-ice-shelf ocean cavity near grounding zones has rarely been observed, due to the

logistical challenge of accessing these areas that tend to be far from the open ocean and buried beneath thick ice. Here we report on direct borehole observations below the largest Antarctic ice shelf, the Ross Ice Shelf (RIS), near the Whillans Ice Stream grounding zone. To our knowledge, this is the first oceanographic study near the RIS grounding zone; there has been one oceanographic study near the grounding zone of an Antarctic ice shelf at the Langhovde Glacier (Sugiyama et al., 2014). Past direct observations of the ocean cavity below the RIS have been limited to three borehole locations, one 200 km downstream of the grounding zone (Jacobs et al., 1979) and two within 20 km of the ice shelf front (Arzeno et al., 2014) (Figure 4.1a). The new borehole lies within the flexure zone, where the ice transitions from fully grounded to fully floating, as determined from TerraSAR-X data collected in 2012 (Figure 4.1b) (Marsh et al., 2016). We combine oceanographic observations with contemporaneous coherent radar measurements of basal melting to evaluate the relationship between ocean water properties and melt rates in a grounding zone setting and determine whether this setting is tidally mixed.

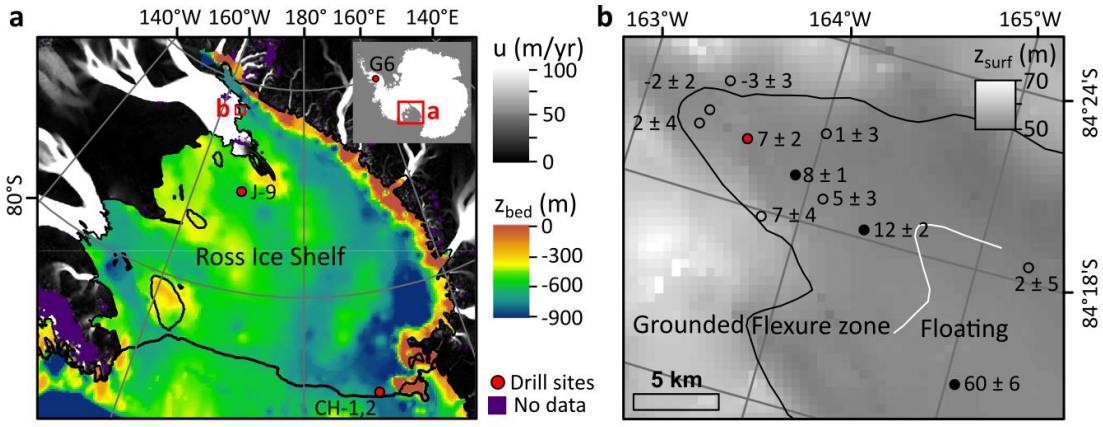

Figure 4.1. Measurement sites. **a.** Ross Sea region of Antarctica (inset). Bathymetry (z_{bed}) is shown for the Ross Sea (Fretwell et al., 2013). Grounded ice velocity (u)

(Rignot et al., 2011) is shown by grey shading. The RIS is outlined in black (Rignot et al., 2011). Red circles indicate locations of oceanographic observations below the RIS (CH-1,2: Arzeno et al., 2014; J-9: Jacobs et al., 1979) and the George VI Ice Shelf (G6: Kimura et al., 2015). **b.** Locations of radar measurements (black circles) with mean melt rate ± 1 S.D. (cm yr^{-1}) on an ice surface elevation model ($z_{surface}$) (DiMarzio, 2007). Empty circles indicate melt rates within 2 S.D. of 0 cm yr^{-1}. The borehole is highlighted in red. Inland and seaward limits of the flexure zone are shown with black and white lines, respectively (Marsh et al., 2016).

4.2 Methods

4.2.1 Oceanographic observations of the sub-ice shelf cavity

The Whillans Ice Stream Subglacial Access Research Drilling (WISSARD) field team accessed the sub-ice shelf cavity using a hot water drill (Rack et al., 2014; Tulaczyk et al., 2014), and deployed geophysical instruments into the cavity during January 7-19, 2015. To maintain access during borehole observations, the borehole was reamed once with hot water (Figure 4.2).

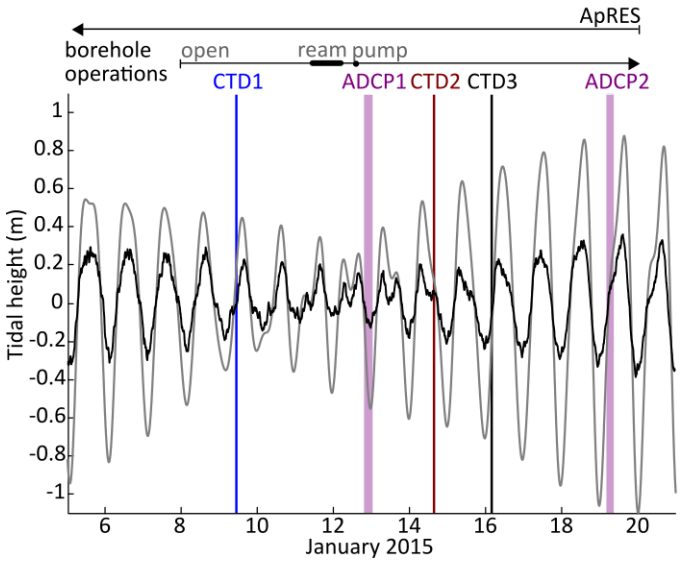

Figure 4.2. Timeline of observations. ApRES measurement period at the borehole starting on December 13, 2014 (top horizontal line). Operations began with borehole opening to the ocean (thin vertical line) and include reaming with hot water (thick horizontal line) and withdrawal of borehole water by pumping (starting at the black dot). Borehole instrument deployments (vertical lines) include three CTD casts and

two ADCP measurements. GPS height data at borehole (black) are compared with the CATS2008a tide model (grey) (after Padman et al., 2002).

Current velocity and direction in the cavity were measured using a Nortek Aquadopp 2 MHz Acoustic Doppler Current Profiler (ADCP). This instrument was deployed once at low tide and again at rising tide as determined by a tide model and GPS observations (Figure 4.2). The ADCP has instrumental accuracy of 1% of the current magnitude ± 0.5 cm s^{-1} and 2° in current orientation. Since current variability is not expected on very short timescales, the average standard deviation of velocity measurements over 10-minute intervals is taken to be an in situ estimate of instrumental noise, equal to 0.2 cm s^{-1}. Acoustic backscatter levels were weak due to low concentrations of suspended particulate matter, resulting in limited range and high noise when collecting vertical current profiles. To improve the signal-to-noise ratio, measurements were made at 1 Hz for 5-6 hours with the sensor stationed ~5 m below the ice shelf base near the middle of the water column. We only analyzed data collected when the ADCP was rotating less than 2° s^{-1} and the current orientation was changing less than 2° s^{-1} during intervals of at least 30 s.

A Sea-Bird Electronics 19plus V2 CTD profiler was used to measure conductivity (C), temperature (T) and depth (D; through pressure, P) at a frequency of 4 Hz with accuracies of 0.5 mS m^{-1}, 0.005 °C and 1 dbar, respectively. Raw data are available as Data Set S1. The profiler was lowered at a (median) rate of 14.8 cm/s for Cast 1, 4.1 cm/s for Cast 2, and 8.6 cm/s for Cast 3. The T and C profiles of Casts 1 and 3 were single-pole low-pass filtered at 2 s, and the profiles of Cast 2, which had more noise, were filtered at 4 s. We low-pass filtered all casts at 1 s in P and smooth

the descent rate with a window of 2 s. Thus, the vertical resolution of T and C after smoothing is 30 cm for Cast 1, 16 cm for Cast 2 and 17 cm for Cast 3.

We derived absolute salinity (S_A), conservative temperature (Θ) and potential density (ρ) referenced to 665 dbar using the CTD data and the Thermodynamic Equation of Seawater (IOC et al., 2010). The accuracy of these derived quantities is 6 x 10^{-3} g kg^{-1}, 0.005 °C, and 4 x 10^{-4} kg m^{-3}, and the resolution is 6 x 10^{-5} g kg^{-1}, 1 x 10^{-4} °C, and 1 x 10^{-4} kg m^{-3}, respectively. Profiles within the ocean cavity had higher noise levels than this, perhaps due to icing or particulates in the pumped C-T sensor. Higher noise levels were particularly evident in Cast 2 likely due to the very low descent speed of the sensor and small amplitude internal waves. The cavity top was identified by a sharp contrast in Θ and SA. The ice-shelf thickness is estimated to be 755 m from CTD-derived density profiles and laser-determined distance from ice-surface to the borehole water surface. The ice-shelf thickness is independently estimated to be 757 m by temperature sensors at 1 m intervals on a steel-reinforced cable of known length. Thickness of the sub-ice shelf cavity was determined by lowering the CTD instrument until it rested on the seafloor as determined by pressure maxima. Mixed layers within the observed stratification were defined by local gradients in filtered Θ that were less than the mean gradients over the 10-m-thick cavity for at least 0.5 m.

The uppermost water layer of Cast 1 was not analyzed because its salinity characteristics had not yet recovered from the perturbation of borehole opening. The temperature and salinity discontinuities at the ice base are small in Casts 2 and 3

because we pumped water out of the borehole at a low rate prior to and during these casts. At the time of Casts 2 and 3 water in the lower part of the borehole was at seawater salinity and had relaxed to the pressure- and salinity-dependent freezing point, which is the expected temperature at the ice shelf base when in thermodynamic equilibrium.

4.2.2 Ice shelf basal melt rates

We estimated ice-shelf basal melt rates at 11 locations in and around the grounding zone embayment using an Autonomous phase-sensitive Radio-Echo Sounding (ApRES) system following Brennan et al. (2013) and Marsh et al. (2016). At each site radar measurements were collected at weekly intervals over a period of 10-38 days with intermediate measurements used to validate mean melt rates over the entire period. Given that the ice shelf is ~755 m thick at the borehole, measurements represent basal melt rates over a 50-60 m diameter area.

We compute the heat and salt fluxes associated with basal melting from the ApRES-derived basal melt rate at the borehole. The heat flux required to explain the observed basal melt rate is

$$Q_{melt}^{T} = -\rho_i m' L_f \quad (4.1)$$

where ρ_i is the ice density taken to be 917 kg m^{-3}, m' is the melt rate, and L_f is the latent heat of fusion. There will be some conductive heat loss from the water at the ice shelf base; however, it will be small relative to the uncertainty in melt rates and is neglected here (following Jenkins et al., 2010). We assume that salt fluxes from the seafloor and into the ice are negligible. The salt flux induced by melting is

$$Q_{melt}^{S} = -\rho_i m' S_{io} \quad (4.2)$$

where S_{io} is the salinity at the ice-ocean interface, assuming the salinity of basal shelf ice is 0 g kg^{-1}. Q_{melt}^{S} was calculated using S_{io} equal to salinity values found at the base of the ice borehole. Although S_{io} is not well-constrained due to the presence of the borehole, uncertainty in Q_{melt}^{S} is dominated by uncertainty in m' (99% of error).

The primary tool for modelling ice-shelf basal melting and freezing in both ocean models (Dansereau et al., 2013; Gwyther et al., 2016) and coupled ice-sheet ocean models (Jordan et al., 2018) is the "three-equation model." The three equations express the pressure- and salinity-dependent freezing point of water, heat conservation, and salt conservation at the ice-ocean interface (D. M. Holland & Jenkins, 1999). The key parameters in this model are the exchange velocities (γ_T, γ_S) that describe fluxes of heat and salt across the viscous sub-layer. We applied our observations of water properties and melt rates to assess the accuracy of several parameterizations of exchange velocity with respect to ice-shelf melt rates derived using the three-equation model.

The three equations are as follows:

1. Freezing temperature condition

$$T_{io} = c_1 + c_2 S_{io} + c_3 P_{io} \quad (4.3)$$

where T_{io} and P_{io} are the temperature and pressure at the ice-ocean interface and c_1, c_2, c_3 are the coefficients that describe the freezing point of freshwater at atmospheric pressure (0.081 °C), the salinity dependence of the freezing point (-0.0568 °C (g kg^{-1})$^{-1}$), and the pressure dependence of the freezing point (-7.61 x 10^{-4}

°C m^{-1}), respectively (Jenkins, 2011). We set P_{io} from CTD data to the value at the cavity top. c_1, c_2 are chosen to fit the Thermodynamic Equation of Seawater at the pressure at the ice base over a plausible salinity range for the ice-ocean interface at this site (33.0 – 34.7 g kg^{-1}, see Section 4.1) (IOC et al., 2010).

2. Heat conservation

$$Q_{melt}^{T} = \rho_{UL} c_{pw} \gamma_T (T_{io} - T_{UL}) \quad (4.4)$$

where ρ_{UL} is the density of the upper layer (UL) water adjacent to the ice base, c_{pw} is the specific heat of water, γ_T is the heat exchange velocity, and T_{UL} is the temperature of UL water.

3. Salt conservation

$$Q_{melt}^{S} = \rho_{UL} \gamma_S (S_{io} - S_{UL}) \quad (4.5)$$

where γ_S is the salt exchange velocity, S_{UL} is the salinity of the UL water and, as before, heat conduction into the ice and salt diffusion into and out of the ice are neglected, as they are negligible compared to the melt rate term.

We use these three equations to define the equivalent heat and salt exchange velocities (γ_T, γ_S) as a function of the salinity at the ice-ocean interface (S_{io}). We then use these calculated exchange velocities to assess available parameterizations for exchange velocities. We test four parameterizations of exchange velocity: constant values (Hellmer & Olbers, 1989), a linear function of the friction velocity (Jenkins et al., 2010), and two other friction-velocity-dependent parameterizations (Kader & Yaglom, 1972; McPhee, 1983). The details of these parameterizations are summarized in D. M. Holland & Jenkins (1999). For the friction-velocity-dependent

parameterizations, we solve for the friction velocity that produces the observationally constrained exchange velocity. We then use a quadratic drag relation for friction velocity, u^*, to solve for the far-field velocity, u

$$u^* = c_d^{1/2} u \quad (4.6)$$

where c_d is the drag coefficient. There are large uncertainties in the drag coefficient; we use a range from 0.001 to 0.01 (a commonly-used value is 0.003; see Jenkins et al. (2010)). The far-field velocity yielded by the exchange velocity parameterizations and the observed melt rate is then compared to the observed velocity at mid-depth in the water column.

A two-equation approach presents an advantage over the 3-equation parameterization in that eliminates the unknown S_{io} (McPhee, 1992). In this approach, a single turbulent transfer coefficient, $\Gamma_{\{TS\}}$, represents the relative fluxes of heat and salt. Equation 4.3 is replaced with the freezing point evaluated at the far-field salinity

$$T_f = c_1 + c_2 S_{UL} + c_3 P_{io} \quad (4.7),$$

and Equation 4.4 is replaced with

$$Q_{melt}^T = \rho_{UL} c_{pw} u_* \Gamma_{\{TS\}} (T_f - T_{UL}) \quad (4.8).$$

We use these two equations to solve for the turbulent transfer coefficient $\Gamma_{\{TS\}}$ that fits our observations and compare it with previously-derived values.

The properties T_{UL}, S_{UL} and ρ_{UL} used as inputs to the parameterization should be derived from the interval closest to the ice-shelf base where the water is fully turbulent. Given that the UL is well-mixed and thus likely to be turbulent, we set

these values equal to their mean values within the UL. One could make the case that these input parameters should drawn from the shallowest depth at which the data fit a meltwater mixing line, which represents turbulent mixing between meltwater and seawater (further discussed in Section 4.3.1). If we use these properties as inputs to the parameterization, the predicted melt rates are about 20% higher than when the mean UL properties are used (Table 4.3).

4.2.3 Tidal forcing near the grounding zone

To quantify the local, non-hydrostatic, vertical motion of the ice shelf with tides, we collected continuous dual-frequency GPS data 284 m downstream of the borehole. The data were processed using Track v1.29 software (Chen, 1998) relative to a reference station (RAMG) located on bedrock 200 km away. We used final precise satellite orbits from the International GNSS Service to form the ionosphere-free linear combination of the two GPS frequencies. Antenna phase-center variations were modelled using igs08_1884.atx, and solid Earth tides were also modelled. Ocean tide loading displacements are small in this region and further cancel through differencing. Real-valued carrier-phase ambiguity parameters were fixed to integers where possible. Site coordinates and tropospheric zenith delays were estimated after applying a Kalman filter/smoother every measurement epoch (30s). Site coordinates and tropospheric zenith have process noise of 5 mm $(30s)^{-1/2}$ and 0.1 mm $(30s)^{-1/2}$, respectively. These temporal parameter constraints are loose enough not to over-smooth data or affect tidal frequencies while reducing noise. The short-term

repeatability of the resulting vertical coordinate time series suggests a precision of 1-2 cm.

4.3 Results

4.3.1 Observations of ice-shelf melting

Basal melt rates were generally low in the grounding zone embayment (Figure 4.1b). Melt rates at seven sites were within 2 S.D. of 0 m yr^{-1}, so neither melting nor freezing can be confidently identified. For the four remaining sites, melt rates tend to increase with distance from the grounding zone, with the highest rate (60 ± 6 cm yr^{-1}, as mean ± 1 S.D.) observed at the farthest site from the grounding zone (10 km from the upstream flexure limit). Strain rates measured at these sites over 1-5 weeks range from -0.14 to 0.15 mm $m^{-1}yr^{-1}$.

The melt rate at the borehole was 7 ± 2 cm yr^{-1} over the full ApRES measurement period. We focus on the melt rate during the same period as oceanographic observations of 5 ± 2 cm yr^{-1}. This is equivalent to a heat flux of 0.49 ± 0.20 W m^{-2} and a salt flux of 50 ± 20 µg s^{-1} m^{-2}. We do not detect statistically-significant variations in basal melt rate on weekly timescales at the borehole site at the 95% confidence level (Table 4.1).

Table 4.1. Weekly basal melt rates at the WGZ borehole (GZ04).

Start Time (UTC)	End Time (UTC)	Interval (days)	Melt (cm)	Melt rate (cm yr^{-1})	Vertical strain rates (mm m^{-1} yr^{-1})
12 Dec 2014 01:15	21 Dec 2014 03:30	8.09	0.19	8.6 ± 4.4	-0.01 ± 0.05
21 Dec 2014 03:30	30 Dec 2014 23:04	9.82	0.15	5.5 ± 2.7	0.15 ± 0.03
30 Dec 2014 23:04	05 Jan 2015 04:00	5.21	0.22	15.3 ± 6.1	0.04 ± 0.07
05 Jan 2015 04:00	20 Jan 2015 00:08	14.84	0.21	5.3 ± 2.3	-0.10 ± 0.03

Note: Basal melt rates and vertical strain rates expressed as mean ± 1 S.D.

4.3.2 Oceanographic observations

Three direct observations of the vertical structure of ocean temperature and conductivity were collected over seven days through the borehole. Cast 2 shows high frequency variability in in-situ temperature and conductivity due to lowering rates that are too slow to capture a snapshot of the T-S conditions. Cast 1 and 3 were lowered quickly enough to provide representative profiles. There is a period of temperature sensor error in Cast 3 (Figure 4.3), which may be due to ice particles passing through the pumped sensor system. As noted in Section 2.1, the uppermost 1m of Cast 1 is also not analyzed because it shows a perturbation from borehole opening.

These observations reveal stratification within the 10 m thick sub-ice-shelf ocean cavity (Figure 4.3). The observed thermohaline staircase was composed of three, 1-4 m thick mixed layers. We refer to the three mixed layers as Upper Layer (UL), Middle Layer (ML) and the Bottom Boundary Layer (BBL) as labeled in Figure 4.3. These layers were separated by 1-2 m thick interfaces defined by steep gradients in temperature (steeper than background gradients). The interface close to the base of the borehole is considered a transition layer, also characterized by steep temperature and salinity gradients. In contrast, the interface between ML and BBL does not show steep salinity gradients. In the last several meters of the water column, stratification becomes roughly isopycnal.

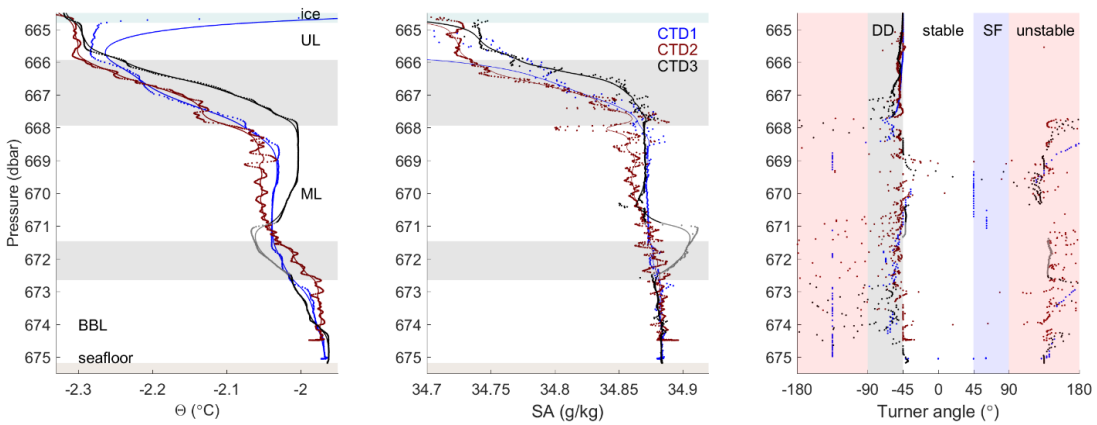

Figure 4.3. CTD observations. **a,b.** Unfiltered data (points) and filtered data (solid lines) for (a) conservative temperature (Θ), (b) absolute salinity (SA). Individual casts are numbered, corresponding to the timeline given in Figure 4.2. A segment of CTD3 (green) is affected by a temperature sensor malfunction. Mixed layers (no shading) and interfaces (grey shading) are identified based on whether the vertical temperature gradient was greater or less than the mean temperature gradient, respectively. **c.** Turner angle for filtered CTD data ($R_\rho^* = -\tan(Tu + 45°)^{-1}$) . Stratification regimes are shaded and labeled (DD = double-diffusive regime, stable regime, SF = salt fingering regime, unstable regime).

The maximum thermal driving, the difference between UL temperature and the freezing temperature, is 0.1 °C for a freezing temperature based on the UL salinity (Figure 4.4b). In contrast, thermal driving is 0.35-0.50 °C for HSSW temperatures at the ice-shelf front at depths greater than 500 m (Orsi & Wiederwohl, 2009) using the same UL freezing temperature.

This stratification persisted over seven days, and its properties were generally consistent between observations (Table 4.2). Even though the water properties of Cast 1 near the ice-ocean interface may have been disturbed by borehole operations, the properties below UL were consistent with Casts 2 and 3. There was some variability in ML characteristics on sub-weekly timescales, with a maximum increase in ML temperature of 0.04 °C over 36 hours (between Casts 2 and 3).

Table 4.2. Oceanographic conditions derived from CTD instrument.

	CTD Cast 2	CTD Cast 3
UL temperature [°C]	-2.305 ± 0.007	-2.296 ± 0.007
UL salinity [g kg^{-1}]	34.712 ± 0.021	34.730 ± 0.015
ML temperature [°C]	-2.050 ± 0.009	-2.011 ± 0.011
ML salinity [g kg^{-1}]	34.865 ± 0.008	34.870 ± 0.006
BBL temperature [°C]	-1.976 ± 0.006	-1.964 ± 0.005
BBL salinity [g kg^{-1}]	34.884 ± 0.006	34.883 ± 0.006
UL thickness [m]	1.2	0.7
UL-ML interface thickness [m]	2.6	2.5
ML thickness [m]	3.2	3.9
ML-BBL interface thickness [m]	1.2	2.5
BBL thickness [m]	1.8	0.9
$R_\rho{}^*$ of UL-ML interface [ND]	10.8 ± 1.7	8.8 ± 1.1
$R_\rho{}^*$ of ML-BL interface [ND]	4.4 ± 2.3	4.8 ± 3.2

Note: Temperature and salinity standard deviations are determined by the variance of the values in each cast after filtering was applied to remove noise. Inverse stability ratio (R_ρ^*) standard deviations are determined by Gaussian propagation of errors from temperature and salinity errors.

When the eddy diffusivities of heat and salt are identical (k_s/k_t = 1), the temperature and salinity characteristics will have the slope of the "meltwater mixing line" connecting source water temperature and salinity with meltwater properties. The slope of this line ($d\theta/dSA$) was originally defined by Gade (1979) and corrected by McDougall et al. (2014). We evaluate the hypothesis that heat and salt transport are fully turbulent using the meltwater mixing line fit to Cast 3 properties. The source waters for the meltwater mixing lines are chosen at 666 dbar, the greatest depth before a break in θ-SA slope away from the meltwater mixing line. The CTD data most closely fits the meltwater mixing line over a ~0.5 m interval within the UL-ML interface using basal ice temperature at the freezing point (a slope of 2.37 °C $(g/kg)^{-1}$, Figure 4.4b). The fit between data and the meltwater mixing line is reduced if colder basal ice temperatures are used. The UL water mass diverges from the meltwater

mixing line, at lower salinities and higher temperatures than the meltwater mixing line predicts. Two explanations for these characteristics are favoured transport of heat over salt ($k_s/k_t < 1$) and advection of UL. We return to the first hypothesis in sections 4.1 and 4.3.b but cannot address the second hypothesis as we do not have current profiles or lateral information about water properties.

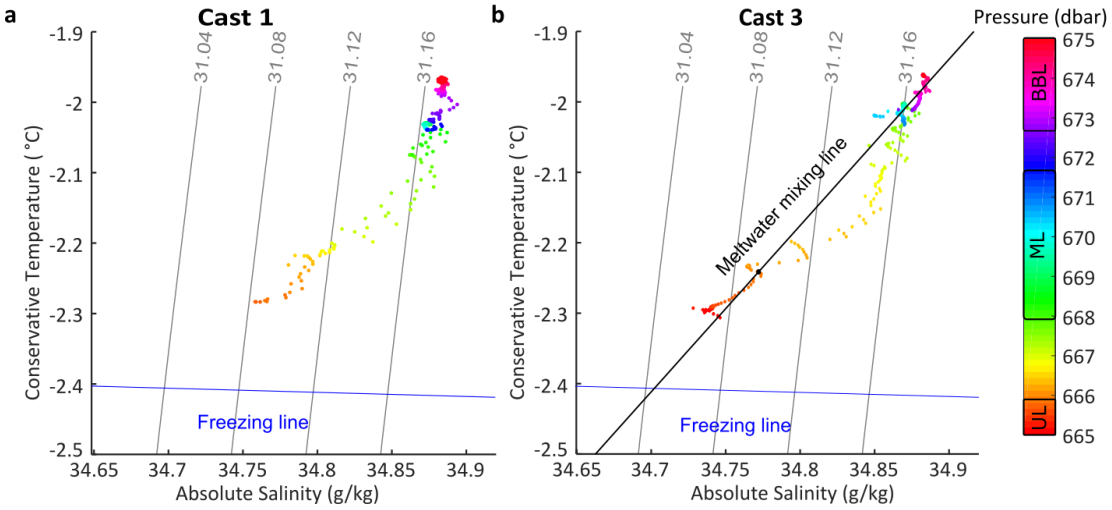

Figure 4.4. Temperature-salinity plots for Cast 1 (a) and Cast 3 (b). Data in the UL from Cast 1 are omitted due to contamination with borehole water. Unfiltered CTD data is colored by the pressure at which it was collected. Lines of constant density are plotted in grey. Freezing line (blue) is plotted for a constant pressure of 665 dbar. **b**. The meltwater mixing lines is plotted in black, and a black filled point along that line denotes the source water chosen.

Measured ML currents at ~5 m below the ice shelf were 1.5 ± 0.2 cm s^{-1} (mean ± 1 S.D.) oriented 175 ± 95°N (mean ± 1 S.D.) during ADCP Deployment 1 (falling tide) and 1.3 ± 0.3 cm s^{-1} oriented 165 ± 25°N during ADCP Deployment 2 (rising tide). Apparent current orientation fluctuates in ADCP Deployment 1, as a result of sensor rotation in the water column. This sensor motion may induce fluid motion near the sensor that biases measurements of current velocity and orientation.

Only short intervals of data from ADCP Deployment 1 passed our criteria for reliable data of both low sensor rotation rates and low current rotation rates. Thus, current orientation over this period is not well-constrained. Current speeds were not significantly different at the two observed parts of the tidal cycle (Figure 4.5a). The tidal velocity variation between these two intervals is within 1 S.D. of 0 cm s^{-1} ($\overline{u}(\mathrm{ADCP1}) - \overline{u}(\mathrm{ADCP2}) = 0.2 \pm 0.4$ cm s^{-1}), and has an amplitude less than the mean current. Thus, at mid-depth in the sub-ice-shelf cavity there is a weak mean current oriented toward the grounding zone, with a weak or absent tidally-varying component.

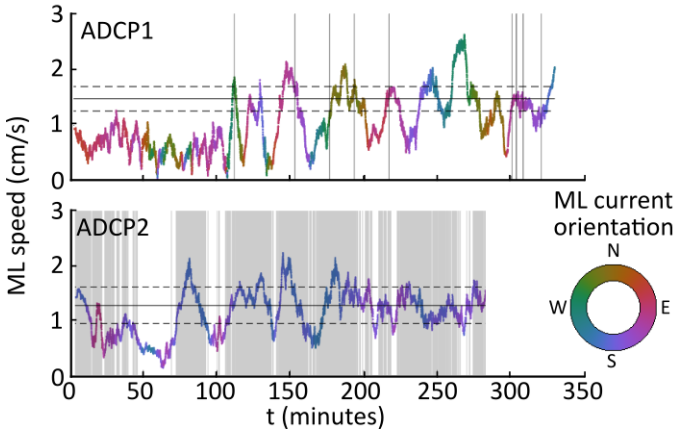

Figure 4.5. Current speed and orientation (color) at 5 m depth in the sub-ice shelf ocean cavity within the Middle Layer (ML). Mean current speed ± 1 S.D. are indicated (horizontal lines). Data analysis windows are shaded; see Figure 4.2 for time period of observations.

4.3.3 Tidal motion of the ice shelf

The Ross Sea ocean tide is mainly diurnal, and variations in ice-shelf height at the borehole were about 40% of the predicted diurnal variations in the freely-floating ice shelf according to the CATS 2008a tidal model (after (Padman et al., 2002).

During ADCP Deployment 1, tides were falling to low tide during a neap tide with a freely-floating tidal range of 0.77 m and a local ice-shelf height change of 0.35 m. During ADCP Deployment 2, tides were rising during a spring tide with a freely-floating tidal range of 1.8 m and a local ice-shelf elevation change of 0.79 m. This was close to the maximum diurnal ice-shelf height change observed in January 2015 at the borehole site of 0.81 m. These reductions in vertical ice-shelf motion are consistent with the location of the borehole within the flexure zone near the grounding zone.

4.4 Discussion

4.4.1 Ice-shelf melting: effectiveness of parameterizations

Using observationally constrained ocean conditions we assess the consistency of observed melt rates and parameterizations used in two- and three-equation models. We directly assess the accuracy of the 3-equation, velocity-independent parameterization of Hellmer & Olbers (1989), which overestimates melt rates at this site by an order of magnitude (76 cm yr^{-1}). Other 3-equation parameterizations rely on a far-field velocity to estimate the friction velocity. Our current velocity measurement is located 5 m from the ice base and below a significant stratification layer, and so may not capture the appropriate far-field velocity for determining the friction velocity. These 3-equation, velocity-dependent parameterizations (Jenkins et al., 2010; Kader & Yaglom, 1972; McPhee, 1983) are consistent with the observed melt rates and drag coefficients of 0.001-0.01 for far-field velocities of 0.2-0.7 cm s^{-1}, 0.2-0.5 cm s^{-1}, and 1-3 cm s^{-1}, respectively (Table 4.3). These parameterizations suggest a

slowly flowing UL. This is consistent with the low measured ice-shelf basal slopes (not significantly different from flat) in this grounding zone embayment (Horgan et al., 2013), which generate little buoyant acceleration.

The low melt rates also indicate a low turbulent transfer coefficient Γ_{TS} in the two-equation model (Equations 4.6 and 4.7). We report $c_d^{1/2}\Gamma_{TS}$, called the Stanton number, using a far-field velocity of 1 cm s^{-1} (Table 4.3). This Stanton number estimate is 2 orders of magnitude lower than the Stanton number for sub-sea-ice turbulence (McPhee et al., 1999) and 1 order of magnitude lower than the previously mentioned sub-ice-shelf setting (Jenkins et al., 2010). Both a low Stanton number and the 3-equation, velocity-dependent parameterization solutions are only consistent with low melt rates when there is a double-diffusive effect that favors heat fluxes over salt fluxes ($k_s/k_t < 1$) (Figure 4.6).

Table 4.3. Flux parameterizations for observed conditions at the WGZ borehole.

	Inferred from observed melt rate	*2-equation parameterizations*		*3-equation parameterizations*			
		MP99	J10	HO	KY (u_*)	MP (u_*)	J10 (u_*)
Heat flux [W m^{-2}]	0.49 ± 0.20	--	--	7.3	2.3	0.37	1.7
Salt flux [µg s^{-1} m^{-2}]	56 ± 22	--	--	723	230	37	170
Stanton number $c_d^{1/2}\Gamma_{TS}$ x 10^{-4}	0.87 ± 0.44	50-60	5.9	--	--	--	--
Inferred IO salinity [g kg^{-1}]	--	--	--	33.3	34.1	33.4	34.0

Melt rate [cm yr^{-1}], UL inputs (mixing line inputs)	5 ± 2	--	--	66 (80)	21 (26)	3.4 (3.9)	15 (18)
Inferred friction velocity [mm s^{-1}]	--	--	--	--	0.16	1.0	0.23
Inferred drag coef. for u = 1 cm s^{-1} [10^{-3}]	--	--	--	--	0.2	7	0.3
Inferred velocity for c_d = 0.001 - 0.01 [cm s^{-1}]	--	--	--	--	0.16 – 0.51	1.0 – 3.2	0.23 – 0.72

Note: The exchange velocities associated with the melt rate observation use the observed ice-ocean salinity range. Fluxes are defined as positive upward. Exchange velocity parameterizations: HO = Hellmer and Olbers (1989), KY = Kader and Yaglom (1972), MP = McPhee (1983), J10 = Jenkins et al. (2010).

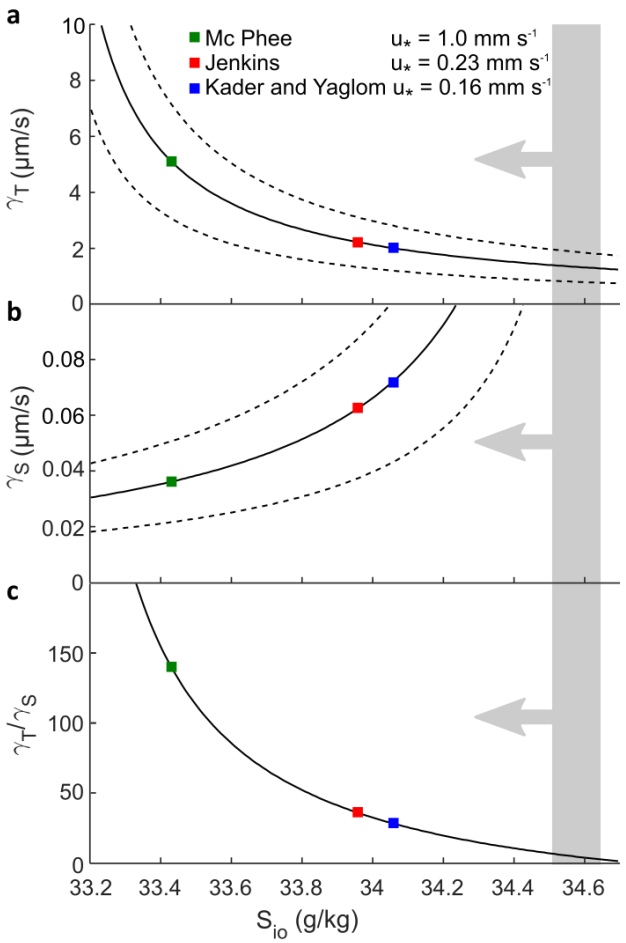

Figure 4.6. Solutions to the 3-equation formulation for the observed melt rate at the borehole. Solutions corresponding to the mean melt rate fall along the black solid line; dotted lines bracket 2 S.D. of the melt rate. Sensitivity of (a) heat exchange velocity (γ_T) and (b) salt exchange velocity (γ_S) and (c) the ratio of heat exchange velocity to salt exchange velocity (γ_T/γ_S) to the salinity at the ice-ocean interface (S_{io}). The grey shaded interval spans salinities observed at the base of the ice borehole, taken to be upper bounds on S_{io}. Colored squares correspond to parameterized exchange velocities at the friction velocity required to reproduce the mean melt rate.

4.4.2 Absence of a tidally-mixed zone

Although a tidally-mixed zone has been postulated to develop near some ice-shelf grounding zones, stratification is observed 3 km from the Whillans Ice Stream grounding zone. Tidally-mixed zones are expected to freshen the inflowing water

mass by mixing with the meltwater-influenced ISW. Thus, it is implausible that a tidally-mixed zone is present immediately seaward of this site given the highly saline water present. ML and BBL have salinities of 34.87 ± 0.01 g kg^{-1} and 34.88 ± 0.01 g kg^{-1}, respectively, which is more saline than 95% of HSSW by volume in the open Ross Sea (Orsi & Wiederwohl, 2009). While ML and BBL may be sourced from highly saline HSSW which is freshened by a tidally-mixed zone, a more plausible scenario is that ML and BBL are part of a continuous, inflowing HSSW, uninterrupted by full-water-column tidal mixing seaward of the borehole (Figure 4.7).

The observed oceanographic conditions and melt rates are consistent with a proposed threshold between stratification and full-water-column tidal mixing (MacAyeal, 1984). The threshold has been defined by melt rate at which turbulent kinetic energy dissipation is balanced by the potential energy needed to mix the freshwater supplied by ice-shelf melting through the entire water column (MacAyeal, 1984):

$$m_c = \frac{2\alpha c_d \langle |\boldsymbol{u}|^3 \rangle}{\beta_S g S h} \quad (4.9)$$

where α is the percent of dissipated energy that goes into eroding stratification (assumed to be $\mathcal{O}$(1%) Fearnhead, 1975; Schumacher et al., 1979), $\langle |\boldsymbol{u}| \rangle$ is time-averaged horizontal speed of the flow, β_S is the saline contraction coefficient (8 x 10^{-4} g kg^{-1}), S is the water's salinity (assumed uniform), and h is the ocean cavity height. The critical melt rate, according to this formulation, was 1-4 mm yr^{-1} using the observed ML current speed (mean – 1 S.D. and mean + 1 S.D., respectively, from ADCP2), water column height, ML salinity, α = 1%, c_d = 0.003. While this critical

melt rate estimate falls well below the observed melt rate of 5 ± 2 cm yr^{-1}, as expected for a stratified setting, we are unable to rigorously evaluate this formulation given uncertainties in c_d, $\boldsymbol{u}$, and α. This critical melt rate estimate is revised downward from MacAyeal's (1984) estimate of ~1 m yr^{-1} for the Whillans Ice Stream grounding zone region, which likely resulted from overestimated current speeds as well as limited knowledge of ocean cavity geometry.

This analysis concurs with Holland (2008) that tidally-mixed zones do not form below the RIS in the presence of weak currents (~1 cm s^{-1}). The absence of significant tidal variations in current velocity contrasts with sub-ice-shelf settings that have tidal variations in current velocity that exceed the mean current (Nicholls et al., 1997). This is consistent with ocean circulation models indicating that tidal currents may be spatially variable below ice shelves (Mueller et al., 2018).

The absence of a tidally-mixed zone allows a buoyant upper layer or meltwater plume to develop at the grounding zone rather than 10s of km seaward outside the tidally-mixed zone. This difference in plume extent may result in a difference in plume velocity by controlling the distance over which the plume accelerates along a sloped ice-shelf base. Tidally-mixed zones may also alter plume buoyancy by controlling the distribution of meltwater. The absence of a tidally-mixed zone also allows dense seawater to reach the grounding zone without significant mixing with meltwater. Consequently, changes in the temperature and salinity characteristics of that seawater may affect melt rates near the grounding zone more strongly in the absence of a tidally-mixed zone. The extent of tidally-mixed zones

may be dynamically important below Antarctic ice shelves threatened by the intrusion of warm ocean water, by determining whether warm water masses can cause high melt rates at the grounding zone.

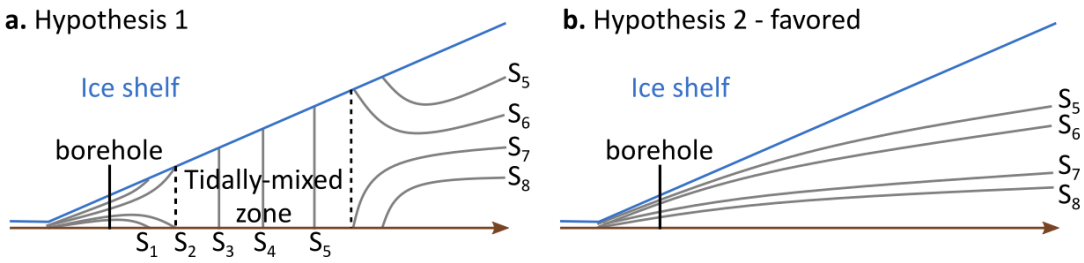

Figure 4.7. Schematic of the sub-ice shelf cavity (a) with a tidally-mixed zone and (b) without a tidally-mixed zone. Grey lines represent schematic isopycnals. Salinities increase as subscripts increase. Dashed black lines mark the limits of the tidally-mixed zone, after Holland (2008).

4.4.3 Contributions to vertical mixing

4.4.3.a. Shear-driven mixing

Turbulent eddies produced by boundary shear are likely to play a role in generating the observed three-layer structure. Temperature and salinity gradients tend to be homogenized within the boundary layers UL and BBL through these eddies (e.g., Armi & Millard, 1976). The relative thicknesses of UL and the BBL are consistent with observationally-constrained scaling relationships for boundary layers. In a neutrally stratified water column with no buoyancy forcing, boundary layer thickness h is estimated to be $0.7u_*/f$, where f is the Coriolis parameter and u_* is the friction velocity (McWilliams & Huckle, 2006). For u_* determined by a quadratic drag law with c_D= 0.003 and a mean velocity of 1 cm s^{-1}, the neutral boundary layer is 3 m thick, consistent with the scale of the BBL.

The buoyancy flux provided by ice melting is expected to reduce the scale of eddies and thus reduce the scale of the ice-ocean boundary layer relative to a neutrally stratified boundary layer (McPhee, 1981). According to the analytic similarity theory extended by McPhee (1981) to the ice-ocean boundary layer, the boundary layer thickness scales with a stability parameter η_*: $h = c\eta_* u_*/f$, where c is about 0.5 and $\eta_* < 1$ (McPhee, 1981). For the buoyancy flux given by the observed melt rate (5 cm yr^{-1}, $\eta_* = 0.4$), the predicted ice-ocean boundary layer thickness is 1 m, similar to the observed UL. The details of this theory may not be entirely appropriate at the borehole site, where boundary layers were significantly thinner than the atmospheric and oceanic boundary layers for which the theory was developed. Nonetheless, the fact that UL is thinner than BBL is consistent with the hypothesis that boundary shear contributes to vertical mixing at the borehole.

Similar 3-layer stratification was observed near the grounding zone of Langhovde Glacier. Two boreholes there revealed that horizontal velocities of 2-3 cm s^{-1} at both sites generated ~5 m thick boundary layers in one 24 m thick ocean cavity setting and fully mixed waters in a 10 m thick ocean cavity setting (Sugiyama et al., 2014). Although the ocean cavity studied here is thinner, velocities of ~1 cm s^{-1} may be fast enough to generate well-mixed boundary layers while being slow enough to permit stratification.

Given the low melt rates at this site, shear-driven mixing is not strong in the UL. This may change during periods of subglacial water discharge (Jenkins, 2011). The thin (1 m) UL and its high salinity indicate that high subglacial water discharge

did not occur at the time of our observations. Subglacial Lake Whillans may episodically drain to the apex of this grounding zone embayment (Carter & Fricker, 2012), but a lake drainage had just occurred prior to our observations (Siegfried et al., 2016). The low melt rates at the borehole contrast with high melt rates (>10 m yr^{-1}) at nearby sites where high subglacial water discharge was inferred (Marsh et al., 2016).

4.4.3.b. Double-diffusive convection

Current forcing in this setting is low, both in the ML and likely also in the UL based on the low observed melt rates. This raises the possibility that double-diffusive convection contributes to vertical mixing. Ice-shelf melting can create the conditions for double diffusion by generating both a stable salinity gradient (by releasing freshwater) and an unstable temperature gradient (by extracting latent heat for melting). This unstable temperature gradient is a source of gravitational potential energy that can be released through double-diffusive convection when thermal diffusion produces instabilities at the edges of salinity interfaces (Radko, 2013). Turner angles, shown in Figure 4.3, indicate that the observed stratification is prone to double-diffusive convection. The inverse stability ratio, R_ρ^*, a related measure of double diffusion, indicates that stratification is near the stable limit of the double-diffusive regime.

$$R_\rho^* = \frac{\beta_S \Delta S}{\beta_T \Delta T} \quad (1)$$

where β_T, β_S are the thermal expansion and saline contraction coefficients, which are 4 x 10^{-5} °C^{-1} and 8 x 10^{-4} g/kg^{-1} in this setting (IOC et al., 2010) and ΔS, ΔT

are salinity and temperature differences between layers. Although double-diffusive staircases can persist in the lab in the absence of shear up to $R_\rho^* = 55$ (Newell, 1984), canonically, stratification is considered prone to double-diffusive convection when R_ρ^* falls between 1 and 10 (Turner, 1965). R_ρ^* at this site is 9-11 between UL and ML and 4-5 between ML and BBL.

Double-diffusive convection can produce well-mixed layers separated by interfaces with steep gradients in temperature and salinity, a stratification structure called a double-diffusive staircase. Double-diffusive staircases have been observed in the Arctic Ocean, driven by freshwater flux and cooling at the surface (Sirevaag & Fer, 2012); in lakes, driven by high geothermal heat flux at lake bottom (Sommer et al., 2013); and in one case below an ice shelf, driven by ice-shelf melting (Kimura et al., 2015). The observed stratification differs from typical double-diffusive staircases in having large temperature and salinity steps between mixed layers and thicker interfaces. (Padman & Dillon, 1987, 1988; Sirevaag & Fer, 2012; Sommer et al., 2013; M.-L. Timmermans et al., 2008). The absence of a well-developed double-diffusive staircase may be related to high R_ρ^* values and large temperature and salinity gradients, which are associated with thicker interfaces (Marmorino & Caldwell, 1976; Newell, 1984; Sommer et al., 2013), or shear-driven mixing (Guthrie et al., 2017).

Shear-driven mixing may dominate heat and salt fluxes over double-diffusive convection at high R_ρ^* values (Crapper, 1976). Melt rates of 60 cm yr^{-1} observed 10 km from the grounding zone suggest that further up-shelf from the grounding line turbulent fluxes dominate over molecular double-diffusion, indicating a limited

double-diffusive zone. Although our analysis indicates that stratification at the Whillans Ice Stream grounding zone is marginally double-diffusive, this is due in part to the high salinity of the inflowing ML. Along other portions of the grounding zone that receive less salty HSSW or Low Salinity Shelf Water (Orsi & Wiederwohl, 2009), stability ratios may be lower and double-diffusive convection may be an important contribution to vertical mixing.

Where double-diffusive convection contributes to vertical mixing below ice shelves, it can have several important consequences for ice-shelf melting. Double-diffusive convection may play a significant role in plume evolution, as it fluxes buoyancy up vertical buoyancy gradients, in contrast to shear-driven turbulence, which transports buoyancy down-gradient (Radko, 2013). Double-diffusive convection favors vertical heat transport over salt transport ($k_s/k_t < 1$). In doing so, it may result in fresher ice-ocean boundary layers with lower thermal driving than may be present in shear-dominated regimes. Furthermore, double-diffusive fluxes are highly sensitive to the stability of stratification. Laboratory experiments on double-diffusive staircases (Flanagan et al., 2013; Guo et al., 2018; Dan E. Kelley, 1990; Marmorino & Caldwell, 1976; Turner, 1965) predict a power-law or exponential increase in heat fluxes as stability ratios decrease. Ongoing freshening and warming of HSSW (Jacobs & Giulivi, 2010) may decrease the stability of stratification at the RIS grounding zone and increase double-diffusive heat fluxes. The equilibrium response to such a perturbation is unknown, as it requires predictions of circulation patterns, the double-diffusive response, and ice-shelf melting. Predicting the

sensitivity of ice-shelf melting to future ocean conditions may require a more thorough understanding of double-diffusive dynamics in this regime.

4.5 Conclusions

We collected contemporaneous oceanographic data through an ice borehole and measured basal melt rates of the RIS within a few kilometers of the grounding zone. This setting is characterized by low thermal driving and low current forcing. Basal melt rates near this grounding zone embayment were less than average for the RIS (Moholdt et al., 2014; Rignot et al., 2013) and are consistent with low shear stress at the ice-shelf base. Horizontal velocities within the 10 m thick sub-ice-shelf ocean cavity were on the order of 1 cm s^{-1} and did not experience significant tidal fluctuations. These weak currents did not generate a tidally-mixed zone at this portion of the grounding zone and allowed stratification to develop at the grounding zone. Since subglacial water discharge at the grounding line that enhances shear-driven boundary-layer mixing may be focused by channels (Le Brocq et al., 2013; Marsh et al., 2016) or be episodic (Siegfried et al., 2016) this low shear regime may be typical of many grounding line settings.

The dynamics of vertical mixing are important for our understanding of the heat and salt fluxes that drive ice-shelf melting. Well-mixed layers within a few meters of the ice-shelf base and the seafloor suggest that boundary shear contributes to vertical mixing. Given low current velocities and favorable temperature and salinity gradients, we believe that double-diffusive convection may also be important. Ice-shelf melting can provide conditions favorable for double-diffusive convection by

providing a flux of freshwater and extracting heat. Conditions are favorable for double-diffusive convection in 14% of the world's oceans (You, 2002), but the extent to which double-diffusive convection controls heat and salt fluxes in sub-ice-shelf cavities is unknown. Our understanding of the relationship between double-diffusive convection and current shear must be improved to assess the role of double-diffusive convection in ice-shelf cavities.

Chapter 5 Conclusion

In this dissertation we presented three research projects that improve our ability to predict ice-sheet mass balance by advancing our understanding of the heat flux to the base of the Antarctic Ice Sheet. This heat flux is difficult to constrain because of the presence of a thick ice sheet, but through an ice-sheet drilling program (WISSARD) and ancillary measurements and experiments, we offered constraints on both the oceanic heat flux and the geothermal heat flux. Since these observations are rare, we undertook further analyses to advance our understanding of the processes that control these heat fluxes.

In Chapter 2, we reported a new direct measurement of geothermal heat flux in the West Antarctic Rift System. This measurement revealed higher than average geothermal heat flux at the grounding zone of the Whillans Ice Stream. Together with the geothermal heat flux measurement at Subglacial Lake Whillans, this indicates spatially variable geothermal heat flux within the Whillans Ice Stream. The observed spatial variability in geothermal heat flux rivals the other major contributor to basal heat flux, shear heating from ice flow over the basal substrate. Thus, spatial variability in geothermal heat flux may be glaciologically significant, even near the margins of the ice sheet where shear heating can be high. We reviewed the major geological and hydrological sources of geothermal heat flux and found that magmatic intrusions and advection by fluids may significantly contribute to its spatial variability.

Although there is evidence for West Antarctic magmatism, uncertainties in the timing of this magmatism contribute to uncertainties in the present-day magnitude and distribution of geothermal heat flux. In Chapter 3 we investigated a mechanism by which changes in ice volume control the timing of intrusive and extrusive magmatism. We translated the findings of previous studies on the relationship between ice load and dyke initiation into changes in eruption frequency over glacial cycles using a thermomechanical magma reservoir model. Magma reservoir dynamics contributed to the modeled sensitivity of magmatic systems to load changes, particularly through volatile exsolution and viscous growth of the magma reservoir. Thus, these dynamics should be considered in future analyses of the magmatic response to ice loss. Our analysis of the conditions that make volcanoes sensitive to ice loss can help identify magmatic systems that responded to ice retreat during the last deglaciation or that will respond to present-day ice retreat.

As the ice flows over the grounding zone and goes afloat, the basal heat balance changes drastically. Much more heat is available to drive melting from the ocean than in the subglacial environment. In Chapter 4 we analyze an ice-shelf grounding zone setting where sub-ice-shelf melting is quite slow compared with other grounding zone settings. The reduced melt rates that we measure below the Ross Ice Shelf are not entirely explained by the presence of colder seawater in the Ross Sea. Using contemporaneous oceanographic observations of the sub-ice-shelf cavity and measurements of ice-shelf melting, we showed that vertical eddy diffusivities of heat and salt are likely smaller than their parameterized values from other sub-ice-shelf

settings. These findings demonstrate a need to revise parameterizations of ocean mixing used to predict ice-shelf melting in ocean models.

Outlook

A new geothermal heat flux map for Antarctica

Our predictions of ice sheet mass balance may be improved when ice-sheet models use a more accurate GHF map for the Antarctic continent. Most of the commonly-used GHF maps for Antarctica and Greenland have been derived from one remotely-sensed field, such as Curie point depth or upper mantle temperature. Continental GHF maps might be better constructed by integrating different lines of evidence relevant to GHF, including direct GHF measurements. This work is already underway, through Monte-Carlo Markov Chain and gradient-based inversion methods and machine learning (TACtical Workshop 2018, Hobart Tasmania;).

There remains a need for more direct GHF measurements to constrain these models, particularly as we currently don't have a way to remotely sense relevant factors such as the heat content of magmatic intrusions, hydrothermal circulation, and groundwater flow. We recommend making GHF measurements common protocol in borehole projects that reach the ice-sheet bed given GHF's potential importance to ice dynamics. To maximize the benefit from costly ice-drilling operations, we recommend locating boreholes where GHF is most likely to affect ice dynamics and where the geothermal gradient is least likely to be contaminated by climatic changes.

A complete sensitivity analysis for volcanoes undergoing surface load changes

What are the relationships between surface load changes, magmatic conditions, and eruption likelihood? The answer to this question could improve eruption forecasting and risk assessments for magmatic systems characterized by surface load changes, such as glacial ice loss. If we understood the magmatic response to surface loading and unloading, we could also form hypotheses about the timing of magmatism in Antarctica over glacial cycles, which impacts the GHF field.

In service of building these relationships, we evaluated the sensitivity of a simplified magmatic system to surface loading and unloading while varying a small set of parameters. Some of the complexity that is likely to be important to the full sensitivity of a magmatic system to surface load changes, but was not included in this model, includes non-spherical magma reservoir geometries, magma recharge and discharge dynamics, and three-dimensional magma dynamics in the reservoir. The study of the magmatic response to surface load changes will likely proceed in a piecemeal fashion, as past investigations on this subject have coincided with the discovery of deglacial eruption patterns at specific volcanoes. However, generalized modeling studies in the vein of our study (Chapter 3) are needed to relate the trends observed at individual volcanoes to magmatic processes across multiple locales.

The sensitivity of natural magmatic systems to surface load changes has the potential to provide much needed validation of model results. It may also indicate the conditions under which magmatic systems are most sensitive to surface load changes. However, it is often difficult to deconvolve a magma reservoir's sensitivity to deglaciation from the myriad other factors that influence its eruptive history. This

difficulty has motivated statistical studies of global volcanism over periods of glacial advance and retreat (Huybers & Langmuir, 2009; Watt et al., 2013)(Huybers & Langmuir, 2009; Watt et al., 2013). Currently these estimates of eruption frequency over glacial cycles are fraught due to the incompleteness of our observational record. However, we are gradually seeing improvements in the observational record, through more accurate dating and more thorough fieldwork, and in the statistical methods for addressing incompleteness . These advances will put us in a better position to evaluate the magmatic response to ice retreat.

A framework for sub-ice-shelf vertical mixing

Accurate predictions of ice-shelf melting using ocean models likely require choosing an appropriate vertical mixing scheme for sub-ice-shelf cavities. This mixing scheme may influence ice-shelf melt rates by controlling the scale of the ice-ocean boundary layer and the heat, salt and momentum fluxes through it (Gwyther et al., . Mixing schema that have been developed for the surface boundary layer in the open ocean and the bottom boundary layer may not be appropriate for the ice-ocean boundary layer, which includes phase changes . To test these mixing schema or to derive new schema, direct observations of turbulent fluctuations in temperature, conductivity and velocity in the ice-ocean boundary layer as well as small-scale turbulence modeling are needed.

In Chapter 4 we point out that 3-equation parameterizations currently used to predict ice-shelf melting in ocean models predict melt rates spanning an order of magnitude for the same observed ocean conditions. These differences between

parameterizations can be traced back to different hypotheses about how double-diffusion will impact heat, salt and momentum fluxes in the ice-ocean boundary layer. Our ability to adjudicate between these hypotheses is limited by poor knowledge of current velocity in the boundary layer and the value of the drag coefficient. These two quantities, as well as topographic contributions to internal mixing, also need to be better determined in ocean models (Dutrieux, Pierre et al., 2014; Gwyther et al., 2015; Jenkins et al., 2010)(Dutrieux et al., 2014; Gwyther et al., 2015; Jenkins et al., 2010).

Turbulence near the ice-shelf base, and thus melt rates, are thought to be highly sensitive to the current velocity magnitude . Recent ocean modeling suggests that the tidal contribution to sub-ice-shelf currents can be significant , but it is not yet included in most ocean models of this setting. We have yet to understand why there were no significant tidal current velocity variations at the observed grounding zone site (Chapter 4). Tidal dissipation to ice-shelf flexure, drag and internal mixing may affect current velocity magnitudes at this and other sites. Ongoing research into ice-shelf flexure (Rosier et al., 2014; Wild et al., 2017)(e.g., Rosier et al., 2014; Wild et al., 2017) and longer duration oceanographic studies using sub-ice-shelf moorings may illuminate these tidal dynamics.

These developments in our understanding of ice-shelf melting will directly improve ice-sheet mass balance projections through the latest generation of ice-sheet models, which are directly coupled to ocean models . It is an exciting time to be engaged in this field of research, because of both forthcoming theoretical

developments and its direct relevance to ongoing sea level rise, an issue of great societal concern.

List of supplemental files

Chapter 2 Supplemental Materials

Chapter 3 Supplemental Materials

References

Chapter 1 References

Albino, F., Pinel, V., & Sigmundsson, F. (2010). Influence of surface load variations on eruption likelihood: application to two Icelandic subglacial volcanoes, Grímsvötn and Katla. Geophysical Journal International. https://doi.org/10.1111/j.1365-246X.2010.04603.x

An, M., Wiens, D. A., Zhao, Y., Feng, M., Nyblade, A., Kanao, M., et al. (2015). Temperature, lithosphere-asthenosphere boundary, and heat flux beneath the Antarctic Plate inferred from seismic velocities. Journal of Geophysical Research: Solid Earth, 120(12). https://doi.org/10.1002/2015JB011917

Beem, L. H., Tulaczyk, S. M., King, M. A., Bougamont, M., Fricker, H. A., & Christoffersen, P. (2014). Variable Deceleration of Whillans Ice Stream, West Antarctica. Journal of Geophysical Research: Earth Surface. https://doi.org/10.1002/2013JF002958

Bougamont, M. (2003). Response of subglacial sediments to basal freeze-on 2. Application in numerical modeling of the recent stoppage of Ice Stream C, West Antarctica. Journal of Geophysical Research, 108(B4). https://doi.org/10.1029/2002JB001936

Budd, W. F., Jenssen, D., & Smith, I. N. (1984). A three-dimensional time-dependent model of the West Antarctic ice sheet. Annals of Glaciology, 5, 29–36.

Burton-Johnson, A., Halpin, J. A., Whittaker, J. M., Graham, F. S., & Watson, S. J. (2017). A new heat flux model for the Antarctic Peninsula incorporating spatially variable upper crustal radiogenic heat production. Geophysical Research Letters, 44(11). https://doi.org/10.1002/2017GL073596

Capra, L. (2006). Abrupt climatic changes as triggering mechanisms of massive volcanic collapses. Journal of Volcanology and Geothermal Research, 155(3–4), 329–333. https://doi.org/10.1016/j.jvolgeores.2006.04.009

Carson, C. J., McLaren, S., Roberts, J. L., Boger, S. D., & Blankenship, D. D. (2014). Hot rocks in a cold place: high sub-glacial heat flow in East Antarctica. Journal of the Geological Society, 171(1), 9–12. https://doi.org/10.1144/jgs2013-030

Chen, J. L., Wilson, C. R., & Tapley, B. D. (2006). Satellite Gravity Measurements Confirm Accelerated Melting of Greenland Ice Sheet. Science, 313(5795), 1958–1960. https://doi.org/10.1126/science.1129007

Clow, G. D., Cuffey, K. M., & Waddington, E. D. (2012). High Heat-Flow Beneath the Central Portion of the West Antarctic Ice Sheet. AGU Fall Meeting Abstracts, 31. Retrieved from http://adsabs.harvard.edu/abs/2012AGUFM.C31A0577C

Conway, H., Gades, A., & Raymond, C. F. (2010). Albedo of dirty snow during conditions of melt. Water Resources Research, 32(6), 1713–1718. https://doi.org/10.1029/96WR00712

Couto, N., Martinson, D. G., Kohut, J., & Schofield, O. (2017). Distribution of Upper Circumpolar Deep Water on the warming continental shelf of the West Antarctic Peninsula. Journal of Geophysical Research: Oceans, 122(7), 5306–5315. https://doi.org/10.1002/2017JC012840

Dalziel, I. W. D., & Elliot, D. H. (1982). West Antarctica: Problem child of Gondwanaland. Tectonics, 1(1), 3–19. https://doi.org/10.1029/TC001i001p00003

Degruyter, W., & Huber, C. (2014). A model for eruption frequency of upper crustal silicic magma chambers. Earth and Planetary Science Letters, 403, 117–130. https://doi.org/10.1016/j.epsl.2014.06.047

Dinniman, M. S., Klinck, J. M., Bai, L.-S., Bromwich, D. H., Hines, K. M., & Holland, D. M. (2015). The Effect of Atmospheric Forcing Resolution on Delivery of Ocean Heat to the Antarctic Floating Ice Shelves. Journal of Climate, 28(15), 6067–6085. https://doi.org/10.1175/JCLI-D-14-00374.1

Dziadek, R., Gohl, K., Diehl, A., & Kaul, N. (2017). Geothermal heat flux in the Amundsen Sea sector of West Antarctica: New insights from temperature measurements, depth to the bottom of the magnetic source estimation, and thermal modeling. Geochemistry, Geophysics, Geosystems. https://doi.org/10.1002/2016GC006755

Engelhardt, H. (2004). Ice temperature and high geothermal flux at Siple Dome, West Antarctica, from borehole measurements. Journal of Glaciology, 50(169), 251–256. https://doi.org/10.3189/172756504781830105

Fisher, A. T., Mankoff, K. D., Tulaczyk, S. M., Tyler, S. W., Foley, N., & Team, and the W. S. (2015). High geothermal heat flux measured below the West Antarctic Ice Sheet. Science Advances, 1(6). https://doi.org/10.1126/sciadv.1500093

Fox Maule, C., Purucker, M. E., Olsen, N., & Mosegaard, K. (2005). Heat Flux Anomalies in Antarctica Revealed by Satellite Magnetic Data. Science, 309(5733), 464–467. https://doi.org/10.1126/science.1106888

Fretwell, P., Pritchard, H. D., Vaughan, D. G., Bamber, J. L., Barrand, N. E., Bell, R., et al. (2013). Bedmap2: improved ice bed, surface and thickness datasets for Antarctica. The Cryosphere, 7(1), 375–393. https://doi.org/10.5194/tc-7-375-2013

Gayen, B., Griffiths, R. W., & Kerr, R. C. (2015). Melting Driven Convection at the Ice-seawater Interface. Procedia IUTAM, 15, 78–85. https://doi.org/10.1016/j.piutam.2015.04.012

Goodge, J. W. (2018). Crustal heat production and estimate of terrestrial heat flow in central East Antarctica, with implications for thermal input to the East Antarctic ice sheet. The Cryosphere, 12(2), 491–504. https://doi.org/10.5194/tc-12-491-2018

Gudmundsson, M. T., Sigmundsson, F., & Björnsson, H. (1997). Ice–volcano interaction of the 1996 Gjálp subglacial eruption, Vatnajökull, Iceland. Nature, 389(6654), 954–957. https://doi.org/10.1038/40122

Hardarson, B. S., & Fitton, J. G. (1991). Increased mantle melting beneath Snaefellsjökull volcano during Late Pleistocene deglaciation. Nature, 353(6339), 62–64. https://doi.org/10.1038/353062a0

Hooper, A., Ófeigsson, B., Sigmundsson, F., Lund, B., Einarsson, P., Geirsson, H., & Sturkell, E. (2011). Increased capture of magma in the crust promoted by ice-cap retreat in Iceland. Nature Geoscience, 4(11), 783–786. https://doi.org/10.1038/ngeo1269

Huggel, C., Caplan-Auerbach, J., & Wessels, R. (2008). Recent Extreme Avalanches: Triggered by Climate Change? Eos, Transactions American Geophysical Union, 89(47), 469–470. https://doi.org/10.1029/2008EO470001

IOC, SCOR, & IAPSO. (2010). The international thermodynamic - 2010: Calculation and use of thermodynamic properties. Intergovernmental Oceanographic Commission Manuals and Guides, 56, 196.

Jacobs, S. S., & Giulivi, C. F. (2010). Large Multidecadal Salinity Trends near the Pacific–Antarctic Continental Margin. Journal of Climate, 23(17), 4508–4524. https://doi.org/10.1175/2010JCLI3284.1

Jarosch, A. H., & Gudmundsson, M. T. (2007). Numerical studies of ice flow over subglacial geothermal heat sources at Grímsvötn, Iceland, using Full Stokes equations. Journal of Geophysical Research: Earth Surface, 112(F2), F02008. https://doi.org/10.1029/2006JF000540

Jellinek, A. M., Manga, M., & Saar, M. O. (2004). Did melting glaciers cause volcanic eruptions in eastern California? Probing the mechanics of dike formation. Journal of Geophysical Research: Solid Earth, 109(B9), B09206. https://doi.org/10.1029/2004JB002978

Jenkins, A., Nicholls, K. W., & Corr, H. F. J. (2010). Observation and Parameterization of Ablation at the Base of Ronne Ice Shelf, Antarctica. Journal of Physical Oceanography, 40(10), 2298–2312. https://doi.org/10.1175/2010JPO4317.1

Jull, M., & McKenzie, D. (1996). The effect of deglaciation on mantle melting beneath Iceland. Journal of Geophysical Research: Solid Earth, 101(B10), 21815–21828. https://doi.org/10.1029/96JB01308

Martos, Y. M., Catalán, M., Jordan, T. A., Golynsky, A. V., Golynsky, D., Eagles, G., & Vaughan, D. G. (2017). Heat Flux Distribution of Antarctica Unveiled. Geophysical Research Letters, 44(22), 11,417-11,426. https://doi.org/10.1002/2017GL075609

Marzeion, B., Jarosch, A. H., & Hofer, M. (2012). Past and future sea-level change from the surface mass balance of glaciers. The Cryosphere; Katlenburg-Lindau, 6(6), 1295. http://dx.doi.org/10.5194/tc-6-1295-2012

McPhee, M. G. (1981). An analytic similarity theory for the planetary boundary layer stabilized by surface buoyancy. Boundary-Layer Meteorology, 21(3), 325–339. https://doi.org/10.1007/BF00119277

Mengel, M., Levermann, A., Frieler, K., Robinson, A., Marzeion, B., & Winkelmann, R. (2016). Future sea level rise constrained by observations and long-term commitment. Proceedings of the National Academy of Sciences, 113(10), 2597–2602. https://doi.org/10.1073/pnas.1500515113

Mueller, R. D., Hattermann, T., Howard, S. L., & Padman, L. (2018). Tidal influences on a future evolution of the Filchner–Ronne Ice Shelf cavity in the Weddell Sea, Antarctica. The Cryosphere, 12(2), 453–476. https://doi.org/10.5194/tc-12-453-2018

Nakada, M., & Yokose, H. (1992). Ice age as a trigger of active Quaternary volcanism and tectonism. Tectonophysics, 212(3–4), 321–329. https://doi.org/10.1016/0040-1951(92)90298-K

Näslund, J.-O., Jansson, P., Fastook, J. L., Johnson, J., & Andersson, L. (2005). Detailed spatially distributed geothermal heat-flow data for modeling of basal temperatures and meltwater production beneath the Fennoscandian ice sheet. Annals of Glaciology, 40(1), 95–101. https://doi.org/10.3189/172756405781813582

Nerem, R. S., Chambers, D. P., Choe, C., & Mitchum, G. T. (2010). Estimating Mean Sea Level Change from the TOPEX and Jason Altimeter Missions. Marine Geodesy, 33(sup1), 435–446. https://doi.org/10.1080/01490419.2010.491031

Paul Segall, Peter Cervelli, Susan Owen, Mike Lisowski, & Asta Miklius. (2001). Constraints on dike propagation from continuous GPS measurements. Journal of Geophysical Research: Solid Earth, 106(B9), 19301–19317. https://doi.org/10.1029/2001JB000229

Pittard, M. L., Galton-Fenzi, B. K., Roberts, J. L., & Watson, C. S. (2016). Organization of ice flow by localized regions of elevated geothermal heat flux. Geophysical Research Letters, 43(7). https://doi.org/10.1002/2016GL068436

Radko, T. (2013). Double-diffusive convection. Cambridge: Cambridge University PRess.

Rawson, H., Pyle, D. M., Mather, T. A., Smith, V. C., Fontijn, K., Lachowycz, S. M., & Naranjo, J. A. (2016). The magmatic and eruptive response of arc volcanoes to deglaciation: Insights from southern Chile. Geology, 44(4), 251–254. https://doi.org/10.1130/G37504.1

Reese, R., Gudmundsson, G. H., Levermann, A., & Winkelmann, R. (2018). The far reach of ice-shelf thinning in Antarctica. Nature Climate Change, 8(1), 53. https://doi.org/10.1038/s41558-017-0020-x

Rignot, E., Casassa, G., Gogineni, P., Krabill, W., Rivera, A., & Thomas, R. (2004). Accelerated ice discharge from the Antarctic Peninsula following the collapse of Larsen B ice shelf. Geophysical Research Letters, 31(18). https://doi.org/10.1029/2004GL020697

Rignot, E., Bamber, J. L., van den Broeke, M. R., Davis, C., Li, Y., van de Berg, W. J., & van Meijgaard, E. (2008). Recent Antarctic ice mass loss from radar

interferometry and regional climate modelling. Nature Geoscience, 1(2), 106–110. https://doi.org/10.1038/ngeo102

Rignot, E., Mouginot, J., & Scheuchl, B. (2011). Ice Flow of the Antarctic Ice Sheet. Science, 333(6048), 1427–1430. https://doi.org/10.1126/science.1208336

Rignot, E., Jacobs, S., Mouginot, J., & Scheuchl, B. (2013). Ice-Shelf Melting Around Antarctica. Science, 341(6143), 266–270. https://doi.org/10.1126/science.1235798

Schmidtko, S., Heywood, K. J., Thompson, A. F., & Aoki, S. (2014). Multidecadal warming of Antarctic waters. Science, 346(6214), 1227–1231. https://doi.org/10.1126/science.1256117

Schodlok, M. P., Menemenlis, D., & Rignot, E. J. (2016). Ice shelf basal melt rates around Antarctica from simulations and observations. Journal of Geophysical Research: Oceans, 121(2), 1085–1109. https://doi.org/10.1002/2015JC011117

Schroeder, D. M., Blankenship, D. D., Young, D. A., & Quartini, E. (2014). Evidence for elevated and spatially variable geothermal flux beneath the West Antarctic Ice Sheet. Proceedings of the National Academy of Sciences. https://doi.org/10.1073/pnas.1405184111

Seroussi, H., Ivins, E. R., Wiens, D. A., & Bondzio, J. (2017). Influence of a West Antarctic mantle plume on ice sheet basal conditions. Journal of Geophysical Research: Solid Earth, 2017JB014423. https://doi.org/10.1002/2017JB014423

Siegert, M. J., & Dowdeswell, J. A. (1996). Spatial variations in heat at the base of the Antarctic ice sheet from analysis of the thermal regime above subglacial lakes. Journal of Glaciology, 42(142), 501–509.

Sigvaldason, G. E., Annertz, K., & Nilsson, M. (1992). Effect of glacier loading/deloading on volcanism: postglacial volcanic production rate of the Dyngjufjöll area, central Iceland. Bulletin of Volcanology, 54(5), 385–392. https://doi.org/10.1007/BF00312320

Smellie, J.L., McArthur, J. M., McIntosh, W. C., & Esser, R. (2006). Late Neogene interglacial events in the James Ross Island region, northern Antarctic Peninsula, dated by Ar/Ar and Sr-isotope stratigraphy. Palaeogeography, Palaeoclimatology, Palaeoecology, 242(3–4), 169–187. https://doi.org/10.1016/j.palaeo.2006.06.003

Smellie, John L., & Edwards, B. R. (2016). Glaciovolcanism on Earth and Mars: Products, Processes and Palaeoenvironmental Significance. Cambridge: Cambridge University Press. https://doi.org/10.1017/CBO9781139764384

Stanton, T. P., Shaw, W. J., Truffer, M., Corr, H. F. J., Peters, L. E., Riverman, K. L., et al. (2013). Channelized Ice Melting in the Ocean Boundary Layer Beneath Pine Island Glacier, Antarctica. Science, 341(6151), 1236–1239. https://doi.org/10.1126/science.1239373

Sternai, P., Caricchi, L., Castelltort, S., & Champagnac, J.-D. (2016). Deglaciation and glacial erosion: A joint control on magma productivity by continental unloading. Geophysical Research Letters, 43(4), 2015GL067285. https://doi.org/10.1002/2015GL067285

Stevens, N. T., Parizek, B. R., & Alley, R. B. (2016). Enhancement of volcanism and geothermal heat flux by ice-age cycling: A stress modeling study of Greenland. Journal of Geophysical Research: Earth Surface, 2016JF003855. https://doi.org/10.1002/2016JF003855

Tuffen, H. (2010). How will melting of ice affect volcanic hazards in the twenty-first century? Philosophical Transactions of the Royal Society of London A: Mathematical, Physical and Engineering Sciences, 368(1919), 2535–2558. https://doi.org/10.1098/rsta.2010.0063

Turner, J. S. (1965). The coupled turbulent transports of salt and and heat across a sharp density interface. International Journal of Heat and Mass Transfer, 8(5), 759–767. https://doi.org/10.1016/0017-9310(65)90022-0

Wannamaker, P., Hill, G., Stodt, J., Maris, V., Ogawa, Y., Selway, K., et al. (2017). Uplift of the central transantarctic mountains. Nature Communications, 8(1), 1588. https://doi.org/10.1038/s41467-017-01577-2

Watt, S. F. L., Pyle, D. M., & Mather, T. A. (2013). The volcanic response to deglaciation: Evidence from glaciated arcs and a reassessment of global eruption records. Earth-Science Reviews, 122, 77–102. https://doi.org/10.1016/j.earscirev.2013.03.007

Weertman, J. (1983). Creep Deformation of Ice. Annual Review of Earth and Planetary Sciences, 11(1), 215–240. https://doi.org/10.1146/annurev.ea.11.050183.001243

Chapter 2 References

An, M., D. A. Wiens, Y. Zhao, M. Feng, A. Nyblade, M. Kanao, Y. Li, A. Maggi, and J.-J. Lévêque (2015), Temperature, lithosphere-asthenosphere boundary, and heat flux beneath the Antarctic Plate inferred from seismic velocities, J. Geophys. Res. Solid Earth, 120(12), doi:10.1002/2015JB011917.

Anandakrishnan, S., D. D. Blankenship, R. B. Alley, and P. L. Stoffa (1998), Influence of subglacial geology on the position of a West Antarctic ice stream from seismic observations, *Nature*, *394*(6688), 62–65, doi:10.1038/27889.

Anandakrishnan, S., and J. P. Winberry (2004), Antarctic subglacial sedimentary layer thickness from receiver function analysis, *Glob. Planet. Change*, *42*(1–4), 167–176, doi:10.1016/j.gloplacha.2003.10.005.

Armienti, P., and C. Perinelli (2010), Cenozoic thermal evolution of lithospheric mantle in northern Victoria Land (Antarctica): Evidences from mantle xenoliths, *Tectonophysics*, *486*(1–4), 28–35, doi:10.1016/j.tecto.2010.02.006.

Arthern, R. J., Winebrenner, D. P., & Vaughan, D. G. (2006). Antarctic snow accumulation mapped using polarization of 4.3-cm wavelength microwave emission. Journal of Geophysical Research, 111(D6), D06107. https://doi.org/10.1029/2004JD005667

Behrendt, J. C., D. D. Blankenship, C. A. Finn, R. E. Bell, R. E. Sweeney, S. M. Hodge, and J. M. Brozena (1994), CASERTZ aeromagnetic data reveal late Cenozoic flood basalts(?) in the West Antarctic rift system, *Geology*, *22*(6), 527–530, doi:10.1130/0091-7613(1994)022<0527:CADRLC>2.3.CO;2.

Berg, J. H., R. J. Moscati, and D. L. Herz (1989), A petrologic geotherm from a continental rift in Antarctica, *Earth Planet. Sci. Lett.*, *93*(1), 98–108, doi:10.1016/0012-821X(89)90187-8.

Bindschadler, R. A., E. P. Roberts, and A. Iken (1990), Age of Crary Ice Rise, Antarctica, determined from temperature-depth profiles, *Ann. Glaciol.*, *14*, 13–16.

Bingham, R. G., F. Ferraccioli, E. C. King, R. D. Larter, H. D. Pritchard, A. M. Smith, and D. G. Vaughan (2012), Inland thinning of West Antarctic Ice Sheet steered along subglacial rifts, *Nature*, *487*(7408), 468–471, doi:10.1038/nature11292.

Blankenship, D. D., R. E. Bell, S. M. Hodge, J. M. Brozena, J. C. Behrendt, and C. A. Finn (1993), Active volcanism beneath the West Antarctic ice sheet and implications for ice-sheet stability, *Nature*, *361*(6412), 526–529, doi:10.1038/361526a0.

Bougamont, M., P. Christoffersen, S. F. Price, H. A. Fricker, S. Tulaczyk, and S. P. Carter (2015), Reactivation of Kamb Ice Stream tributaries triggers century-scale reorganization of Siple Coast ice flow in West Antarctica: Restructuring of Siple Coast ice flow, *Geophys. Res. Lett.*, *42*(20), 8471–8480, doi:10.1002/2015GL065782.

Bredehoeft, J. D., and I. S. Papadopulos (1965), Rates of vertical groundwater movement estimated from the Earth's thermal profile, *Water Resour. Res.*, *1*(2), 325–328, doi:10.1029/WR001i002p00325.

Brigaud, F., and G. Vasseur (1989), Mineralogy, porosity and fluid control on thermal conductivity of sedimentary rocks, *Geophys. J. Int.*, *98*(3), 525–542, doi:10.1111/j.1365-246X.1989.tb02287.x.

Bullard, E. C. (1939). Heat Flow in South Africa. Proceedings of the Royal Society of London. Series A, Mathematical and Physical Sciences, 173(955), 474–502. https://doi.org/10.2307/97404

Bullard, E. (1954), The Flow of Heat through the Floor of the Atlantic Ocean, *Proc. R. Soc. Lond. Math. Phys. Eng. Sci.*, *222*(1150), 408–429, doi:10.1098/rspa.1954.0085.

Burton-Johnson, A., J. A. Halpin, J. M. Whittaker, F. S. Graham, and S. J. Watson (2017), A new heat flux model for the Antarctic Peninsula incorporating spatially variable upper crustal radiogenic heat production, *Geophys. Res. Lett.*, *44*(11), doi:10.1002/2017GL073596.

Cande, S. C., J. M. Stock, R. D. Müller, and T. Ishihara (2000), Cenozoic motion between East and West Antarctica, *Nature*, *404*(6774), 145–150, doi:10.1038/35004501.

Carslaw, H. S., and J. C. Jaeger (1947), *Conduction of heat in solids*, Oxford Clarendon Press.

Carson, C. J., S. McLaren, J. L. Roberts, S. D. Boger, and D. D. Blankenship (2014), Hot rocks in a cold place: high sub-glacial heat flow in East Antarctica, *J. Geol. Soc.*, *171*(1), 9–12, doi:10.1144/jgs2013-030.

Chaput, J., R. C. Aster, A. Huerta, X. Sun, A. Lloyd, D. Wiens, A. Nyblade, S. Anandakrishnan, J. P. Winberry, and T. Wilson (2014), The crustal thickness of West Antarctica, *J. Geophys. Res. Solid Earth*, *119*(1), 378–395, doi:10.1002/2013JB010642.

Christner, B. C. et al. (2014), A microbial ecosystem beneath the West Antarctic ice sheet, *Nature*, *512*(7514), 310–313, doi:10.1038/nature13667.

Christoffersen, P., M. Bougamont, S. P. Carter, H. A. Fricker, and S. Tulaczyk (2014), Significant groundwater contribution to Antarctic ice streams hydrologic budget, *Geophys. Res. Lett.*, *41*(6), 2014GL059250, doi:10.1002/2014GL059250.

Clauser, C., and E. Huenges (1995), Thermal conductivity of rocks and minerals, *Rock Phys. Phase Relat. Handb. Phys. Constants*, 105–126.

Clow, G. D., K. M. Cuffey, and E. D. Waddington (2012), High Heat-Flow Beneath the Central Portion of the West Antarctic Ice Sheet, *AGU Fall Meet. Abstr.*, *31*.

Comiso, J. C. (2000), Variability and Trends in Antarctic Surface Temperatures from In Situ and Satellite Infrared Measurements, *J. Clim.*, *13*(10), 1674–1696, doi:10.1175/1520-0442(2000)013<1674:VATIAS>2.0.CO;2.

Coney, P. J., and T. A. Harms (1984), Cordilleran metamorphic core complexes: Cenozoic extensional relics of Mesozoic compression, *Geology*, *12*(9), 550–554, doi:10.1130/0091-7613(1984)12<550:CMCCCE>2.0.CO;2.

Corr, H. F. J., and D. G. Vaughan (2008), A recent volcanic eruption beneath the West Antarctic ice sheet, *Nat. Geosci.*, *1*(2), 122–125, doi:10.1038/ngeo106.

Cuffey, K., and W. S. B. Paterson (2010), *The physics of glaciers*, 4th ed., Butterworth-Heinemann/Elsevier, Burlington, MA.

Davies, J. H., and D. R. Davies (2010), Earth's surface heat flux, *Solid Earth*, *1*(1), 5–24.

Davis, E. E., and A. T. Fisher (2011), Heat Flow, Seafloor: Methods and Observations, in *Encyclopedia of Solid Earth Geophysics*, edited by H. K. Gupta, pp. 582–591, Springer Netherlands.

Davis, E. E. et al. (1992), FlankFlux: an experiment to study the nature of hydrothermal circulation in young oceanic crust, *Can. J. Earth Sci.*, *29*(5), 925–952, doi:10.1139/e92-078.

Davis, E. E., K. Wang, J. He, D. S. Chapman, H. Villinger, and A. Rosenberger (1997), An unequivocal case for high Nusselt number hydrothermal convection in sediment-buried igneous oceanic crust, *Earth Planet. Sci. Lett.*, *146*(1), 137–150, doi:10.1016/S0012-821X(96)00212-9.

Decesari, R., D. Wilson, B. Luyendyk, and M. Faulkner (2007), Cretaceous and Tertiary extension throughout the Ross Sea, Antarctica, in Antarctica: A Keystone in a Changing World, in *Online Proceedings of the 11ISAES*, vol. Short Research Paper 098, edited by A. K. Cooper, C. R. Raymond, et al., p. 6 p.

Dziadek, R., K. Gohl, A. Diehl, and N. Kaul (2017), Geothermal heat flux in the Amundsen Sea sector of West Antarctica: New insights from temperature measurements, depth to the bottom of the magnetic source estimation, and thermal modeling, *Geochem. Geophys. Geosystems*, doi:10.1002/2016GC006755.

Engelhardt, H. (2004a), Ice temperature and high geothermal flux at Siple Dome, West Antarctica, from borehole measurements, *J. Glaciol.*, *50*(169), 251–256, doi:10.3189/172756504781830105.

Engelhardt, H. (2004b), Thermal regime and dynamics of the West Antarctic ice sheet, *Ann. Glaciol.*, *39*(1), 85–92, doi:10.3189/172756404781814203.

Favier, L., and F. Pattyn (2015), Antarctic ice rise formation, evolution, and stability, *Geophys. Res. Lett.*, *42*(11), doi:10.1002/2015GL064195.

Fisher, A. T., and R. N. Harris (2010), Using seafloor heat flow as a tracer to map subseafloor fluid flow in the ocean crust, *Geofluids*, doi:10.1111/j.1468-8123.2009.00274.x.

Fisher, A. T., K. Becker, I. T. N. Narasimhan, M. G. Langseth, and M. J. Mottl (1990), Passive, off-axis convection through the southern flank of the Costa Rica Rift, *J. Geophys. Res. Solid Earth*, *95*(B6), 9343–9370, doi:10.1029/JB095iB06p09343.

Fisher, A. T. et al. (2003), Hydrothermal recharge and discharge across 50 km guided by seamounts on a young ridge flank, *Nature*, *421*(6923), 618–621, doi:10.1038/nature01352.

Fisher, A. T., K. D. Mankoff, S. M. Tulaczyk, S. W. Tyler, N. Foley, and the W. S. Team (2015), High geothermal heat flux measured below the West Antarctic Ice Sheet, *Sci. Adv.*, *1*(6), doi:10.1126/sciadv.1500093.

Foster, T. D. (1978), Temperature and salinity fields under the Ross Ice Shelf, *Antarct. J*, *13*, 81–82.

Fox Maule, C., Purucker, M. E., Olsen, N., & Mosegaard, K. (2005). Heat flux anomalies in Antarctica revealed by satellite magnetic data. Science, 309(5,733), 464–467. https://doi.org/10.1126/science.1106888

Fretwell, P. et al. (2013), Bedmap2: improved ice bed, surface and thickness datasets for Antarctica, *The Cryosphere*, *7*(1), 375–393, doi:10.5194/tc-7-375-2013.

Fudge, T. J., E. J. Steig, B. R. Markle, S. W. Schoenemann, and Q. Ding (2013), Onset of deglacial warming in West Antarctica driven by local orbital forcing, *Nature*, *500*(7463), 440–444, doi:10.1038/nature12376.

Gangadhara Rao, M., and D. N. Singh (1999), A generalized relationship to estimate thermal resistivity of soils, *Can. Geotech. J.*, *36*(4), 767–773, doi:10.1139/t99-037.

Hasterok, D., and D. S. Chapman (2011), Heat production and geotherms for the continental lithosphere, *Earth Planet. Sci. Lett.*, *307*(1–2), 59–70, doi:10.1016/j.epsl.2011.04.034.

Heesemann, M., H. Villinger, A. T. Fisher, A. M. Trehu, and S. Witte (2006), *Testing and deployment of the new APC3 tool to determine in situ temperature while piston coring*, Proceedings of the IODP, edited by M. Riedel, T. S. Collett, M. J. Malone, and Expedition 311 Scientists, Integrated Ocean Drilling Program Management International Inc., College Station, TX.

Hirschmann, M. M. (2000), Mantle solidus: Experimental constraints and the effects of peridotite composition, *Geochem. Geophys. Geosystems*, *1*(10), 1042, doi:10.1029/2000GC000070.

Intergovernmental Oceanographic Commission, Scientific Committee on Oceanic Research, & International Association for the Physical Sciences of the Oceans (2010), The international thermodynamic - 2010: Calculation and use of thermodynamic properties, *Intergov. Oceanogr. Comm. Man. Guid.*, *56*, 196.

Jørgensen, B. B., and A. Boetius (2007), Feast and famine — microbial life in the deep-sea bed, *Nat. Rev. Microbiol.*, *5*(10), 770–781, doi:10.1038/nrmicro1745.

Kingslake, J., R. C. A. Hindmarsh, G. Aðalgeirsdóttir, H. Conway, H. F. J. Corr, F. Gillet-Chaulet, C. Martín, E. C. King, R. Mulvaney, and H. D. Pritchard (2014), Full-depth englacial vertical ice sheet velocities measured using phase-sensitive

radar, *J. Geophys. Res. Earth Surf.*, *119*(12), 2014JF003275, doi:10.1002/2014JF003275.

Lachenbruch, A. H., and J. H. Sass (1978), 9: Models of an extending lithosphere and heat flow in the Basin and Range province, *Geol. Soc. Am. Mem.*, *152*, 209–250, doi:10.1130/MEM152-p209.

Lachenbruch, A. H., J. H. Sass, R. J. Munroe, and T. H. Moses (1976), Geothermal setting and simple heat conduction models for the Long Valley Caldera, *J. Geophys. Res.*, *81*(5), 769–784, doi:10.1029/JB081i005p00769.

LeMasurier, W. E. (1990), Late Cenozoic Volcanism on the Antarctic Plate: An Overview, in *Volcanoes of the Antarctic Plate and Southern Oceans*, edited by W. E. LeMasurier, J. W. Thomson, P. E. Baker, P. R. Kyle, P. D. Rowley, J. L. Smellie, and W. J. Verwoerd, pp. 1–17, American Geophysical Union.

Lough, A. C., D. A. Wiens, C. Grace Barcheck, S. Anandakrishnan, R. C. Aster, D. D. Blankenship, A. D. Huerta, A. Nyblade, D. A. Young, and T. J. Wilson (2013), Seismic detection of an active subglacial magmatic complex in Marie Byrd Land, Antarctica, *Nat. Geosci.*, *6*(12), 1031–1035, doi:10.1038/ngeo1992.

Mancktelow, N. S., and B. Grasemann (1997), Time-dependent effects of heat advection and topography on cooling histories during erosion, *Tectonophysics*, *270*(3–4), 167–195, doi:10.1016/S0040-1951(96)00279-X.

Morin, R., and A. J. Silva (1984), The effects of high pressure and high temperature on some physical properties of ocean sediments, *J. Geophys. Res. Solid Earth*, *89*(B1), 511–526, doi:10.1029/JB089iB01p00511.

Morin, R. H., Williams, T., Henrys, S. A., Magens, D., Niessen, F., & Hansaraj, D. (2010). Heat Flow and Hydrologic Characteristics at the AND-1B borehole, ANDRILL McMurdo Ice Shelf Project, Antarctica. Geosphere, 6(4), 370–378. https://doi.org/10.1130/GES00512.1

Muto, A., K. Christianson, H. J. Horgan, S. Anandakrishnan, and R. B. Alley (2013), Bathymetry and geological structures beneath the Ross Ice Shelf at the mouth of Whillans Ice Stream, West Antarctica, modeled from ground-based gravity measurements: Grounding zone and subglacial conditions, *J. Geophys. Res. Solid Earth*, *118*(8), 4535–4546, doi:10.1002/jgrb.50315.

Paterson, W. S. B. (1976), Vertical Strain-rate Measurements in an Arctic Ice Cap and deductions from them, *J. Glaciol.*, *17*(75), 3–12, doi:10.1017/S0022143000030665.

Pittard, M. L., B. K. Galton-Fenzi, J. L. Roberts, and C. S. Watson (2016), Organization of ice flow by localized regions of elevated geothermal heat flux, *Geophys. Res. Lett.*, *43*(7), doi:10.1002/2016GL068436.

Pollack, H. N., S. J. Hurter, and J. R. Johnson (1993), Heat flow from the Earth's interior: Analysis of the global data set, *Rev. Geophys.*, *31*(3), 267–280, doi:10.1029/93RG01249.

Price, S. F., H. Conway, and E. D. Waddington (2007), Evidence for late Pleistocene thinning of Siple Dome, West Antarctica, *J. Geophys. Res. Earth Surf.*, *112*(F3), F03021, doi:10.1029/2006JF000725.

Raymond, C. F. (1983), Deformation in the Vicinity of Ice Divides, *J. Glaciol.*, *29*(103), 357–373, doi:10.3198/1983JoG29-103-357-373.

Raymond, C. (1996), Shear margins in glaciers and ice sheets, *J. Glaciol.*, *42*(140), 90–102.

Reiter, M., C. L. Edwards, H. Hartman, and C. Weidman (1975), Terrestrial Heat Flow along the Rio Grande Rift, New Mexico and Southern Colorado, *Geol. Soc. Am. Bull.*, *86*(6), 811–818, doi:10.1130/0016-7606(1975)86<811:THFATR>2.0.CO;2.

Rignot, E., G. Casassa, P. Gogineni, W. Krabill, A. Rivera, and R. Thomas (2004), Accelerated ice discharge from the Antarctic Peninsula following the collapse of Larsen B ice shelf, *Geophys. Res. Lett.*, *31*(18), doi:10.1029/2004GL020697.

Rignot, E., J. Mouginot, and B. Scheuchl (2011), Ice Flow of the Antarctic Ice Sheet, *Science*, *333*(6048), 1427–1430, doi:10.1126/science.1208336.

Robin, G. D. Q. (1955), Ice Movement and Temperature Distribution in Glaciers and Ice Sheets, *J. Glaciol.*, *2*(18), 523–532, doi:10.3189/002214355793702028.

Schroeder, D. M., D. D. Blankenship, D. A. Young, and E. Quartini (2014), Evidence for elevated and spatially variable geothermal flux beneath the West Antarctic Ice Sheet, *Proc. Natl. Acad. Sci.*, doi:10.1073/pnas.1405184111.

Schröder, H., Paulsen, T., & Wonik, T. (2011). Thermal properties of the AND-2A borehole in the southern Victoria Land Basin, McMurdo Sound, Antarctica. Geosphere, 7(6), 1324–1330. https://doi.org/10.1130/GES00690.1

Seront, B., T.-F. Wong, J. S. Caine, C. B. Forster, R. L. Bruhn, and J. T. Fredrich (1998), Laboratory characterization of hydromechanical properties of a seismogenic normal fault system, *J. Struct. Geol.*, *20*(7), 865–881, doi:10.1016/S0191-8141(98)00023-6.

Seroussi, H., Ivins, E. R., Wiens, D. A., & Bondzio, J. (2017). Influence of a West Antarctic mantle plume on ice sheet basal conditions. Journal of Geophysical Research: Solid Earth, 122. https://doi.org/10.1002/2017JB014423

Shapiro, N. M., and M. H. Ritzwoller (2004), Inferring surface heat flux distributions guided by a global seismic model: particular application to Antarctica, *Earth Planet. Sci. Lett.*, *223*(1–2), 213–224, doi:10.1016/j.epsl.2004.04.011.

Siegert, M. J., and J. A. Dowdeswell (1996), Spatial variations in heat at the base of the Antarctic ice sheet from analysis of the thermal regime above subglacial lakes, *J. Glaciol.*, *42*(142), 501–509.

Spinelli, G. A., and A. T. Fisher (2004), Hydrothermal circulation within topographically rough basaltic basement on the Juan de Fuca Ridge flank, *Geochem. Geophys. Geosystems*, *5*(2), doi:10.1029/2003GC000616.

Swanberg, C. A. (1972), Vertical distribution of heat generation in the Idaho batholith, *J. Geophys. Res.*, *77*(14), 2508–2513, doi:10.1029/JB077i014p02508.

Trey, H., A. K. Cooper, G. Pellis, B. della Vedova, G. Cochrane, G. Brancolini, and J. Makris (1999), Transect across the West Antarctic rift system in the Ross Sea, Antarctica, *Tectonophysics*, *301*(1–2), 61–74, doi:10.1016/S0040-1951(98)00155-3.

Tulaczyk, S., Kamb, W. B., & Engelhardt, H. F. (2000). Basal mechanics of Ice Stream B, West Antarctica 1. Till mechanics. Journal of Geophysical Research, 105. 463–482. https://doi.org/DOI: 10.1029/1999JB900329

Tulaczyk, S., B. Kamb, and H. F. Engelhardt (2001), Estimates of effective stress beneath a modern West Antarctic ice stream from till preconsolidation and void ratio, *Boreas*, *30*(2), 101–114, doi:10.1111/j.1502-3885.2001.tb01216.x.

Tulaczyk, S. et al. (2014), WISSARD at Subglacial Lake Whillans, West Antarctica: scientific operations and initial observations, *Ann. Glaciol.*, *55*(65), 51–58, doi:10.3189/2014AoG65A009.

van de Berg, W. J., van den Broeke, M. R., Reijmer, C. H., & van Meijgaard, E. (2006). Reassessment of the Antarctic surface mass balance using calibrated output of a regional atmospheric climate model. Journal of Geophysical Research, 111(D11), D11104. https://doi.org/10.1029/2005JD006495

Vilà, M., M. Fernández, and I. Jiménez-Munt (2010), Radiogenic heat production variability of some common lithological groups and its significance to lithospheric thermal modeling, *Tectonophysics*, *490*(3–4), 152–164, doi:10.1016/j.tecto.2010.05.003.

Villinger, H., I. Grevemeyer, N. Kaul, J. Hauschild, and M. Pfender (2002), Hydrothermal heat flux through aged oceanic crust: where does the heat escape?, *Earth Planet. Sci. Lett.*, *202*(1), 159–170, doi:10.1016/S0012-821X(02)00759-8.

Vogel, S. W., and S. Tulaczyk (2006), Ice-dynamical constraints on the existence and impact of subglacial volcanism on West Antarctic ice sheet stability, *Geophys. Res. Lett.*, *33*(23), doi:10.1029/2006GL027345.

Von Herzen, R., and A. E. Maxwell (1959), The measurement of thermal conductivity of deep-sea sediments by a needle-probe method, *J. Geophys. Res.*, *64*(10), 1557–1563, doi:10.1029/JZ064i010p01557.

Weertman, J. (1964), The theory of glacier sliding, *J. Glaciol.*, *5*, 287–303.

Wilson, D. S., S. S. R. Jamieson, P. J. Barrett, G. Leitchenkov, K. Gohl, and R. D. Larter (2012), Antarctic topography at the Eocene–Oligocene boundary, *Palaeogeogr. Palaeoclimatol. Palaeoecol.*, *335–336*, 24–34, doi:10.1016/j.palaeo.2011.05.028.

York, D., N. M. Evensen, M. L. Martínez, and J. D. B. Delgado (2004), Unified equations for the slope, intercept, and standard errors of the best straight line, *Am. J. Phys.*, *72*(3), 367–375, doi:10.1119/1.1632486.

Zumberge, M. A., D. H. Elsberg, W. D. Harrison, E. Husmann, J. L. Morack, E. C. Pettit, and E. D. Waddington (2002), Measurement of vertical strain and velocity at Siple Dome, Antarctica, with optical sensors, *J. Glaciol.*, *48*(161), 217–225, doi:10.3189/172756502781831421.

Chapter 3 References

Albino, F., Pinel, V., & Sigmundsson, F. (2010). Influence of surface load variations on eruption likelihood: application to two Icelandic subglacial volcanoes, Grímsvötn and Katla. Geophysical Journal International. https://doi.org/10.1111/j.1365-246X.2010.04603.x

Bacon, C. R., & Lanphere, M. A. (2006). Eruptive history and geochronology of Mount Mazama and the Crater Lake region, Oregon. Geological Society of America Bulletin, 118(11–12), 1331–1359. https://doi.org/10.1130/B25906.1

Bakker, R. R., Frehner, M., & Lupi, M. (2016). How temperature-dependent elasticity alters host rock/magmatic reservoir models: A case study on the effects of ice-cap unloading on shallow volcanic systems. Earth and Planetary Science Letters, 456, 16–25. https://doi.org/10.1016/j.epsl.2016.09.039

Broecker, W. S. (1984). Terminations. In A. Berger, J. Imbrie, J. Hays, G. Kukla, & B. Saltzman (Eds.), Milankovitch and Climate (pp. 687–698). Dordrecht: Springer Netherlands. https://doi.org/10.1007/978-94-017-4841-4_14

Capra, L. (2006). Abrupt climatic changes as triggering mechanisms of massive volcanic collapses. Journal of Volcanology and Geothermal Research, 155(3–4), 329–333. https://doi.org/10.1016/j.jvolgeores.2006.04.009

Caricchi, L., Annen, C., Blundy, J., Simpson, G., & Pinel, V. (2014). Frequency and magnitude of volcanic eruptions controlled by magma injection and buoyancy. Nature Geoscience, 7(2), 126–130. https://doi.org/10.1038/ngeo2041

Carlson, A. E., LeGrande, A. N., Oppo, D. W., Came, R. E., Schmidt, G. A., Anslow, F. S., et al. (2008). Rapid early Holocene deglaciation of the Laurentide ice sheet. Nature Geoscience, 1(9), 620–624. https://doi.org/10.1038/ngeo285

Committee on Improving Understanding of Volcanic Eruptions, Committee on Seismology and Geodynamics, Board on Earth Sciences, Division on Earth and Life Studies, & National Academies of Sciences, Engineering, and Medicine. (2017). Volcanic Eruptions and Their Repose, Unrest, Precursors, and Timing. Washington, D.C.: National Academies Press. https://doi.org/10.17226/24650

Degruyter, W., & Huber, C. (2014). A model for eruption frequency of upper crustal silicic magma chambers. Earth and Planetary Science Letters, 403, 117–130. https://doi.org/10.1016/j.epsl.2014.06.047

Dufek, J., & Bergantz, G. W. (2005). Lower Crustal Magma Genesis and Preservation: a Stochastic Framework for the Evaluation of Basalt–Crust Interaction. Journal of Petrology, 46(11), 2167–2195. https://doi.org/10.1093/petrology/egi049

Dungan, M. A., Wulff, A., & Thompson, R. (2001). Eruptive Stratigraphy of the Tatara–San Pedro Complex, 36°S, Southern Volcanic Zone, Chilean Andes: Reconstruction Method and Implications for Magma Evolution at Long-lived Arc Volcanic Centers. Journal of Petrology, 42(3), 555–626. https://doi.org/10.1093/petrology/42.3.555

Flóvenz, Ó. G., & Saemundsson, K. (1993). Heat Flow and the Structure of the Lithosphere Heat flow and geothermal processes in Iceland. Tectonophysics, 225(1), 123–138. https://doi.org/10.1016/0040-1951(93)90253-G

Friedman, I., Long, W., & Smith, R. L. (1963). Viscosity and water content of rhyolite glass. Journal of Geophysical Research, 68(24), 6523–6535. https://doi.org/10.1029/JZ068i024p06523

Glazner, A. F., Manley, C. R., Damgaard, J. S., & Rojstaczer, S. (1999). Fire or ice: anticorrelation of volcanism and glaciation in California over the past 800,000 years. Geophysical Research Letters, 26(12), 1759–1762. https://doi.org/10.1029/1999GL900333

Grosfils, E. B. (2007). Magma reservoir failure on the terrestrial planets: Assessing the importance of gravitational loading in simple elastic models. Journal of Volcanology and Geothermal Research, 166(2), 47–75. https://doi.org/10.1016/j.jvolgeores.2007.06.007

Gudmundsson, A. (2006). How local stresses control magma-chamber ruptures, dyke injections, and eruptions in composite volcanoes. Earth-Science Reviews, 79(1–2), 1–31. https://doi.org/10.1016/j.earscirev.2006.06.006

Hall, K. (1982). Rapid deglaciation as an initiator of volcanic activity: An hypothesis. Earth Surface Processes and Landforms, 7(1), 45–51. https://doi.org/10.1002/esp.3290070106

Hallet, B., Hunter, L., & Bogen, J. (1996). Rates of erosion and sediment evacuation by glaciers: A review of field data and their implications. Global and Planetary Change, 12(1–4), 213–235. https://doi.org/10.1016/0921-8181(95)00021-6

Hole, M. J., & LeMasurier, W. E. (1994). Tectonic controls on the geochemical composition of Cenozoic, mafic alkaline volcanic rocks from West Antarctica. Contributions to Mineralogy and Petrology, 117(2), 187–202. https://doi.org/10.1007/BF00286842

Huber, C., Bachmann, O., & Manga, M. (2009). Homogenization processes in silicic magma chambers by stirring and mushification (latent heat buffering). Earth and Planetary Science Letters, 283(1), 38–47. https://doi.org/10.1016/j.epsl.2009.03.029

Huber, C., Bachmann, O., & Manga, M. (2010). Two Competing Effects of Volatiles on Heat Transfer in Crystal-rich Magmas: Thermal Insulation vs Defrosting. Journal of Petrology, 51(4), 847–867. https://doi.org/10.1093/petrology/egq003

Huggel, C., Caplan-Auerbach, J., & Wessels, R. (2008). Recent Extreme Avalanches: Triggered by Climate Change? Eos, Transactions American Geophysical Union, 89(47), 469–470. https://doi.org/10.1029/2008EO470001

Huybers, P., & Langmuir, C. (2009). Feedback between deglaciation, volcanism, and atmospheric CO2. Earth and Planetary Science Letters, 286(3–4), 479–491. https://doi.org/10.1016/j.epsl.2009.07.014

Jarosch, A. H., & Gudmundsson, M. T. (2007). Numerical studies of ice flow over subglacial geothermal heat sources at Grímsvötn, Iceland, using Full Stokes equations. Journal of Geophysical Research: Earth Surface, 112(F2), F02008. https://doi.org/10.1029/2006JF000540

Jeffery, G. B. (1921). Plane Stress and Plane Strain in Bipolar Co-Ordinates. Philosophical Transactions of the Royal Society of London. Series A, Containing Papers of a Mathematical or Physical Character, 221, 265–293.

Jellinek, A. M., & DePaolo, D. J. (2003). A model for the origin of large silicic magma chambers: precursors of caldera-forming eruptions. Bulletin of Volcanology, 65(5), 363–381. https://doi.org/10.1007/s00445-003-0277-y

Jellinek, A. M., Manga, M., & Saar, M. O. (2004). Did melting glaciers cause volcanic eruptions in eastern California? Probing the mechanics of dike formation. Journal of Geophysical Research: Solid Earth, 109(B9), B09206. https://doi.org/10.1029/2004JB002978

Jomelli, V., Favier, V., Rabatel, A., Brunstein, D., Hoffmann, G., & Francou, B. (2009). Fluctuations of glaciers in the tropical Andes over the last millennium and

palaeoclimatic implications: A review. Palaeogeography, Palaeoclimatology, Palaeoecology, 281(3–4), 269–282. https://doi.org/10.1016/j.palaeo.2008.10.033

Julio-Miranda, P., Delgado-Granados, H., Huggel, C., & Kääb, A. (2008). Impact of the eruptive activity on glacier evolution at Popocatépetl Volcano (México) during 1994–2004. Journal of Volcanology and Geothermal Research, 170(1–2), 86–98. https://doi.org/10.1016/j.jvolgeores.2007.09.011

Jull, M., & McKenzie, D. (1996). The effect of deglaciation on mantle melting beneath Iceland. Journal of Geophysical Research: Solid Earth, 101(B10), 21815–21828. https://doi.org/10.1029/96JB01308

Koppes, M. N., & Montgomery, D. R. (2009). The relative efficacy of fluvial and glacial erosion over modern to orogenic timescales. Nature Geoscience, 2(9), 644–647. https://doi.org/10.1038/ngeo616

Kutterolf, S., Jegen, M., Mitrovica, J. X., Kwasnitschka, T., Freundt, A., & Huybers, P. J. (2013). A detection of Milankovitch frequencies in global volcanic activity. Geology, 41(2), 227–230. https://doi.org/10.1130/G33419.1

Maclennan, J., Jull, M., McKenzie, D., Slater, L., & Grönvold, K. (2002). The link between volcanism and deglaciation in Iceland. Geochemistry, Geophysics, Geosystems, 3(11), 1–25. https://doi.org/10.1029/2001GC000282

Major, J. J., & Newhall, C. G. (1989). Snow and ice perturbation during historical volcanic eruptions and the formation of lahars and floods: A global review. Bulletin of Volcanology, 52(1), 1–27. https://doi.org/10.1007/BF00641384

Marsh, B. D. (1981). On the crystallinity, probability of occurrence, and rheology of lava and magma. Contributions to Mineralogy and Petrology, 78(1), 85–98. https://doi.org/10.1007/BF00371146

Marzeion, B., Jarosch, A. H., & Hofer, M. (2012). Past and future sea-level change from the surface mass balance of glaciers. The Cryosphere; Katlenburg-Lindau, 6(6), 1295. http://dx.doi.org/10.5194/tc-6-1295-2012

McKenzie, N. R., Horton, B. K., Loomis, S. E., Stockli, D. F., Planavsky, N. J., & Lee, C.-T. A. (2016). Continental arc volcanism as the principal driver of icehouse-greenhouse variability. Science, 352(6284), 444–447. https://doi.org/10.1126/science.aad5787

Moore, J. G., & Albee, W. C. (1981). Topographic and structural changes, March–July 1980—photogrammetric data. In P. W. Lipman & D. R. Mullineaux (Eds.),

The 1980 Eruptions of Mount St. Helens (Vol. 1250). U.S. Government Printing Office.

Pagli, C., & Sigmundsson, F. (2008). Will present day glacier retreat increase volcanic activity? Stress induced by recent glacier retreat and its effect on magmatism at the Vatnajökull ice cap, Iceland. Geophysical Research Letters, 35(9). https://doi.org/10.1029/2008GL033510

Pagli, C., Sigmundsson, F., Lund, B., Sturkell, E., Geirsson, H., Einarsson, P., et al. (2007). Glacio-isostatic deformation around the Vatnajökull ice cap, Iceland, induced by recent climate warming: GPS observations and finite element modeling. Journal of Geophysical Research, 112(B8). https://doi.org/10.1029/2006JB004421

Pierson, T. C., Janda, R. J., Thouret, J.-C., & Borrero, C. A. (1990). Perturbation and melting of snow and ice by the 13 November 1985 eruption of Nevado del Ruiz, Colombia, and consequent mobilization, flow and deposition of lahars. Journal of Volcanology and Geothermal Research, 41(1), 17–66. https://doi.org/10.1016/0377-0273(90)90082-Q

Pinel, V., & Jaupart, C. (2000). The effect of edifice load on magma ascent beneath a volcano. Philosophical Transactions of the Royal Society of London A: Mathematical, Physical and Engineering Sciences, 358(1770), 1515–1532. https://doi.org/10.1098/rsta.2000.0601

Pinel, V., Jaupart, C., & Albino, F. (2010). On the relationship between cycles of eruptive activity and growth of a volcanic edifice. Journal of Volcanology and Geothermal Research, 194(4), 150–164. https://doi.org/10.1016/j.jvolgeores.2010.05.006

Praetorius, S., Mix, A., Jensen, B., Froese, D., Milne, G., Wolhowe, M., et al. (2016). Interaction between climate, volcanism, and isostatic rebound in Southeast Alaska during the last deglaciation. Earth and Planetary Science Letters, 452, 79–89. https://doi.org/10.1016/j.epsl.2016.07.033

Ragettli, S., Bolch, T., & Pellicciotti, F. (2016). Heterogeneous glacier thinning patterns over the last 40 years in Langtang Himal, Nepal. The Cryosphere, 10(5), 2075–2097. https://doi.org/10.5194/tc-10-2075-2016

Rawson, H., Pyle, D. M., Mather, T. A., Smith, V. C., Fontijn, K., Lachowycz, S. M., & Naranjo, J. A. (2016). The magmatic and eruptive response of arc volcanoes to

deglaciation: Insights from southern Chile. Geology, 44(4), 251–254. https://doi.org/10.1130/G37504.1

Rivera, A., Bown, F., Mella, R., Wendt, J., Casassa, G., Acuña, C., et al. (2006). Ice volumetric changes on active volcanoes in southern Chile. Annals of Glaciology, 43, 111–122. https://doi.org/10.3189/172756406781811970

Rubin, A. M. (1995). Propagation of Magma-Filled Cracks. Annual Review of Earth and Planetary Sciences, 23(1), 287–336. https://doi.org/10.1146/annurev.ea.23.050195.001443

Sigmundsson, F., Pinel, V., Lund, B., Albino, F., Pagli, C., Geirsson, H., & Sturkell, E. (2010). Climate effects on volcanism: influence on magmatic systems of loading and unloading from ice mass variations, with examples from Iceland. Philosophical Transactions of the Royal Society A: Mathematical, Physical and Engineering Sciences, 368(1919), 2519–2534. https://doi.org/10.1098/rsta.2010.0042

Sternai, P., Caricchi, L., Castelltort, S., & Champagnac, J.-D. (2016). Deglaciation and glacial erosion: A joint control on magma productivity by continental unloading. Geophysical Research Letters, 43(4), 2015GL067285. https://doi.org/10.1002/2015GL067285

Sternai, P., Caricchi, L., Garcia-Castellanos, D., Jolivet, L., Sheldrake, T. E., & Castelltort, S. (2017). Magmatic pulse driven by sea-level changes associated with the Messinian salinity crisis. Nature Geoscience, 10(10), 783–787. https://doi.org/10.1038/ngeo3032

Stevens, N. T., Parizek, B. R., & Alley, R. B. (2016). Enhancement of volcanism and geothermal heat flux by ice-age cycling: A stress modeling study of Greenland. Journal of Geophysical Research: Earth Surface, 2016JF003855. https://doi.org/10.1002/2016JF003855

Tait, S., Jaupart, C., & Vergniolle, S. (1989). Pressure, gas content and eruption periodicity of a shallow, crystallising magma chamber. Earth and Planetary Science Letters, 92(1), 107–123. https://doi.org/10.1016/0012-821X(89)90025-3

Thompson, L. G., Brecher, H. H., Mosley-Thompson, E., Hardy, D. R., & Mark, B. G. (2009). Glacier loss on Kilimanjaro continues unabated. Proceedings of the National Academy of Sciences, 106(47), 19770–19775. https://doi.org/10.1073/pnas.0906029106

Tolstoy, M. (2015). Mid-ocean ridge eruptions as a climate valve. Geophysical Research Letters, 42(5), 1346–1351. https://doi.org/10.1002/2014GL063015

Tuffen, H. (2010). How will melting of ice affect volcanic hazards in the twenty-first century? Philosophical Transactions of the Royal Society of London A: Mathematical, Physical and Engineering Sciences, 368(1919), 2535–2558. https://doi.org/10.1098/rsta.2010.0063

Tuffen, H., Owen, J., & Denton, J. (2010). Magma degassing during subglacial eruptions and its use to reconstruct palaeo-ice thicknesses. Earth-Science Reviews, 99(1), 1–18. https://doi.org/10.1016/j.earscirev.2010.01.001

Voight, B., Glicken, H., Janda, R.J., & Douglass, P.M. (1981). Topographic and structural changes, March–July 1980—photogrammetric data. In P. W. Lipman & D. R. Mullineaux (Eds.), Catastrophic rockslide avalanche of May 18 (Vol. 1250). U.S. Government Printing Office.

Watt, S. F. L., Pyle, D. M., & Mather, T. A. (2013). The volcanic response to deglaciation: Evidence from glaciated arcs and a reassessment of global eruption records. Earth-Science Reviews, 122, 77–102. https://doi.org/10.1016/j.earscirev.2013.03.007

Wilson, L., Sparks, R. S. J., & Walker, G. P. L. (1980). Explosive volcanic eruptions — IV. The control of magma properties and conduit geometry on eruption column behaviour. Geophysical Journal International, 63(1), 117–148. https://doi.org/10.1111/j.1365-246X.1980.tb02613.x

Chapter 4 References

Armi, L., & Millard, R. C. (1976). The bottom boundary layer of the deep ocean. Journal of Geophysical Research, 81(27), 4983–4990. https://doi.org/10.1029/JC081i027p04983

Arzeno, I. B., Beardsley, R. C., Limeburner, R., Owens, B., Padman, L., Springer, S. R., et al. (2014). Ocean variability contributing to basal melt rate near the ice front of Ross Ice Shelf, Antarctica. Journal of Geophysical Research: Oceans, 119(7), 4214–4233. https://doi.org/10.1002/2014JC009792

Brennan, P. V., Lok, L. B., Nicholls, K., & Corr, H. (2013). Phase-sensitive FMCW radar system for high-precision Antarctic ice shelf profile monitoring. Sonar Navigation IET Radar, 8(7), 776–786. https://doi.org/10.1049/iet-rsn.2013.0053

Carter, S. P., & Fricker, H. A. (2012). The supply of subglacial meltwater to the grounding line of the Siple Coast, West Antarctica. Annals of Glaciology, 53(60), 267–280. https://doi.org/10.3189/2012AoG60A119

Chen, G. (1998). GPS kinematic positioning for the airborne laser altimetry at Long Valley, California (Thesis). Massachusetts Institute of Technology. Retrieved from http://dspace.mit.edu/handle/1721.1/9680

Cook, A. J., Holland, P. R., Meredith, M. P., Murray, T., Luckman, A., & Vaughan, D. G. (2016). Ocean forcing of glacier retreat in the western Antarctic Peninsula. Science, 353(6296), 283–286. https://doi.org/10.1126/science.aae0017

Crapper, P. F. (1976). Fluxes of heat and salt across a diffusive interface in the presence of grid generated turbulence. International Journal of Heat and Mass Transfer, 19(12), 1371–1378. https://doi.org/10.1016/0017-9310(76)90065-X

Dansereau, V., Heimbach, P., & Losch, M. (2013). Simulation of subice shelf melt rates in a general circulation model: Velocity-dependent transfer and the role of friction. Journal of Geophysical Research: Oceans, 119(3), 1765–1790. https://doi.org/10.1002/2013JC008846

DiMarzio, J. P. (2007). GLAS/ICESat 500 m Laser Altimetry Digital Elevation Model of Antarctica. https://doi.org/10.5067/K2IMI0L24BRJ

Dutrieux, P., Vaughan, D. G., Corr, H. F. J., Jenkins, A., Holland, P. R., Joughin, I., & Fleming, A. H. (2013). Pine Island glacier ice shelf melt distributed at kilometre scales. The Cryosphere, 7(5), 1543–1555. https://doi.org/10.5194/tc-7-1543-2013

Fearnhead, P. G. (1975). On the formation of fronts by tidal mixing around the British Isles. Deep Sea Research and Oceanographic Abstracts, 22(5), 311–321. https://doi.org/10.1016/0011-7471(75)90072-8

Flanagan, J. D., Lefler, A. S., & Radko, T. (2013). Heat transport through diffusive interfaces. Geophysical Research Letters, 40(10), 2466–2470. https://doi.org/10.1002/grl.50440

Fretwell, P., Pritchard, H. D., Vaughan, D. G., Bamber, J. L., Barrand, N. E., Bell, R., et al. (2013). Bedmap2: improved ice bed, surface and thickness datasets for Antarctica. The Cryosphere, 7(1), 375–393. https://doi.org/10.5194/tc-7-375-2013

Gagliardini, O., Durand, G., Zwinger, T., Hindmarsh, R. C. A., & Le Meur, E. (2010). Coupling of ice-shelf melting and buttressing is a key process in ice-

sheets dynamics. Geophysical Research Letters, 37(14), L14501. https://doi.org/10.1029/2010GL043334

Gladish, C. V., Holland, D. M., Holland, P. R., & Price, S. F. (2012). Ice-shelf basal channels in a coupled ice/ocean model. Journal of Glaciology, 58(212), 1227–1244. https://doi.org/10.3189/2012JoG12J003

Guo, S.-X., Cen, X.-R., & Zhou, S.-Q. (2018). New Parametrization for Heat Transport Through Diffusive Convection Interface. Journal of Geophysical Research: Oceans, n/a-n/a. https://doi.org/10.1002/2017JC013545

Guthrie, J. D., Fer, I., & Morison, J. H. (2017). Thermohaline staircases in the Amundsen Basin: Possible disruption by shear and mixing. Journal of Geophysical Research: Oceans, 122(10), 7767–7782. https://doi.org/10.1002/2017JC012993

Gwyther, D. E., Cougnon, E. A., Galton-Fenzi, B. K., Roberts, J. L., Hunter, J. R., & Dinniman, M. S. (2016). Modelling the response of ice shelf basal melting to different ocean cavity environmental regimes. Annals of Glaciology, 57(73), 131–141. https://doi.org/10.1017/aog.2016.31

Hellmer, H., & Olbers, D. (1989). A two-dimensional model for the thermohaline circulation under an ice shelf. Antarctic Science, 1(4), 325–336.

Holland, D. M., & Jenkins, A. (1999). Modeling Thermodynamic Ice–Ocean Interactions at the Base of an Ice Shelf. Journal of Physical Oceanography, 29(8), 1787–1800. https://doi.org/10.1175/1520-0485(1999)029<1787:MTIOIA>2.0.CO;2

Holland, P. R. (2008). A model of tidally dominated ocean processes near ice shelf grounding lines. Journal of Geophysical Research: Oceans, 113(C11). https://doi.org/10.1029/2007JC004576

Horgan, H. J., Christianson, K., Jacobel, R. W., Anandakrishnan, S., & Alley, R. B. (2013). Sediment deposition at the modern grounding zone of Whillans Ice Stream, West Antarctica. Geophysical Research Letters, 40(15), 3934–3939. https://doi.org/10.1002/grl.50712

IOC, SCOR, & IAPSO. (2010). The international thermodynamic - 2010: Calculation and use of thermodynamic properties. Intergovernmental Oceanographic Commission Manuals and Guides, 56, 196.

Jacobs, S. S., & Giulivi, C. F. (2010). Large Multidecadal Salinity Trends near the Pacific–Antarctic Continental Margin. Journal of Climate, 23(17), 4508–4524. https://doi.org/10.1175/2010JCLI3284.1

Jacobs, S. S., Gordon, A. L., & Ardai, J. L. (1979). Circulation and Melting Beneath the Ross Ice Shelf. Science, 203(4379), 439–443. https://doi.org/10.1126/science.203.4379.439

Jenkins, A. (2011). Convection-Driven Melting near the Grounding Lines of Ice Shelves and Tidewater Glaciers. Journal of Physical Oceanography, 41(12), 2279–2294. https://doi.org/10.1175/JPO-D-11-03.1

Jenkins, A., Nicholls, K. W., & Corr, H. F. J. (2010). Observation and Parameterization of Ablation at the Base of Ronne Ice Shelf, Antarctica. Journal of Physical Oceanography, 40(10), 2298–2312. https://doi.org/10.1175/2010JPO4317.1

Jordan, J. R., Holland, P. R., Goldberg, D., Snow, K., Arthern, R., Campin, J.-M., et al. (2018). Ocean-Forced Ice-Shelf Thinning in a Synchronously Coupled Ice-Ocean Model. Journal of Geophysical Research: Oceans, n/a-n/a. https://doi.org/10.1002/2017JC013251

Kader, B. A., & Yaglom, A. M. (1972). Heat and mass transfer laws for fully turbulent wall flows. International Journal of Heat and Mass Transfer, 15(12), 2329–2351. https://doi.org/10.1016/0017-9310(72)90131-7

Kelley, D. E. (1990). Fluxes through diffusive staircases: A new formulation. Journal of Geophysical Research: Oceans, 95(C3), 3365–3371. https://doi.org/10.1029/JC095iC03p03365

Kimura, S., Nicholls, K. W., & Venables, E. (2015). Estimation of Ice Shelf Melt Rate in the Presence of a Thermohaline Staircase. Journal of Physical Oceanography, 45(1), 133–148. https://doi.org/10.1175/JPO-D-14-0106.1

Le Brocq, A. M., Ross, N., Griggs, J. A., Bingham, R. G., Corr, H. F. J., Ferraccioli, F., et al. (2013). Evidence from ice shelves for channelized meltwater flow beneath the Antarctic Ice Sheet. Nature Geoscience, 6(11), 945–948. https://doi.org/10.1038/ngeo1977

MacAyeal, D. R. (1984). Thermohaline circulation below the Ross Ice Shelf: A consequence of tidally induced vertical mixing and basal melting. Journal of

Geophysical Research: Oceans, 89(C1), 597–606. https://doi.org/10.1029/JC089iC01p00597

Makinson, K., Holland, P. R., Jenkins, A., Nicholls, K. W., & Holland, D. M. (2011). Influence of tides on melting and freezing beneath Filchner-Ronne Ice Shelf, Antarctica. Geophysical Research Letters, 38(6). https://doi.org/10.1029/2010GL046462

Marmorino, G. O., & Caldwell, D. R. (1976). Heat and salt transport through a diffusive thermohaline interface. Deep Sea Research and Oceanographic Abstracts, 23(1), 59–67. https://doi.org/10.1016/0011-7471(76)90808-1

Marsh, O. J., Fricker, H. A., Siegfried, M. R., Christianson, K., Nicholls, K. W., Corr, H. F. J., & Catania, G. (2016). High basal melting forming a channel at the grounding line of Ross Ice Shelf, Antarctica. Geophysical Research Letters, 43(1), 250–255. https://doi.org/10.1002/2015GL066612

McDougall, T. J., Barker, P. M., Feistel, R., & Galton-Fenzi, B. K. (2014). Melting of Ice and Sea Ice into Seawater and Frazil Ice Formation. Journal of Physical Oceanography, 44(7), 1751–1775. https://doi.org/10.1175/JPO-D-13-0253.1

McPhee, M. G. (1981). An analytic similarity theory for the planetary boundary layer stabilized by surface buoyancy. Boundary-Layer Meteorology, 21(3), 325–339. https://doi.org/10.1007/BF00119277

McPhee, M. G. (1983). Turbulent heat and momentum transfer in the oceanic boundary layer under melting pack ice. Journal of Geophysical Research: Oceans, 88(C5), 2827–2835. https://doi.org/10.1029/JC088iC05p02827

McPhee, M. G. (1992). Turbulent heat flux in the upper ocean under sea ice. Journal of Geophysical Research: Oceans, 97(C4), 5365–5379. https://doi.org/10.1029/92JC00239

McPhee, M. G., Kottmeier, C., & Morison, J. H. (1999). Ocean Heat Flux in the Central Weddell Sea during Winter. Journal of Physical Oceanography, 29(6), 1166–1179. https://doi.org/10.1175/1520-0485(1999)029<1166:OHFITC>2.0.CO;2

McWilliams, J. C., & Huckle, E. (2006). Ekman Layer Rectification. Journal of Physical Oceanography, 36(8), 1646–1659. https://doi.org/10.1175/JPO2912.1

Moholdt, G., Padman, L., & Fricker, H. A. (2014). Basal mass budget of Ross and Filchner-Ronne ice shelves, Antarctica, derived from Lagrangian analysis of

ICESat altimetry. Journal of Geophysical Research: Earth Surface, 119(11), 2014JF003171. https://doi.org/10.1002/2014JF003171

Mueller, R. D., Padman, L., Dinniman, M. S., Erofeeva, S. Y., Fricker, H. A., & King, M. A. (2012). Impact of tide-topography interactions on basal melting of Larsen C Ice Shelf, Antarctica. Journal of Geophysical Research: Oceans, 117(C5), C05005. https://doi.org/10.1029/2011JC007263

Mueller, R. D., Hattermann, T., Howard, S. L., & Padman, L. (2018). Tidal influences on a future evolution of the Filchner–Ronne Ice Shelf cavity in the Weddell Sea, Antarctica. The Cryosphere, 12(2), 453–476. https://doi.org/10.5194/tc-12-453-2018

Newell, T. A. (1984). Characteristics of a double-diffusive interface at high density stability ratios. Journal of Fluid Mechanics, 149, 385–401. https://doi.org/10.1017/S0022112084002718

Nicholls, K. W., Makinson, K., & Johnson, M. R. (1997). New oceanographic data from beneath Ronne Ice Shelf, Antarctica. Geophysical Research Letters, 24(2), 167–170. https://doi.org/10.1029/96GL03922

Orsi, A. H., & Wiederwohl, C. L. (2009). A recount of Ross Sea waters. Deep Sea Research Part II: Topical Studies in Oceanography, 56(13–14), 778–795. https://doi.org/10.1016/j.dsr2.2008.10.033

Padman, L., & Dillon, T. M. (1987). Vertical heat fluxes through the Beaufort Sea thermohaline staircase. Journal of Geophysical Research: Oceans, 92(C10), 10799–10806. https://doi.org/10.1029/JC092iC10p10799

Padman, L., & Dillon, T. M. (1988). On the Horizontal Extent of the Canada Basin Thermohaline Steps. Journal of Physical Oceanography, 18(10), 1458–1462. https://doi.org/10.1175/1520-0485(1988)018<1458:OTHEOT>2.0.CO;2

Padman, L., Fricker, H. A., Coleman, R., Howard, S., & Erofeeva, L. (2002). A new tide model for the Antarctic ice shelves and seas. Annals of Glaciology, 34(1), 247–254. https://doi.org/10.3189/172756402781817752

Padman, L., Siegfried, M. R., & Fricker, H. A. (2018). Ocean Tide Influences on the Antarctic and Greenland Ice Sheets. Reviews of Geophysics, 2016RG000546. https://doi.org/10.1002/2016RG000546

Pritchard, H. D., Ligtenberg, S. R. M., Fricker, H. A., Vaughan, D. G., van den Broeke, M. R., & Padman, L. (2012). Antarctic ice-sheet loss driven by basal

melting of ice shelves. Nature, 484(7395), 502–505. https://doi.org/10.1038/nature10968

Rack, F. R., Duling, D., Blythe, D., Burnett, J., Gibson, D., Roberts, G., et al. (2014). Developing a hot-water drill system for the WISSARD project: 1. Basic drill system components and design. Annals of Glaciology, 55(68), 285–297. https://doi.org/10.3189/2014AoG68A031

Radko, T. (2013). Double-diffusive convection. Cambridge: Cambridge University PRess.

Reese, R., Gudmundsson, G. H., Levermann, A., & Winkelmann, R. (2018). The far reach of ice-shelf thinning in Antarctica. Nature Climate Change, 8(1), 53. https://doi.org/10.1038/s41558-017-0020-x

Rignot, E., Mouginot, J., & Scheuchl, B. (2011). Ice Flow of the Antarctic Ice Sheet. Science, 333(6048), 1427–1430. https://doi.org/10.1126/science.1208336

Rignot, E., Jacobs, S., Mouginot, J., & Scheuchl, B. (2013). Ice-Shelf Melting Around Antarctica. Science, 341(6143), 266–270. https://doi.org/10.1126/science.1235798

Ruddick, B. (1983). A practical indicator of the stability of the water column to double-diffusive activity. Deep-Sea Research. Part A. Oceanographic Research Papers, 30(10), 1105–1107.

Schoof, C. (2007). Ice sheet grounding line dynamics: Steady states, stability, and hysteresis. Journal of Geophysical Research, 112(F3). https://doi.org/10.1029/2006JF000664

Schumacher, J. D., Kinder, T. H., Pashinski, D. J., & Charnell, R. L. (1979). A Structural Front Over the Continental Shelf of the Eastern Bering Sea. Journal of Physical Oceanography, 9(1), 79–87. https://doi.org/10.1175/1520-0485(1979)009<0079:ASFOTC>2.0.CO;2

Shepherd, A., Wingham, D., Wallis, D., Giles, K., Laxon, S., & Sundal, A. V. (2010). Recent loss of floating ice and the consequent sea level contribution. Geophysical Research Letters, 37(13). https://doi.org/10.1029/2010GL042496

Siegfried, M. R., Fricker, H. A., Carter, S. P., & Tulaczyk, S. (2016). Episodic ice velocity fluctuations triggered by a subglacial flood in West Antarctica. Geophysical Research Letters, 43(6), 2640–2648. https://doi.org/10.1002/2016GL067758

Sirevaag, A., & Fer, I. (2012). Vertical heat transfer in the Arctic Ocean: The role of double-diffusive mixing. Journal of Geophysical Research: Oceans, 117(C7). https://doi.org/10.1029/2012JC007910

Sommer, T., Carpenter, J. R., Schmid, M., Lueck, R. G., Schurter, M., & Wüest, A. (2013). Interface structure and flux laws in a natural double-diffusive layering. Journal of Geophysical Research: Oceans, 118(11), 6092–6106. https://doi.org/10.1002/2013JC009166

Stanton, T. P., Shaw, W. J., Truffer, M., Corr, H. F. J., Peters, L. E., Riverman, K. L., et al. (2013). Channelized Ice Melting in the Ocean Boundary Layer Beneath Pine Island Glacier, Antarctica. Science, 341(6151), 1236–1239. https://doi.org/10.1126/science.1239373

Sugiyama, S., Sawagaki, T., Fukuda, T., & Aoki, S. (2014). Active water exchange and life near the grounding line of an Antarctic outlet glacier. Earth and Planetary Science Letters, 399, 52–60. https://doi.org/10.1016/j.epsl.2014.05.001

Timmermans, M.-L., Toole, J., Krishfield, R., & Winsor, P. (2008). Ice-Tethered Profiler observations of the double-diffusive staircase in the Canada Basin thermocline. Journal of Geophysical Research: Oceans, 113(C1). https://doi.org/10.1029/2008JC004829

Tulaczyk, S., Mikucki, J. A., Siegfried, M. R., Priscu, J. C., Barcheck, C. G., Beem, L. H., et al. (2014). WISSARD at Subglacial Lake Whillans, West Antarctica: scientific operations and initial observations. Annals of Glaciology, 55(65), 51–58. https://doi.org/10.3189/2014AoG65A009

Turner, J. S. (1965). The coupled turbulent transports of salt and and heat across a sharp density interface. International Journal of Heat and Mass Transfer, 8(5), 759–767. https://doi.org/10.1016/0017-9310(65)90022-0

Walker, R. T., Dupont, T. K., Parizek, B. R., & Alley, R. B. (2008). Effects of basal-melting distribution on the retreat of ice-shelf grounding lines. Geophysical Research Letters, 35(17), L17503. https://doi.org/10.1029/2008GL034947

You, Y. (2002). A global ocean climatological atlas of the Turner angle: implications for double-diffusion and water-mass structure. Deep Sea Research Part I: Oceanographic Research Papers, 49(11), 2075–2093. https://doi.org/10.1016/S0967-0637(02)00099-7

Chapter 5 References

Dutrieux, Pierre, Stewart, Craig, Jenkins, Adrian, Nicholls, Keith W., Corr, Hugh F. J., Rignot, Eric, & Steffen, Konrad. (2014). Basal terraces on melting ice shelves. Geophysical Research Letters, 41(15), 5506–5513. https://doi.org/10.1002/2014GL060618

Gayen, B., Griffiths, R. W., & Kerr, R. C. (2015). Melting Driven Convection at the Ice-seawater Interface. Procedia IUTAM, 15, 78–85. https://doi.org/10.1016/j.piutam.2015.04.012

Gwyther, D. E., Galton-Fenzi, B. K., Dinniman, M. S., Roberts, J. L., & Hunter, J. R. (2015). The effect of basal friction on melting and freezing in ice shelf–ocean models. Ocean Modelling, 95, 38–52. https://doi.org/10.1016/j.ocemod.2015.09.004

Hattermann, T., Nøst, O. A., Lilly, J. M., & Smedsrud, L. H. (2012). Two years of oceanic observations below the Fimbul Ice Shelf, Antarctica. Geophysical Research Letters, 39(12), L12605. https://doi.org/10.1029/2012GL051012

Holland, D. M., & Jenkins, A. (1999). Modeling Thermodynamic Ice–Ocean Interactions at the Base of an Ice Shelf. Journal of Physical Oceanography, 29(8), 1787–1800. https://doi.org/10.1175/1520-0485(1999)029<1787:MTIOIA>2.0.CO;2

Huybers, P., & Langmuir, C. (2009). Feedback between deglaciation, volcanism, and atmospheric CO2. Earth and Planetary Science Letters, 286(3–4), 479–491. https://doi.org/10.1016/j.epsl.2009.07.014

Jenkins, A., Nicholls, K. W., & Corr, H. F. J. (2010). Observation and Parameterization of Ablation at the Base of Ronne Ice Shelf, Antarctica. Journal of Physical Oceanography, 40(10), 2298–2312. https://doi.org/10.1175/2010JPO4317.1

Jordan, J. R., Holland, P. R., Goldberg, D., Snow, K., Arthern, R., Campin, J.-M., et al. (2018). Ocean-Forced Ice-Shelf Thinning in a Synchronously Coupled Ice-Ocean Model. Journal of Geophysical Research: Oceans, n/a-n/a. https://doi.org/10.1002/2017JC013251

McPhee, M. (2008). Air-ice-ocean interaction: turbulent ocean boundary layer exchange processes. Dordrecht: Springer.

Mead, S., & Magill, C. (2014). Determining change points in data completeness for the Holocene eruption record. Bulletin of Volcanology, 76(11), 874. https://doi.org/10.1007/s00445-014-0874-y

Mueller, R. D., Hattermann, T., Howard, S. L., & Padman, L. (2018). Tidal influences on a future evolution of the Filchner–Ronne Ice Shelf cavity in the Weddell Sea, Antarctica. The Cryosphere, 12(2), 453–476. https://doi.org/10.5194/tc-12-453-2018

Rezvanbehbahani, S., Stearns, Leigh A., Kadivar, Amir, Walker J. Doug, & van der Veen, C. J. (2017). Predicting the Geothermal Heat Flux in Greenland: A Machine Learning Approach. Geophysical Research Letters, 44(24), 12,271-12,279. https://doi.org/10.1002/2017GL075661

Rosier, S. H. R., Gudmundsson, G. H., & Green, J. A. M. (2014). Insights into ice stream dynamics through modelling their response to tidal forcing. The Cryosphere, 8(5), 1763–1775. https://doi.org/10.5194/tc-8-1763-2014

Rougier, J., Sparks, S. R., & Cashman, K. V. (2016). Global recording rates for large eruptions. Journal of Applied Volcanology, 5(1), 11. https://doi.org/10.1186/s13617-016-0051-4

Stanton, T. P., Shaw, W. J., Truffer, M., Corr, H. F. J., Peters, L. E., Riverman, K. L., et al. (2013). Channelized Ice Melting in the Ocean Boundary Layer Beneath Pine Island Glacier, Antarctica. Science, 341(6151), 1236–1239. https://doi.org/10.1126/science.1239373

Watt, S. F. L., Pyle, D. M., & Mather, T. A. (2013). The volcanic response to deglaciation: Evidence from glaciated arcs and a reassessment of global eruption records. Earth-Science Reviews, 122, 77–102. https://doi.org/10.1016/j.earscirev.2013.03.007

Wild, C. T., Marsh, O. J., & Rack, W. (2017). Viscosity and elasticity: a model intercomparison of ice-shelf bending in an Antarctic grounding zone. Journal of Glaciology, 63(240), 573–580. https://doi.org/10.1017/jog.2017.15